SECOND-HARMONIC GENERATION-BASED MUELLER MATRIX POLARIZATION ANALYSIS OF COLLAGEN-RICH TISSUES

BY

CHUKWUEMEKA OKORO

DISSERTATION

Submitted in partial fulfillment of the requirements
for the degree of Doctor of Philosophy in Electrical and Computer Engineering
in the Graduate College of the
University of Illinois at Urbana-Champaign, 2018

Urbana, Illinois

Doctoral Committee:

Associate Professor Kimani C. Toussaint, Chair
Professor Gabriel Popescu
Professor Umberto Ravaioli
Associate Professor Viktor Gruev

ABSTRACT

Quantitative assessment of the properties of fibrillar collagen in tissue can yield deeper insight into structure-function correlations of the cell and its surrounding matrix. Second-harmonic generation (SHG) microscopy is especially well-suited as an image acquisition technique, due to its specificity to the non-centrosymmetric structure of collagen, and inherent confocality which enables three-dimensional sectioning. SHG imaging can be undertaken in a quantifiable manner, or combined with other techniques that highlight desired properties.

A powerful property for characterizing collagenous tissue microstructure is the Mueller matrix polarization response. Two polarimetric imaging approaches are demonstrated for robust Mueller matrix characterization of collagenous tissue. One approach, called the two-photon Mueller matrix second-harmonic generation (MMSHG) microscopy, involves the generalization of Mueller matrix to the case of two-photon excitation. This 4×9 two-photon Mueller matrix is extracted using second-harmonic generation microscopy and analyzed for quantitative collagen assessment. The matrix and associated degree-of-polarization parameter from different sample types and thicknesses are also investigated. It was observed that the polarization-dependent degree-of-polarization distribution shape changes and a model-based bimodal mean difference metric increases with sample thickness.

The second polarization technique which we developed, called second-harmonic patterned polarization-analyzed reflection confocal (SPPARC) microscopy, uses the conventional linear polarimetry of confocal images, delineated with a second-harmonic mask. This latter approach, combining the metric richness of linear polarimetry with the specificity of SHG imaging, is used for assessing collagen, as well as non-collagenous regions, in porcine tendon and ligament. We observed differences in depolarization and circular degree-of-polarization parameters, that have potential for differentiating

tissues in varying states.

Next, we present the results of SPPARC microscopy and analysis of collagen on varying pathologies of breast tissues. Experiments were conducted on a breast tissue microarray having *benign tissues* (BT), malignant *invasive lobular carcinoma* (ILC), and benign stroma adjacent to the malignant tissues (called the *benign adjacent tissue*, or BAT). We observed that stroma in BAT and ILC exhibits the largest parameter differences, with collagen readings in ILC showing lower depolarization, lower diattenuation and higher linear degree-of-polarization values than stromal collagen in BAT. This result suggests that the optical properties of collagen change most in the vicinity of tumors. A similar trend is also exhibited in the non-collagenous extrafibrillar matrix *plus* cells (EFMC) region.

We finally discuss additional work involving polarization modeling, setup optimization, and implementation of other decomposition techniques.

To my siblings, Ugo, Chy and Uchay, for support and encouragement
To my parents, Chukwudi and Josephine, for their love and support
To God, for science, my faith and a beautiful future

ACKNOWLEDGMENTS

There are so many people who have helped me through my doctoral program. First, I would like to express my gratitude to my remarkable Ph.D. advisor, Dr. Kimani Toussaint, Jr. His mentorship and help as I adjusted to the academic and research life in a new country were priceless. I have always enjoyed the passion and intelligence he brings to science research. He showed me a good mix of patience and pressure to help me achieve my goals, even when they did not always directly align with the group work. I will never forget that he supported me when I attempted some entrepreneurial endeavors. He constantly encouraged me to attend conferences, and definitely helped me polish my speaking style and delivery. When collaborating on papers, his excellent writing and attention to detail have always been impressive (even if it meant going through many many many rounds of edits).

I would also like to thank collaborators, professors and teachers in and out of Illinois: my Ph.D academic advisor, Dr. Gabriel Popescu, whose Modern Light Microscopy class was one of my favorite on campus and whose deep understanding of optics I admire; Dr. Ayman Abouraddy who has a brilliant mind, and with whom I enjoyed interacting and collaborating on an intriguing paper; Dr. Ilesanmi Adesida, for his mentorship and inspiring discussions; Dr. Gary Eden who was my master's academic advisor; and Dr. Mayandi Sivaguru who initially trained me on nonlinear imaging at the core facility on campus. I would also like to thank Dr. Umberto Ravaioli and Dr. Viktor Gruev for agreeing to serve on my doctoral committee.

I am grateful to have worked and/or interacted with current and former group members: Woowon Lee (you should have a dual-degree in sample preparation), Mohammad Kabir (the reliable lab manager!), Qing Ding (always running simulations), Varun Kelkar, Aakash Choubal, Hemangg Rajput, Arif Syraj, Gopala Inavalli, Abdul Bhuiya, Hao Chen and Brian Roxworthy. From the lab cleanup sessions to the celebratory dinners hosted by

whoever passed the last exam, and of course, the arguments and discussions about science, it was a truly memorable experience.

I will not forget my Kings' Assembly family. These wonderful people made my life in Urbana-Champaign exciting. Particularly, Laolu Adeniba, my friend and mentor, has been an immense source of support. I also recognize Laolu Ajala, Biodun Oki, Iyke Idehen, Emeka Okekeocha and Tola Okesanjo.

Finally, I would like to thank my parents and siblings. I am deeply appreciative of their love and patience through this journey.

TABLE OF CONTENTS

CHAPTER 1 INTRODUCTION 1
1.1 Second-harmonic generation imaging 1
1.2 Polarization-based imaging 2
1.3 The best of both worlds 2

CHAPTER 2 SECOND-HARMONIC GENERATION IMAGING OF COLLAGEN 4
2.1 Motivation 4
2.2 Second-harmonic generation 9
2.3 SHG theory 9
2.4 SHG microscopy 16

CHAPTER 3 POLARIMETRIC IMAGING 23
3.1 Polarization 23
3.2 Mueller matrix theory 29
3.3 Mueller matrix polarimetry 39

CHAPTER 4 MUELLER MATRIX SECOND-HARMONIC GENERATION MICROSCOPY 41
4.1 Introduction 41
4.2 Theory 42
4.3 Experiment 47
4.4 Results and discussion 48

CHAPTER 5 SECOND-HARMONIC PATTERNED POLARIZATION ANALYZED REFLECTION CONFOCAL MICROSCOPY . 53
5.1 Introduction 53
5.2 Confocal microscopy 54
5.3 Experiment 55
5.4 Results 58

CHAPTER 6 ANALYSIS OF STROMAL COLLAGEN IN BREAST BIOPSIES 64
6.1 Motivation 64
6.2 Experiment 66

6.3 Results 67
6.4 Summary 72

CHAPTER 7 CONCLUSION 74
7.1 Future directions 75

APPENDIX A POLARIMETRIC MEASUREMENTS 79

APPENDIX B MUELLER MATRIX ANALYSIS 81
B.1 Some polarization parameters 81
B.2 Mueller matrix polar decomposition 82

APPENDIX C COMMENTS ON SOME EXPERIMENTAL SPECIFICATIONS 84
C.1 Laser source 84
C.2 Detectors 84
C.3 Acquisition speed 84

REFERENCES 86

CHAPTER 1

INTRODUCTION

1.1 Second-harmonic generation imaging

Second-harmonic generation (SHG) imaging is a nonlinear imaging technique, based on the second-harmonic generation process, that has found a broad range of applications for imaging and assessing materials. It is useful due to its intrinsic confocality that enables three-dimensional optical sectioning and the non-requirement of labeling that is the hallmark of fluorescence-based methods. However, appreciable signal from samples is generated when there is wavelength-order non-centrosymmetry; this requirement constrains the application of SHG to samples for which there is no structural inversion symmetry. Since surfaces break the symmetry when moving from a medium of one refractive index to another, SHG imaging has been used for analysis of surface properties [1–4]. In addition, many biological tissues contain fibrillar collagen, which is non-centrosymmetric and hence quite amenable to probing via SHG imaging. In fact, collagen is the main structural protein in mammals [5] (with fibillar collagen type 1 being the major collagen type [5,6]) and can be found in skin, cornea, cartilage, bone, tendon and ligaments [7–11].

Collagen provides cell structural support, preserves tissue architecture [12,13] and plays an important role in cell function and development [14–16]. It can be abnormally altered by physical injury or through disorders such osteogenesis imperfecta, keratoconous and sarcoma [17–19]. In addition, its role as part of the extracellular matrix (or ECM) in mediating cancer growth and metastasis has been increasingly recognized over the years [20–22]. Therefore, it is beneficial to image and assess collagen in order to gain more insight into how its properties (molecular changes, structure, polarization response, organization) may affect and/or be affected by its environment. SHG microscopy is a powerful tool for such imaging analysis of collagen, having been

used both exclusively and in conjunction with other modalities.

1.2 Polarization-based imaging

Polarization-based (or polarization-resolved) imaging techniques are supplementary techniques for enhancing contrast and/or extracting polarization information from a sample [23–25]. The additional information achievable is due to the inherent polarization altering properties of the sample under consideration. Therefore, these methods are advantageous for imaging anisotropic and polarization-altering media. The goals of polarization-based experiments are to generate parameters that are representative of the sample polarization response and to deduce how they are generated by sample structure or molecular orientation. This is useful as a diagnostic and prognostic biological tool. The polarimetric approaches undertaken can range from imaging for anisotropy ratio [26, 27] and polarized light microscopy [28, 29] to more complex polarization matrix imaging [30–32].

1.3 The best of both worlds

This thesis focuses on work done in integrating SHG and polarization-imaging techniques for robust assessment of tissues, particularly collagen. The fundamental theoretical framework and description of second-harmonic generation and polarization is laid out in Chapters 2 and 3, respectively, along with summary of work done in these fields. The next two chapters explore two techniques that were developed and demonstrated during the course of my program; the first, Mueller-matrix second-harmonic generation (MMSHG) microscopy, is introduced in Chapter 4. The chapter also describes the experimental demonstration of the microscopy technique on collagen-rich tendon samples, and discusses the results obtained. The second technique (second-harmonic patterned polarization-analyzed reflection confocal, or SPPARC, microscopy), which has several advantages over the first, is described in Chapter 5 along with its application for analysis of collagen-rich tendon and ligament tissues. SPPARC is then applied for analysis of collagen within and adjacent to breast invasive lobular carcinoma tumors, to demonstrate

its utility as a diagnostic tool in Chapter 6. Finally, conclusions are drawn and future directions considered in Chapter 7.

CHAPTER 2

SECOND-HARMONIC GENERATION IMAGING OF COLLAGEN

2.1 Motivation

2.1.1 Extracellular matrix and collagen

The extracellular matrix (ECM) is the non-cellular biological matter between cells. Its utility in the body ranges from support for tissue integrity and elasticity, and controlling tissue homeostasis via remodeling [33], to affecting cell adhesion, differentiation and proliferation [34]. In mammals, the ECM is composed of about 300 proteins such as collagen, proteoglycans and glycoproteins [35], which are typically large and complex. The structure-function dynamics of the ECM components play important roles in cell development, and can exacerbate existing diseases or lead to new ones.

Collagen is the most prevalent protein in mammals. It is assembled from trimeric molecules made of three polypeptide α chains forming a triple helix domain structure, can form supramolecular aggregates and is typically deposited within the ECM [36]. It constitutes a major component of skin, cornea, cartilage, tendons, ligaments and most of the organic matrix in bone and dentin [37, 38].

In humans, there are 28 different types of collagen. The most abundant of these are the fibril-forming collagens (types I, II, III, V, XI, XXIV and XXVII), with type I being the most widely occurring in skin, tendon, and bone [37]. The molecular triple-helical structure is characterized by domains containing mostly glycine, proline and hydroxyproline amino acids. The sequence of amino acids is nonrepetitive and complex, giving the molecule no inversion symmetry [39]. Collagen molecules of ~ 300 nm length and ~ 1.5 nm width are periodically staggered with respect to each other to form fibrils with diameters of $\sim$20–250 μm. The fibrils function as the basic structural

unit providing mechanical strength where required. The fibrils themselves are aggregated into fibers with diameters of up to 500 μm [40]. Figure 2.1 shows an illustration of collagen assembly.

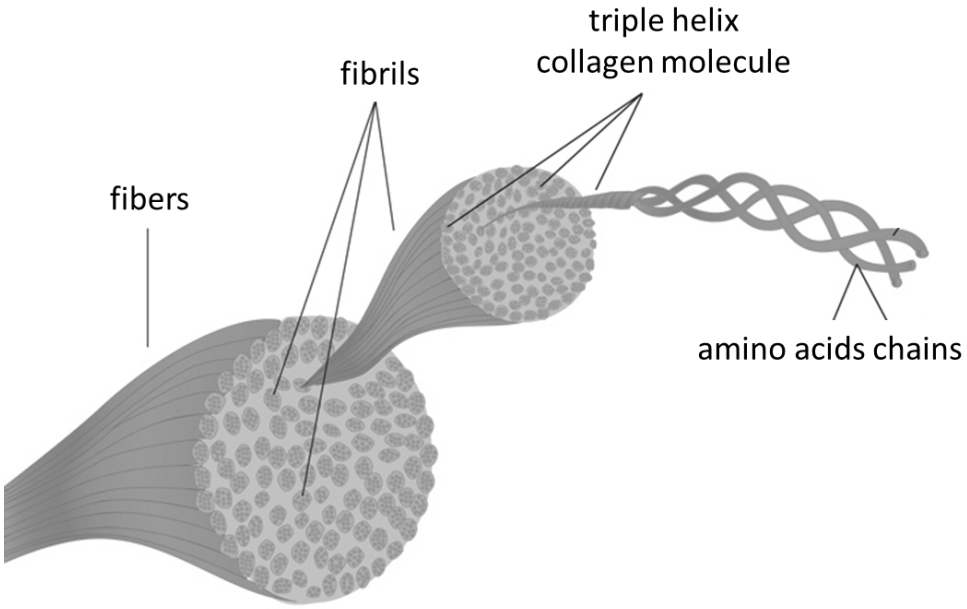

Figure 2.1: Assembly of collagen starting with amino acid chains, built into α-chains, which form the triple helical collagen molecules. These combine to form collagen fibrils, which in turn aggregate to form fibers. Adapted from [41].

The triple-helix arrangement and molecular packing structure of collagen result in a number of properties, one of which is the anisotropic behavior of collagen [42]. For fibrillar collagen, the refractive index along the fiber's length is typically higher than that across the fiber, yielding unixial positive birefringence [43]. If collagen fibers lose their α-helix (as occurs during thermal denaturation, where collagen gains a random-coil arrangement), a loss in birefringence becomes apparent [44].

The crystal class symmetry for collagen is not definite, as is expected for many biological materials. Several crystallographic studies have been carried out to determine its symmetry, and a number of them point to the collagen molecules having two general regions, forming a triangular and a square pattern, when looking down the helical axis [45–47]. The pattern in the center of the square regions maintains a *pseudo-tetragonal* distribution,

with helices surrounded by five nearest neighbors at roughly similar distances away. Figure 2.2 shows an illustration of the molecular arrangement. A separate model re-interpretation has also been given to the X-ray data leading to a *quasi-hexagonal* molecular packing structure [48].

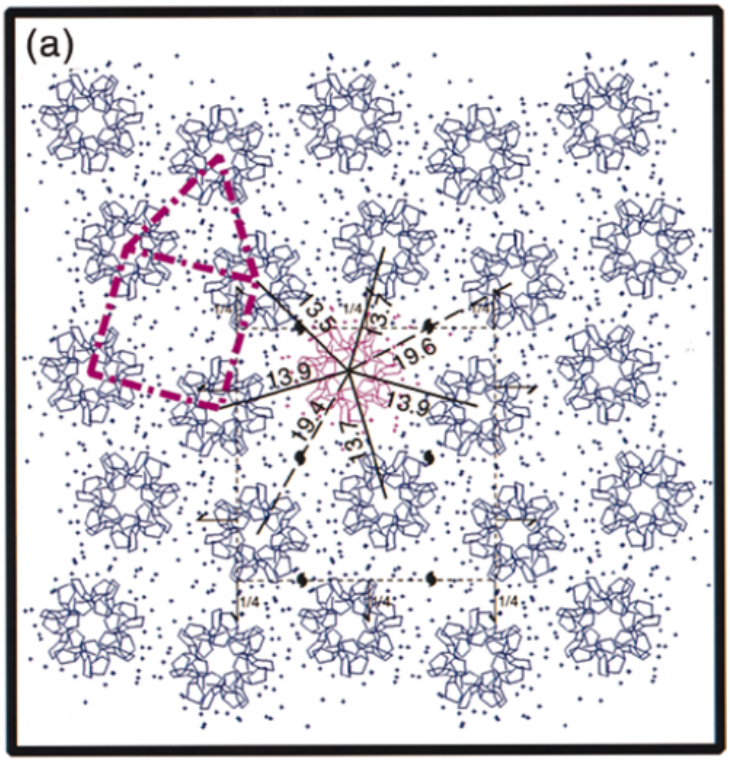

Figure 2.2: Collagen molecular packing showing the pseudo-tetragonal crystal symmetry. The square pattern, triangular pattern and distances of helix to neighbors are shown. Reprinted with permission from Ref [46], Elseiver.

2.1.2 Role of collagen

Collagen plays a number of important biomechanical roles in the body, primarily towards maintenance of structural integrity and elasticity of tissue and organs. For example, type I collagen provides tensile stiffness in tendon and aids load bearing and torsional stiffness after calcification in bone [49]. This is typically accomplished by forming fibrils, with additional mechanical resilience introduced by formation of covalent cross-links.

Aside from biomechanical roles, collagen interaction mediated by receptors has been observed to define cell adhesion, differentiation, growth and survival

[50]. Furthermore, it takes part in entrapment and delivery of growth factors during organ development, wound healing and tissue repair [51–53].

Certain abnormalities in the structure or composition of collagen can result in diseases. As an example, mutation in one of the two genes' encoding of collagen type I results in the genetic disorder osteogenesis imperfecta. This disorder is associated with increased bone fragility, low bone mass and other connective-tissue symptoms [54]. Another example is the eye disorder, keratoconous, which arises when the cornea weakens due to anomalies in its structure and/or composition (including collagen fibrils) [18, 55]. One other collagen disorder is the relatively rare sarcoma – malignant tumors of connective tissues containing collagen [56]. Sarcomas may reveal themselves as painless lumps (with soft tissue sarcomas) or bone pains and swelling (in the case of osteosarcoma). In addition, there is increasing appreciation for the role of collagen in tumor progression and metastasis, and this will be explored in detail in Chapter 6.

Consequently, it can be seen that assessment of collagen would be immensely valuable, not only for deeper understanding of its function, but for insight on disease prevention and therapeutic actions. Collagen imaging provides a robust platform for analysis by which researchers can see and investigate the underlying structure of samples.

2.1.3 Imaging collagen

Many techniques have been used for microscopic imaging of collagen. For example, polarized light microscopy (PLM), which is a brightfield technique that leverages the birefringent property of collagen to enhance contrast, has been used. By placing the sample between crossed polarizers in the optical setup, the sample birefringence effect shows up as modulation of brightness and color. This has been used in the study of collagen's molecular/structural features [57,58] and as a collagen assessment/diagnostic tool [23,43]. By using staining dyes, such as picrosirius red, which enhance collagen anisotropic behavior, more compelling results can be obtained [59, 60]. A shortcoming of PLM is its limitation to two-dimensional imaging and assessment.

Another technique is electron microscopy which provides much higher resolution than optical methods. Scanning electron microscopy (SEM) has

been used for studying articular cartilage collagen organization in joint surfaces [58,61,62], while the higher-resolution transmission electron microscope (TEM) has been applied for imaging the nanostructural organization of collagen in bone [63] and to determine the fibril size and structure [64]. The good resolution achievable from electron microscopy ($\sim$1-10 nm for SEM and as much as 100 times better for TEM) makes it a prime candidate for viewing collagen structures in much detail. However, several constraints can offset the advantage, especially for biological samples. The samples go through harsh biology-disturbing preparation procedures of having to be fixed and dehydrated to prevent beam obstruction by vapor, since the environment has to be a vacuum. Also, the samples are usually coated with a thin layer of metal (such as gold) to make the samples more conductive and prevent build-up of electrons. The requirement of dehydration has been alleviated with the use of environmental SEM (or ESEM), but the process is still not optimal [65].

Laser scanning confocal microscopy is another example of a microscopy technique that has been used for collagen imaging. This is a point-scanning modality that is quite popular in biological imaging due to its use of the spatial pinhole for optical 3D sectioning, and which enhances the theoretical lateral resolution obtained from conventional brightfield microscopy by a factor of $\sim$1.5. It has been used for imaging collagen in heart muscles [66], heart septum [67] and cornea [68].

One shortcoming of all these techniques described is that none is specific to the structure of collagen. This is not a disadvantage if the goal is to visualize everything in a sample, but does become a drawback if there is a need to be sensitive to only collagen. This is where SHG microscopy comes into the picture. This nonlinear imaging technique, based on the SHG process, demonstrates specificity to the non-centrosymmetric structure of collagen, and can image it in isolation from other surrounding centrosymmetric biological constituents. By reason of its intrinsic confocality within the thin focal volume where SHG occurs for focusing systems, optical sectioning is achievable. The next sections review the theory and implementation of SHG microscopy.

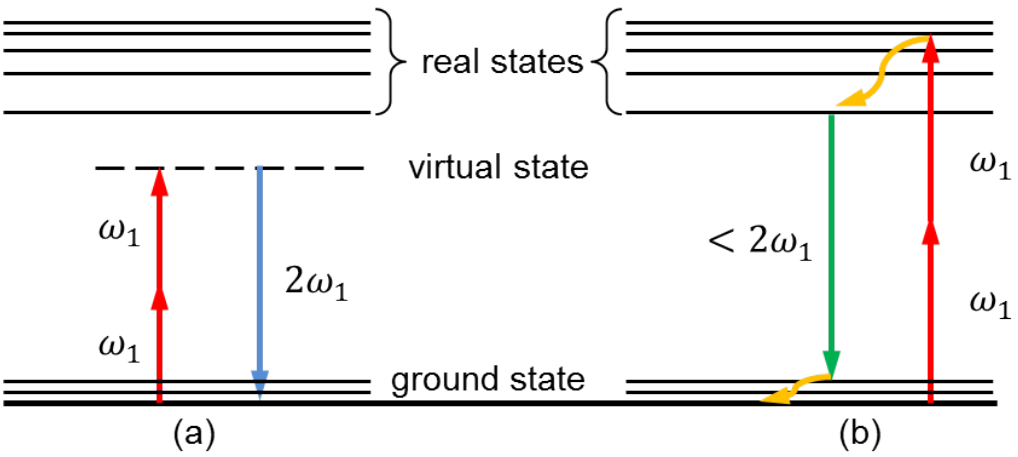

Figure 2.3: Quantum mechanical picture illustrating photon energy conversion for (a) second-harmonic generation and (b) two-photon fluorescence.

2.2 Second-harmonic generation

Second-harmonic generation (SHG) is a coherent nonlinear optical scattering process that occurs when incident light of a particular wavelength interacts in a medium having a non-centrosymmetric structure, to yield light at half the wavelength (or equivalently, twice the frequency). The nonlinearity is negligible at low intensities, but becomes more appreciable at higher intensities, of the order of 10^5 - 10^8 V/m [69]. Figure 2.3a shows the quantum-mechanical picture for second harmonic generation. It makes use of virtual states for the two-to-one photon conversion. This energy-conserving operation contrasts with the nonlinear absorption-fluorescence characteristic that is present in two-photon fluorescence (TPF) (shown in Fig. 2.3b). For this reason, SHG has been variously described as coherent [2, 70] or parametric [71, 72].

2.3 SHG theory

Starting off with the basic consideration of the induced polarization density (P) due to incident field E in a lossless material, we express this as

$$P = \epsilon_0[\chi^{(1)}E + \chi^{(2)}E^2 + \chi^{(3)}E^3 + ...] \quad , \tag{2.1}$$

where $\chi^{(j)}$ is the jth-order susceptibility. The first term describes the linear susceptibility ($\chi^{(1)}$) related to the refractive index of the material by $n = \sqrt{1 + \chi^{(1)}}$. It is important to note that in the more general case of lossy materials (that is, materials for which absorption is present), the nonlinear susceptibility becomes a complex quantity relating complex amplitudes of electric fields and polarization density. This would enable the mathematical formulation for the so-called *non*-parametric processes [71] involving real states, such as two-photon fluorescence (TPF) and stimulated Raman scattering (SRS).

The second term of Eq. 2.1 can be expanded as a more general formulation for second-order parametric processes such as sum-frequency generation (SFG) and difference-frequency generation (DFG), given as

$$P_l(2\omega) = \sum_{mn} \chi_{lmn} E_m(\omega) E_n(\omega) \qquad l, m, n = 1, 2, 3 \quad , \tag{2.2}$$

where ω is the angular frequency, χ_{lmn} is a third-rank tensor and $P(2\omega)$ is the component polarization density along the principal axes of the material, l is the running axis index and m and n are dummy indices. The degeneracy of the SHG process simplifies the mathematical formulations, obviating the need to invoke intrinsic or full permutation symmetries [71], and requiring only consideration of the spatial symmetry (or lack thereof) of the nonlinear medium on the order of the illuminating wavelength.

2.3.1 Spatial symmetry considerations

The important spatial symmetry property for second-harmonic generation is that it can only occur in noncentrosymmetric media, that is, media which do not possess a center of inversion symmetry (on the order of the wavelength of the probing light). One intuitive way to think about it is to consider that for a centrosymmetric material, the induced polarization ($+P$) by a given field $+E$ should change to ($-P$) given the field $-E$ (Figure 2.4). This is expected because both A and B will encounter the same spatial structure (since it is symmetric), with the only change expected in the change of polarization density sign. However, for second-order harmonics (and ignoring constants), $P = (+E)^2 = (-E)^2 = -P$ which can only be the case if $P = 0$.

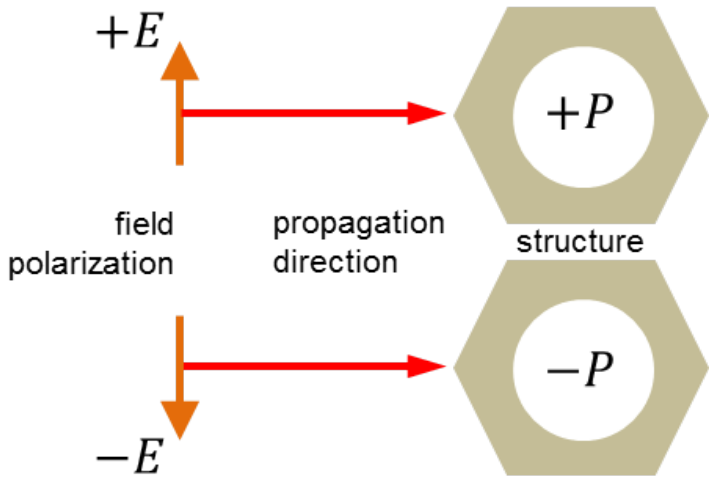

Figure 2.4: Induced polarization in a centrosymmetric medium.

This suggests that the second-order signals (or even-ordered signals, for that matter) vanish in centrosymmetric media. Insight can also be obtained using the potential well analogy from Ch. 6 of Ref [71].

2.3.2 Coupled wave equations for SHG

We start with a form of Maxwell's differential equations:

$$\nabla \cdot \boldsymbol{D} = 4\pi\rho \tag{2.3}$$

$$\nabla \cdot \boldsymbol{B} = 0 \tag{2.4}$$

$$\nabla \times \boldsymbol{E} = -\frac{1}{c}\frac{\partial \boldsymbol{B}}{\partial t} \tag{2.5}$$

$$\nabla \times \boldsymbol{H} = \frac{1}{c}\frac{\partial \boldsymbol{D}}{\partial t} + \frac{4\pi}{c}\boldsymbol{J} \quad . \tag{2.6}$$

For majority of biological samples, we can make assumptions of absence of free charges ($\rho = 0$), free currents ($\boldsymbol{J} = 0$) and nonmagnetic materials ($\mu = 1, \boldsymbol{B} = \boldsymbol{H}$). Since the material is nonlinear, we express the displacement field as

$$\boldsymbol{D} = \epsilon_o \boldsymbol{E} + 4\pi \boldsymbol{P} \quad , \tag{2.7}$$

where $\boldsymbol{P}$ is the induced polarization density vector and ϵ_0 is the permittivity of free space. By taking the curl of both sides in Eq. 2.5, we obtain

$$\nabla \times \nabla \times \boldsymbol{E} + \frac{1}{c^2}\frac{\partial^2 \boldsymbol{D}}{\partial t^2} = 0 \tag{2.8}$$

$$\nabla \times \nabla \times \boldsymbol{E} + \frac{\epsilon_o}{c^2}\frac{\partial^2 \boldsymbol{E}}{\partial t^2} = -\frac{4\pi}{c^2}\frac{\partial^2 \boldsymbol{P}}{\partial t^2} \quad . \tag{2.9}$$

We know that $\nabla \times \nabla \times \boldsymbol{E} = \nabla(\nabla \cdot \boldsymbol{E}) - \nabla^2 \boldsymbol{E}$, and it can be shown that with the slowly-varying amplitude approximation, $\nabla \cdot \boldsymbol{E}$ is very small. Hence Eq. 2.8 reduces to the form

$$-\nabla^2 \boldsymbol{E} + \frac{\epsilon_o}{c^2}\frac{\partial^2 \boldsymbol{E}}{\partial t^2} = -\frac{4\pi}{c^2}\frac{\partial^2 \boldsymbol{P}}{\partial t^2} \tag{2.10}$$

If we split the linear and nonlinear parts of the polarization density (as in Eq. 2.1) to

$$\boldsymbol{P} = \boldsymbol{P}^L + \boldsymbol{P}^{NL} \quad , \tag{2.11}$$

then Eq. 2.10 becomes

$$-\nabla^2 \boldsymbol{E} + \frac{\epsilon_o}{c^2}\frac{\partial^2 \boldsymbol{E}}{\partial t^2} + \frac{4\pi}{c^2}\frac{\partial^2 \boldsymbol{P}^L}{\partial t^2} = -\frac{4\pi}{c^2}\frac{\partial^2 \boldsymbol{P}^{NL}}{\partial t^2} \tag{2.12}$$

$$-\nabla^2 \boldsymbol{E} + \frac{\epsilon}{c^2}\frac{\partial^2 \boldsymbol{E}}{\partial t^2} = -\frac{4\pi}{c^2}\frac{\partial^2 \boldsymbol{P}^{NL}}{\partial t^2} \quad , \tag{2.13}$$

where ϵ $(= \epsilon_0 + 4\pi\frac{\boldsymbol{P}^L}{\boldsymbol{E}} = \epsilon_0 + 4\pi\epsilon_0\chi^{(1)})$ is the linear permittivity of the medium. Equation 2.13 is an inhomogeneous wave equation with the medium nonlinear response as the source driving term.

Since multiple frequencies exist, we express the fields in terms of these frequencies obtaining:

$$-\nabla^2 \boldsymbol{E} + \frac{\epsilon_o}{c^2}\frac{\partial^2 \boldsymbol{E}}{\partial t^2} + \frac{4\pi}{c^2}\frac{\partial^2 \boldsymbol{P}^L}{\partial t^2} = -\frac{4\pi}{c^2}\frac{\partial^2 \boldsymbol{P}^{NL}}{\partial t^2} \tag{2.14}$$

$$-\nabla^2 \boldsymbol{E} + \frac{\epsilon}{c^2}\frac{\partial^2 \boldsymbol{E}}{\partial t^2} = -\frac{4\pi}{c^2}\frac{\partial^2 \boldsymbol{P}^{NL}}{\partial t^2} \quad . \tag{2.15}$$

For second-harmonic generation, the total field can be expressed as

$$\boldsymbol{E}_p(z,t) = \boldsymbol{A}_p e^{-j(k_p z - \omega_p t)} + \left[\begin{smallmatrix}\text{complex}\\ \text{conjugate}\end{smallmatrix}\right] \quad p = 1, 2 \quad , \tag{2.16}$$

where

$$k_1 = \frac{\omega_1 n(\omega_1)}{c}, \quad k_2 = \frac{2\omega_1 n(2\omega_1)}{c}, \quad n(\omega_1) = (\epsilon(\omega_1)^{\frac{1}{2}}) \quad , \tag{2.17}$$

and ω_1 and $2\omega_1$ are the frequencies that exist. The induced second-order polarization vector components due to three-wave mixing fields are given by [71]

$$P_i(\omega_m + \omega_n) = \sum_{jk} \sum_{mn} \chi_{ijk} E_j(\omega_m) E_k(\omega_n) \quad i, j, k = 1, 2, 3. \tag{2.18}$$

For the degenerate SHG case having fixed propagation and polarization directions, the amplitude for each frequency component reduces to

$$P_1(z) = 4d_{\text{eff}} E_1^* E_2 = 4d_{\text{eff}} A_1^* A_2 e^{-j(k_2 - k_1)z} + \left[\begin{smallmatrix} \text{complex} \\ \text{conjugate} \end{smallmatrix} \right] \tag{2.19}$$

$$P_2(z) = 2d_{\text{eff}} E_1^* E_1 = 2d_{\text{eff}} A_1^2 e^{-2j(k_1)z} + \left[\begin{smallmatrix} \text{complex} \\ \text{conjugate} \end{smallmatrix} \right] \quad , \tag{2.20}$$

where d_{eff} is the effective scalar value related to the second-order nonlinear susceptibility ($\chi^{(2)}$). Assuming each frequency component obeys the inhomogeneous wave equation 2.13, we can substitute Eq. 2.16 for $\boldsymbol{E}$ and one of Eqs. 2.19 or 2.20 for $\boldsymbol{P}$ to derive the coupled equations

$$\frac{dA_1}{dz} = \frac{-j8\pi\omega_1^2 d_{\text{eff}}}{k_1 c^2} A_2 A_1^* e^{j\Delta k z} \tag{2.21}$$

$$\frac{dA_2}{dz} = \frac{-j4\pi\omega_2^2 d_{\text{eff}}}{k_2 c^2} A_1^2 e^{-j\Delta k z} \quad , \tag{2.22}$$

where $\Delta k = 2k_1 - k_2$. To get to Eqs. 2.21 and 2.22, the slowly varying amplitude approximation has been invoked. This is valid since the first-order rate of change of the field with respect to distance is typically much greater than the second-order rate ($\left|\frac{\partial^2 A_p}{\partial z^2}\right| << \left|\frac{\partial A_p}{\partial z}\right|$). Consider a nonlinear medium of length L in Fig. 2.5, through which light of the fundamental wavelength goes through. Using the undepleted-pump approximation (A_1 is constant), the field strength can be obtained by integrating over L, yielding

$$A_2(L) = \int_0^L \frac{-j4\pi\omega_2^2 d_{\text{eff}}}{k_2 c^2} A_1^2 e^{-j\Delta k z} dz \tag{2.23}$$

$$= \frac{-j4\pi\omega_2^2 d_{\text{eff}} A_1^2}{k_2 c^2} \frac{(1 - e^{-j\Delta k L})}{j\Delta k} \quad . \tag{2.24}$$

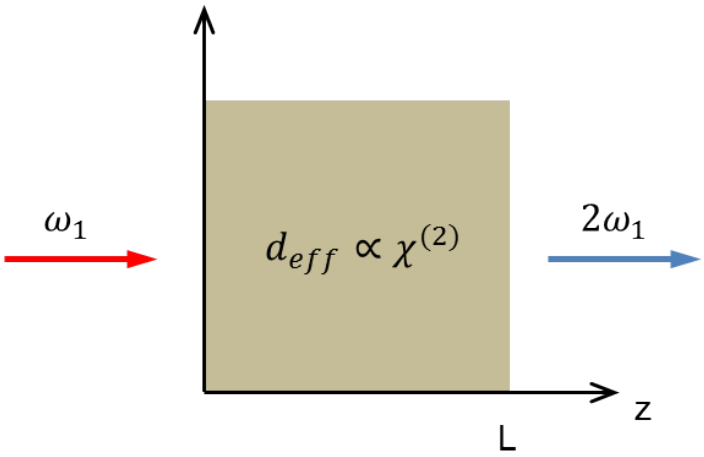

Figure 2.5: Generated second-harmonic signals through a nonlinear medium of length L.

The intensity due to this field can be expressed as

$$\begin{aligned} I_2 &= \frac{n_2 c}{2\pi}|A_2(L)|^2 \\ &= \frac{8n_2\pi\omega_2^4 d_{\text{eff}}^2 A_1^4}{k_2^2 c^3}\left|\frac{(1-e^{-j\Delta kL})}{j\Delta k}\right|^2 \\ &= \frac{8n_2\pi\omega_2^4 d_{\text{eff}}^2 A_1^4}{k_2^2 c^3} L^2 sinc^2(\frac{\Delta kL}{2}) \quad . \end{aligned} \tag{2.25}$$

It can be observed that maximum intensity of the generated second-harmonic occurs when the phase mismatch factor, $\Delta k = 0$, a case that occurs when there is phase-matching.

2.3.3 Phase matching

A plot of the intensity profile dependence on the term $\frac{\Delta kL}{2}$ is shown in Fig. 2.6. The maximum intensity condition of $\Delta k = 0$, called the *perfect phase matching* condition, is achieved when the second-harmonic wave maintains a fixed phase relationship with respect to the induced polarization. In terms of multiple dipoles, this occurs when the atomic dipoles are properly phased so that the generated fields add coherently to yield a total emitted field that scales as the square of the number of generating atoms. The phase matching condition is difficult to achieve with collinear beams because the refractive

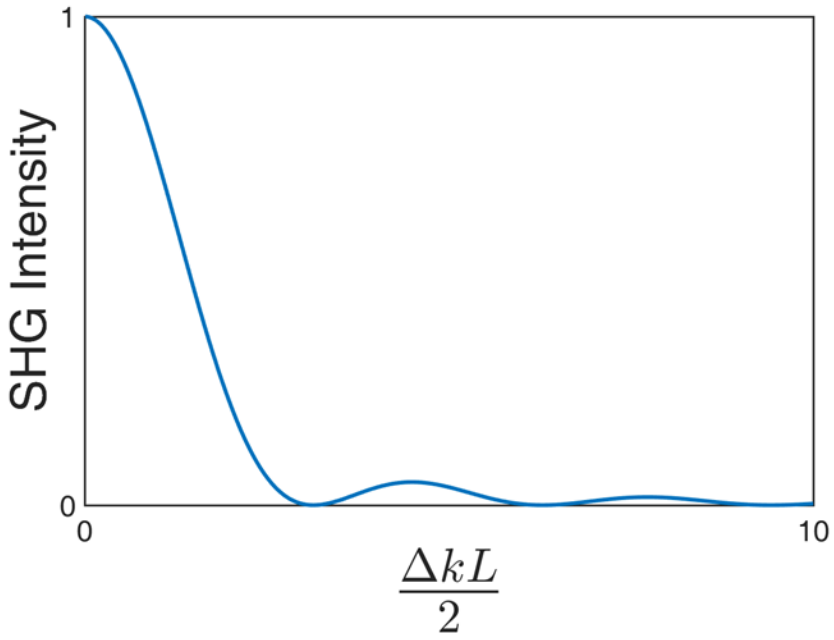

Figure 2.6: Plot of intensity profile vs. $\frac{\Delta kL}{2}$

index increases with frequency in general [and so, $n(\omega_1) \neq n(2\omega_1)$], which violates a necessary requirement for the condition to hold.

For the case when $\Delta kL \neq 0$, the intensity falls off as shown by the sinc-squared function. This is the *non-perfect phase matching* and we observe local maxima given by $\frac{\Delta kL'}{2} = b\frac{\pi}{2}$, where b includes odd integers. This gives

$$\frac{2\Delta n\omega L'}{2c} = b\frac{\pi}{2} \tag{2.26}$$

$$\frac{4\Delta n\pi L'}{2\lambda} = b\frac{\pi}{2} \tag{2.27}$$

$$L' = b\frac{\lambda}{4\Delta n}, \quad b = 1, 3, 5, \ldots \quad . \tag{2.28}$$

The term L' is the "coherence length", which is a measure of the interaction length that can allow for higher second-harmonic generation. The smaller the refractive index difference is, the larger L' is.

There are several methods of forcing phase matching. One way is to take advantage of the anomalous dispersion property of materials that occurs close to the absorption frequency regime of the material. The frequency can be chosen so that the refractive index at the fundamental and second-harmonic frequency are equal [73, 74]. A more common approach involves the use of polarization-dependent refractive index property (or birefringence) of many

crystals for matching the indices at different wavelengths [75–77]. By setting the input light polarization to an optimal direction, the refractive indices for the ordinary fundamental and extraordinary second-harmonic polarization can be matched for maximum generation. Usually, the angle between the propagation vector and the crystal optical axis is not 0° or 90°, leading to walk-off between the ordinary and extraordinary rays. For isotropic materials (possessing no birefringence), periodic poling of the structure, during fabrication or by using an external field, can be used to increase the second-order generation [78, 79]. The poling can be implemented in such a way that the optical axis of the material is periodically inverted as a function of position within the material. This results in the inversion of the coupling coefficient which compensates for the phase mismatch.

2.4 SHG microscopy

SHG microscopy aims to extract images from the second-harmonic signals generated by a sample. It has emerged as a useful modality for imaging crystals [80–82] and assessing surface properties [4, 83, 84]. First demonstrated for biological applications by Freund *et al.* in 1986 [85], it has grown to find applications in tissue imaging [86, 87], neuron imaging [88–90] and studies of components such as myosin, tubulin and membrane potential measurements [70, 91]. A common feature of these samples is the probing-light-wavelength-order non-centrosymmetry. While from a crystallographic point of view, collagen molecules have been classed as pseudo-tetragonal or orthorhombic, as described in Section 2.1.1, optical SHG averages the molecular properties over dimensions on the order of the light wavelength leading to disappearance of local symmetries. The resulting effect is that the incident light typically encounters cylindrical symmetry along the long axis (implying C_∞, which is itself non-centrosymmetric) [39].

A typical microscopy setup is shown in Fig. 2.7. A mode-locked femtosecond pulsed laser (such as a titanium-sapphire, or Ti:sapph laser) is commonly used as the source, since it generates ultrashort pulsed fields (less than 100 fs) which provide suitable temporal photon bunching required for appreciable SHG efficiency. For a given average power, shorter pulses imply higher pulse peak power which yields higher SHG intensities. However, it may be

quite difficult for extremely short pulses to get to the sample plane as they broaden nonlinearly through optical components.

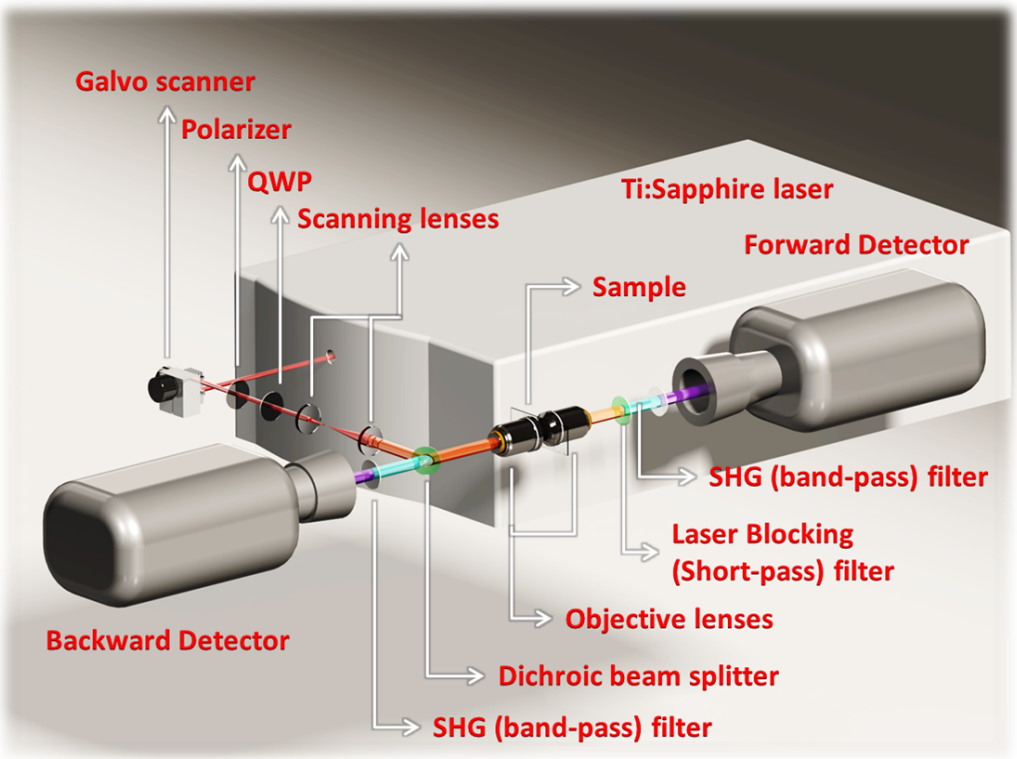

Figure 2.7: Typical SHG microscopy setup (courtesy Tung Yuen Lau)

As a point scanning technique, SHG images can be acquired by scanning the sample or the galvanometer. The latter (more widely used) has the advantage of having faster acquisition times, due to the possibility of moving scanning mirrors quite fast ($\sim$ kHz range), though the field-of-view is limited. The reverse holds when scanning the sample, as there is theoretically infinite field-of-view achievable, although the image acquisition time can be orders of magnitude longer. The setup shown implements beam scanning using galvanometer scanning mirrors which sweep the beam through scanning lenses and an objective lens across the sample.

The use of an objective (as a condenser) for focusing the beam enables not only point-by-point image reconstruction, but also increased SHG efficiency via spatial photon crowding, as well as 3-D sectioning due to the focal volume only having high enough intensity to generate an appreciable second-harmonic signal. In addition, there is a relative axial phase shift in field due to focusing which produces the interesting effect of modulating the

propagation direction of the generated second-harmonic signals. This phase shift (called the Gouy shift [92]), localized in the focal volume, causes the SHG signals from uniformly distributed molecules to be directed along symmetric lobes so as to conserve momentum (as shown in Fig. 2.8). Note

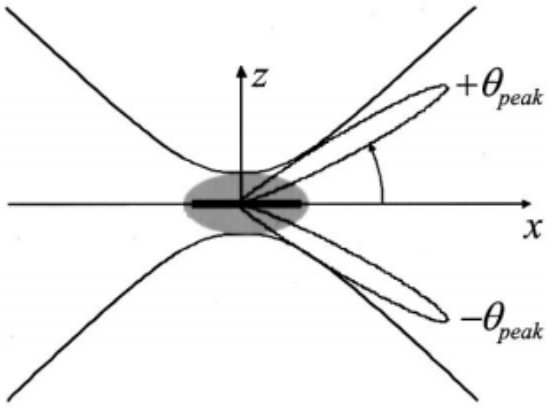

Figure 2.8: A Gaussian beam propagating along the x-direction, polarized along the z-direction and focused onto a sample with uniformly distributed molecules radiates a double-peaked SHG field. Reprinted with permission from Ref [93], OSA.

that this holds for uniformly distributed molecules, while other angular patterns emerge for more complicated structures. For example, 25% of the SHG power is radiated in backward directed lobes for a molecular distribution having $\sim \frac{\lambda}{4}$ axial periodicity and forward-backward dipolar SHG results in the case of tightly clustered molecules [94]. The total back-scattered signals receive contributions from the direct backward signal generation and forward signals that have been redirected back towards the source [95].

Since SHG occurs in forward and backward directions, detectors can be placed in both paths. The higher-intensity forward-detected SHG is collected via another objective-tube lens combination and separated from the fundamental using short-pass and/or bandpass filters. For the backward SHG signal (which is weaker in intensity), the condenser serves as the collection objective and the dichroic mirror as a bandpass filter to block out the linearly scattered light. As in linear imaging, the resolution is dependent on the wavelength of the excitation light (λ) and the numerical aperture (NA) of the objectives used. The theoretical lateral resolution achievable by SHG microscopy is $\frac{0.36\lambda}{NA}$ while the axial resolution is given by $\frac{0.7n\lambda}{NA^2}$ [96], where n

is the refractive index of the medium and λ is the excitation wavelength.

2.4.1 Quantitative SHG microscopy

The importance of objectively characterizing collagen samples while imaging, especially with assessment and diagnostic aims in mind, is increasingly being recognized. This has driven the increase in quantitative SHG-based imaging techniques applied to collagen.

An example is the forward to backward (F/B) SHG intensity ratio which has been used to highlight differences in morphology and content between various tissues [97–99]. This is because in biological matter like collagen, second-harmonic emission directionality and conversion efficiency depend on several factors such as fibril size structure, packing density and excitation direction [97]. Typically, forward-detected signals have higher intensity and

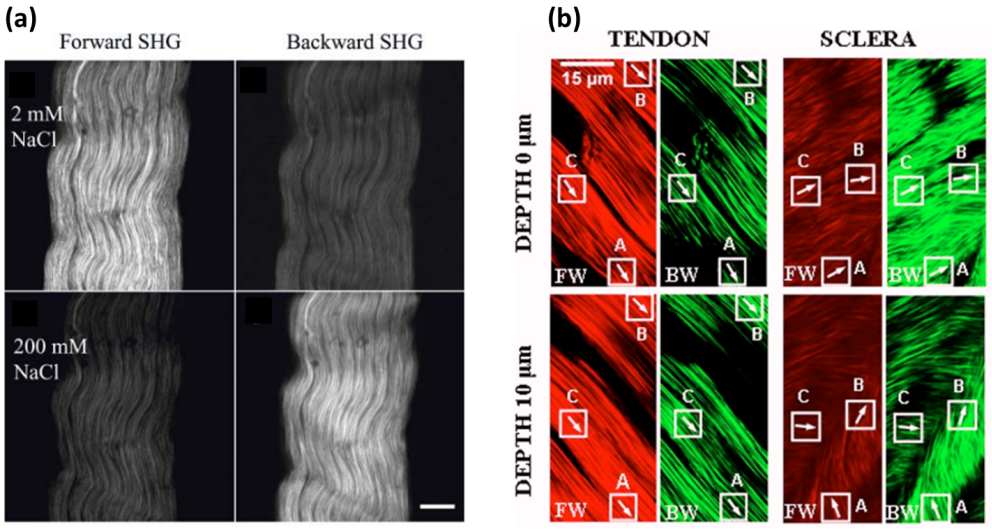

Figure 2.9: (a) F/B ratio depends on the ionic strength of solution around collagen fibrils. Reprinted with permission from Ref [98], Cell Press. (b) Assessment of collagen fiber orientation in tendon and sclera for forward (red) and backward (green) SHG images at different depths. Reprinted with permission from Ref [99], OSA.

longer coherence lengths than the backward-detected signals. The coherence disparity is because of the multiply scattered signals that contribute majorly to the backward signals. Forward-to-backward ratio can be used to assess the axial size of scatterers within the second-harmonic generating volume and to

sense ionic strength in solutions around the sample (as shown by differences in forward and backward signals for differing ionic strengths in Fig. 2.9a) [98]. It has also been applied in depth-dependent quantitative orientation analysis comparison between porcine tendon, sclera and ear cartilage (Fig. 2.9b) [99].

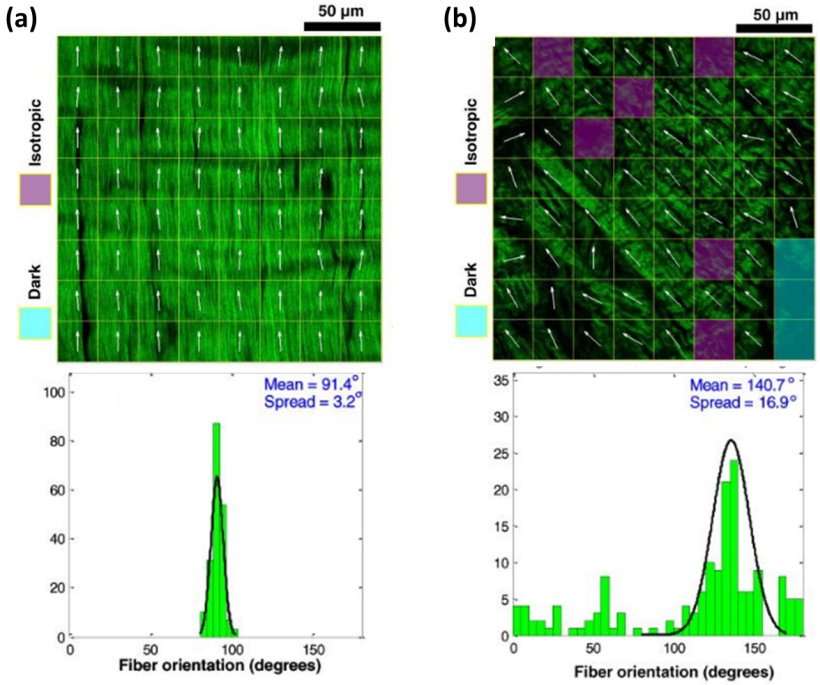

Figure 2.10: Collagen fiber preferred orientation map (top) and the histogram of orientation angles for (a) normal and (b) injured horse tendon, quantifying the disorganization of fibers due to injury. Reprinted with permission from Ref [100], OSA.

Fourier-transform (FT-) SHG and associated orientation analysis methods are series of SHG image acquisition and processing techniques applied towards analysis of fiber orientation, spacing and structural organization in SHG images. For example our group employed FT-SHG to obtain metrics that capture the preferred orientation and maximum spatial frequency of collagen fibers in porcine trachea, ear and cornea, where it was observed that trachea showed the comparatively largest variations in derived metrics [101]. In other studies, our group applied this method to assess collagen fibers in porcine bone [102], to quantify collagen orientation in breast biopsies [103] and to evaluate differences in collagen between normal and injured horse ten-

don [100] (Fig. 2.10). The analysis was further extended in work from our group, to three dimensions, and used to extract fiber orientation in porcine sclera [99].

Quantifying optical anisotropic properties of collagen is done using several polarization-resolved (PR-) SHG methods [104]. For example, the d-ratio analysis which involves second-order susceptibility d-parameters ($d \approx \frac{1}{2}\chi^{(2)}$) was used in studies of melanoma tumor tissues [105] (Fig. 2.11a). Furthermore, our group utilized this approach to assess stromal collagen in breast tissue microarrays with different pathological conditions, and showed the potential for distinguishing differences across pathologies [106] (Fig. 2.11b).

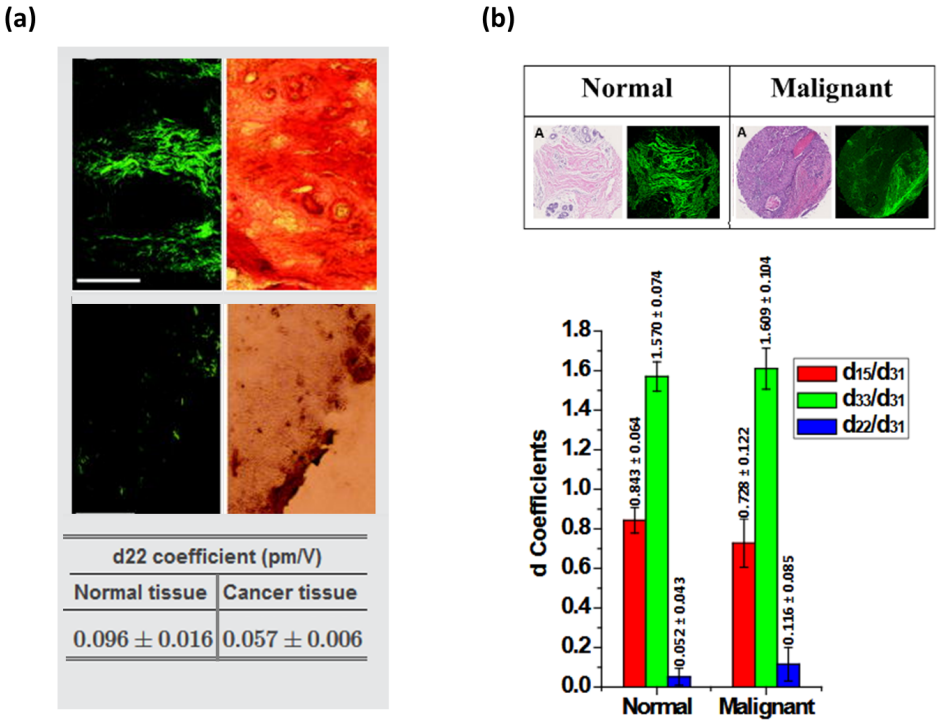

Figure 2.11: (a) SHG (left) and brightfield (right) images of normal skin (top) and melanoma (middle) along with extracted d-coefficient value comparison (bottom). Reprinted with permission from Ref [105], SPIE. (b) Brightfield (pink) and SHG (green) images for normal and malignant breast tissues, along with the d-coefficient comparison plots (bottom). Reprinted with permission from Ref [106], OSA.

Notwithstanding the potential utility of this approach, methods employing extraction of these d-parameters are hampered by the requirement to accu-

rately model the biological tissue, often with some particular crystallographic symmetry.

CHAPTER 3

POLARIMETRIC IMAGING

3.1 Polarization

The polarization of a field specifies the direction of geometric oscillations. The field at a given point rapidly fluctuates as a function of time, and is generally different, to a degree, from the field at another point (or from the same point at another time). This is the general concept behind coherence in several degrees of freedom (spatial, temporal or polarization) [107] which we have shown to be convertible from one degree of freedom to another (at least for the spatio-polarization case) [108]. The similarity of the points is captured mathematically by the cross-correlation between the two points $(\boldsymbol{U_1}(\boldsymbol{r_1}, t_1)\boldsymbol{U_2^*}(\boldsymbol{r_2}, t_2))$ where the superscript $*$ stands for the conjugate transpose operator. When all points in the field are considered, the cross-correlation is expressed as an averaging across space and time. Assuming the fluctuations are stationary (at least in the wide-sense) and ergodic, we can proceed to describe the mutual field coherence as a correlation function given by:

$$\begin{aligned} G_{12}(\boldsymbol{r_1}, \boldsymbol{r_2}, \tau) &= \langle \boldsymbol{U_1}(\boldsymbol{r_1}, t)\boldsymbol{U_2^*}(\boldsymbol{r_2}, t+\tau)\rangle \\ &= \lim_{T\to\infty} \frac{1}{2T} \int \boldsymbol{U_1}(\boldsymbol{r_1}, t)\boldsymbol{U_2^*}(\boldsymbol{r_2}, t+\tau)dt \quad . \end{aligned} \tag{3.1}$$

Normalizing by the root-product of the field intensities gives the complex degree of coherence:

$$g_{12}(\boldsymbol{r_1}, \boldsymbol{r_2}, \tau) = \frac{G_{12}(\boldsymbol{r_1}, \boldsymbol{r_2}, \tau)}{\sqrt{I(r_1)I(r_2)}} \quad , \quad 0 \leq |g_{12}, (\boldsymbol{r_1}, \boldsymbol{r_2}, \tau)| \leq 1 \quad , \tag{3.2}$$

where $I(r_1) = U(r_1)U^*(r_1)$ and $I(r_2)) = U(r_2)U^*(r_2)$.

The analysis for polarization requires evaluation of fluctuation correlations

along two chosen direction bases (instead of two points for spatial coherence or different times for temporal coherence). For a given point ($\boldsymbol{r_1} = \boldsymbol{r_2}$), if the vector fields are represented as having scalar components along orthogonal x and y vector directions, the correlation functions are given as

$$\begin{aligned} G_{xx}(\tau) &= \langle U_x(t) U_x^*(t+\tau) \rangle \\ G_{yy}(\tau) &= \langle U_y(t) U_y^*(t+\tau) \rangle \\ G_{xy}(\tau) &= \langle U_x(t) U_y^*(t+\tau) \rangle = G_{yx}^*(\tau) \quad . \end{aligned} \tag{3.3}$$

Combining the four correlation functions into a 2×2 matrix yields the Hermitian coherency density matrix.

$$\begin{aligned} \boldsymbol{G} = \begin{pmatrix} G_{xx} & G_{xy} \\ G_{yx} & G_{yy} \end{pmatrix} &= \begin{pmatrix} \langle U_x U_x^* \rangle & \langle U_x U_y^* \rangle \\ \langle U_y U_x^* \rangle & \langle U_y U_y^* \rangle \end{pmatrix} \\ &= \left\langle \begin{pmatrix} U_x \\ U_y \end{pmatrix} \begin{pmatrix} U_x^* & U_y^* \end{pmatrix} \right\rangle \\ &= \left\langle \boldsymbol{J} \otimes \overline{\boldsymbol{J}} \right\rangle \quad . \end{aligned} \tag{3.4}$$

$\boldsymbol{J}$ is the well-known Jones vector of the field, the superscript represents the complex conjugate transpose operator and the ensemble averaging of their outer product yields the density matrix.

3.1.1 Jones calculus

For a monochromatic polarized field, the **Jones vector** is sufficient to characterize the field properties.

$$\boldsymbol{J} = \begin{pmatrix} U_x \\ U_y \end{pmatrix} = U_x \hat{\boldsymbol{x}} + U_y \hat{\boldsymbol{y}} \quad , \tag{3.5}$$

where $U_x = u_x e^{-j\phi_x}$ and $U_y = u_y e^{-j\phi_y}$ are complex quantities with a phase difference given by $\phi_y - \phi_x$. Table 3.1 shows the Jones vector representation for different polarizations using the coordinate map shown in Fig. 3.1. The effect of optical systems on light can be expressed as a linear matrix action on the Jones vectors. This transformation is called the **Jones matrix T**, where

$$\boldsymbol{J}_{\text{out}} = \boldsymbol{T} \boldsymbol{J}_{\text{in}} \quad , \tag{3.6}$$

Table 3.1: Jones vectors of selected polarization states

Linearly polarized	x-polarized	$\begin{pmatrix} 1 \\ 0 \end{pmatrix}$
	y-polarized	$\begin{pmatrix} 0 \\ 1 \end{pmatrix}$
	polarized at angle θ to x	$\begin{pmatrix} \cos\theta \\ \sin\theta \end{pmatrix}$
Elliptically polarized	left circularly polarized	$\frac{1}{\sqrt{2}} \begin{pmatrix} 1 \\ e^{-j\frac{\pi}{2}} \end{pmatrix}$
	right circularly polarized	$\frac{1}{\sqrt{2}} \begin{pmatrix} 1 \\ e^{j\frac{\pi}{2}} \end{pmatrix}$
	elliptically polarized with retardance ϕ w.r.t. x	$\frac{1}{\sqrt{2}} \begin{pmatrix} 1 \\ e^{-j\phi} \end{pmatrix}$

$\boldsymbol{T}$ is a 2×2 matrix and $\boldsymbol{J}_{\text{in}}$ and $\boldsymbol{J}_{\text{out}}$ represent the input and output electric fields, respectively. Unitary and non-unitary optical transformations that preserve the maximum polarization state of the field can be completely captured by Eq. 3.6. Table 3.2 shows some of these transformations. For

Table 3.2: Jones matrices for selected optical components

Polarizer	x-polarizer	$\begin{pmatrix} 1 & 0 \\ 0 & 0 \end{pmatrix}$
	y-polarizer	$\begin{pmatrix} 0 & 0 \\ 0 & 1 \end{pmatrix}$
	polarizer at angle θ to x	$\begin{pmatrix} \cos^2\theta & \sin\theta\cos\theta \\ \sin\theta\cos\theta & \sin^2\theta \end{pmatrix}$
Retarder	quarter-wave plate	$\begin{pmatrix} 1 & 0 \\ 0 & e^{-j\frac{\pi}{2}} \end{pmatrix}$
	half-wave plate	$\begin{pmatrix} 1 & 0 \\ 0 & e^{-j\pi} \end{pmatrix}$
	retarder by ϕ	$\begin{pmatrix} 1 & 0 \\ 0 & e^{-j\phi} \end{pmatrix}$

cascaded optical systems, the composite Jones matrix is the product of the individual component Jones matrices. The order of multiplication is important, going from initial to final components (since matrix multiplication is not commutative). Hence, for n cascaded systems,

$$\boldsymbol{J}_{\text{out}} = \boldsymbol{T}_n ... \boldsymbol{T}_1 \boldsymbol{J}_{\text{in}} \quad , \tag{3.7}$$

where $1, ..., n$ are the order of optical components encountered.

The Jones vector and matrix are dependent on the coordinate system chosen. If the chosen coordinate system is related to the original coordinate system by a rotation, then

$$\boldsymbol{J}' = \boldsymbol{R}(\theta)\boldsymbol{J} \tag{3.8}$$

$$\boldsymbol{T}' = \boldsymbol{R}(\theta)\boldsymbol{T}\boldsymbol{R}(-\theta) \quad , \tag{3.9}$$

where $\boldsymbol{R}(\theta)$ is the rotation matrix, and

$$\boldsymbol{R}(\theta) = \begin{pmatrix} \cos\theta & \sin\theta \\ -\sin\theta & \cos\theta \end{pmatrix} \quad . \tag{3.10}$$

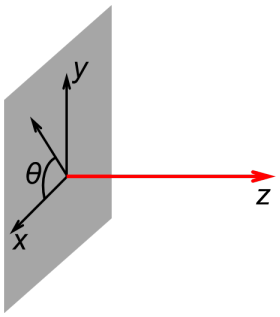

Figure 3.1: Coordinate map for electric field propagating along z and polarized along angle θ to x.

3.1.2 Mueller calculus

For fields that are not fully polarized (partially or randomly polarized), Jones calculus is inadequate for a comprehensive characterization of the field. Describing the polarization of such fields will have to incorporate field statistics, alongside measures of coherence and entropy. This necessitates the use of ensemble averaging as introduced in Eqs. 3.3 and 3.4 yielding **Stokes vectors**.

$$\boldsymbol{s} = \begin{pmatrix} s_0 \\ s_1 \\ s_2 \\ s_3 \end{pmatrix} = \begin{pmatrix} I_H + I_V \\ I_H - I_V \\ I_P - I_{P^*} \\ I_R - I_{R^*} \end{pmatrix} \quad , \tag{3.11}$$

where I is the intensity, and the subscripts H, V, P, P^*, R and R^* stand for bases at angles 0°, 90°, +45°, −45°, right-circularly polarized and left-circularly polarized respectively.

Table 3.3 shows the Stokes vector representation for different polarizations.

Table 3.3: Stokes vectors of selected polarization states

Linearly polarized	x/y-polarized	$\begin{pmatrix} 1 \\ \pm 1 \\ 0 \\ 0 \end{pmatrix}$
	$\pm 45^o$-polarized	$\begin{pmatrix} 1 \\ 0 \\ \pm 1 \\ 0 \end{pmatrix}$
	polarized at angle θ to x	$\begin{pmatrix} 1 \\ \cos^2\theta - \sin^2\theta \\ \cos^2(\frac{\pi}{4} - \theta) - \sin^2(\frac{\pi}{4} - \theta) \\ 0 \end{pmatrix}$
Elliptically polarized	left/right circularly polarized	$\begin{pmatrix} 1 \\ 0 \\ 0 \\ \pm 1 \end{pmatrix}$
	elliptically polarized with retardance ϕ w.r.t. x	$\begin{pmatrix} 1 \\ 0 \\ \cos\phi \\ \sin\phi \end{pmatrix}$
Unpolarized	also known as randomly polarized	$\begin{pmatrix} 1 \\ 0 \\ 0 \\ 0 \end{pmatrix}$

The effect of optical systems on light can be expressed as a linear matrix action on the Stokes vectors. This transformation is called the **Mueller matrix M**, where

$$\boldsymbol{s}_{\text{out}} = \boldsymbol{M}\boldsymbol{s}_{\text{in}} \quad , \tag{3.12}$$

$\boldsymbol{M}$ is a 4×4 matrix and $\boldsymbol{s}_{\text{in}}$ and $\boldsymbol{s}_{\text{out}}$ represent the input and output fields respectively. The condition of preserving maximum polarization state for unitary and non-unitary optical transformations need not be satisfied, for characterization by the Mueller matrices. Table 3.4 shows the Mueller matrix

representations for some selected optical components.

Table 3.4: Mueller matrices for selected optical components

Polarizer	x-polarizer	$\frac{1}{2}\begin{pmatrix} 1 & 1 & 0 & 0 \\ 1 & 1 & 0 & 0 \\ 0 & 0 & 0 & 0 \\ 0 & 0 & 0 & 0 \end{pmatrix}$
	y-polarizer	$\frac{1}{2}\begin{pmatrix} 1 & -1 & 0 & 0 \\ -1 & 1 & 0 & 0 \\ 0 & 0 & 0 & 0 \\ 0 & 0 & 0 & 0 \end{pmatrix}$
	polarizer at angle θ to x	$\frac{1}{2}\begin{pmatrix} 1 & \cos 2\theta & \sin 2\theta & 0 \\ \cos 2\theta & \cos^2 2\theta & \cos 2\theta \sin 2\theta & 0 \\ \sin 2\theta & \cos 2\theta \sin 2\theta & \sin^2 2\theta & 0 \\ 0 & 0 & 0 & 0 \end{pmatrix}$
Retarder	quarter-wave plate	$\begin{pmatrix} 1 & 0 & 0 & 0 \\ 0 & 1 & 0 & 0 \\ 0 & 0 & 0 & 1 \\ 0 & 0 & -1 & 0 \end{pmatrix}$
	half-wave plate	$\begin{pmatrix} 1 & 0 & 0 & 0 \\ 0 & 1 & 0 & 0 \\ 0 & 0 & -1 & 0 \\ 0 & 0 & 0 & -1 \end{pmatrix}$
	retarder by ϕ	$\begin{pmatrix} 1 & 0 & 0 & 0 \\ 0 & 1 & 0 & 0 \\ 0 & 0 & \cos\phi & -\sin\phi \\ 0 & 0 & \sin\phi & \cos\phi \end{pmatrix}$

For cascaded optical systems, the composite Mueller matrix is the product of the individual component Mueller matrices. As in the Jones matrix case, the order of multiplication is goes from initial to final components. Hence, for n cascaded systems, for which the field travels from 1...n,

$$\boldsymbol{s}_{\text{out}} = \boldsymbol{M}_n ... \boldsymbol{M}_1 \boldsymbol{s}_{\text{in}} \quad . \tag{3.13}$$

The rotation of Stokes vectors and Mueller matrices also proceeds as

$$\boldsymbol{s}' = \boldsymbol{R}_M(\theta)\boldsymbol{s} \tag{3.14}$$

$$\boldsymbol{M}' = \boldsymbol{R}_M(\theta)\boldsymbol{M}\boldsymbol{R}_M(-\theta) \quad , \tag{3.15}$$

where $\boldsymbol{R}_M(\theta)$ is the rotation matrix, and

$$\boldsymbol{R}_M(\theta) = \begin{pmatrix} 1 & 0 & 0 & 0 \\ 0 & \cos 2\theta & \sin 2\theta & 0 \\ 0 & -\sin 2\theta & \cos 2\theta & 0 \\ 0 & 0 & 0 & 1 \end{pmatrix} \quad . \tag{3.16}$$

3.2 Mueller matrix theory

This section provides a more rigorous theory of polarization from the Mueller framework.

3.2.1 Stokes vector and coherency density matrix

Starting off with $\boldsymbol{G} = \left\langle \boldsymbol{J} \otimes \overline{\boldsymbol{J}} \right\rangle$ from Eq. 3.4 and invoking Pauli matrix Lie generators of the group SU(2) irreducible Hermitian representation [109], we get

$$s_\alpha = \left\langle \overline{\boldsymbol{J}} \boldsymbol{\tau_\alpha} \boldsymbol{J} \right\rangle = \mathrm{Tr}(\langle \boldsymbol{G} \rangle \, \boldsymbol{\tau_\alpha}) \quad \alpha = 0, 1, 2, 3, \tag{3.17}$$

where

$$\begin{aligned} \boldsymbol{\tau}_0 &= \begin{pmatrix} 1 & 0 \\ 0 & 1 \end{pmatrix} \quad \boldsymbol{\tau}_1 = \begin{pmatrix} -1 & 0 \\ 0 & 1 \end{pmatrix} \\ \boldsymbol{\tau}_2 &= \begin{pmatrix} 0 & 1 \\ 1 & 0 \end{pmatrix} \quad \boldsymbol{\tau}_3 = \begin{pmatrix} 0 & j \\ -j & 0 \end{pmatrix} \end{aligned} \tag{3.18}$$

and s_α are the Stokes vector elements. The Pauli matrices are used because they form an elementary basis of the Poincaré sphere geometry, providing a connection from density matrices to Stokes vectors [110]. Substituting the Pauli matrices in Eq. 3.18 into Eq. 3.17, we can build up the Stokes vector from the elements as

$$\boldsymbol{s} = \begin{pmatrix} s_0 \\ s_1 \\ s_2 \\ s_3 \end{pmatrix} = \begin{pmatrix} 1 \\ \sigma_1 \\ \sigma_2 \\ \sigma_3 \end{pmatrix} = \begin{pmatrix} \langle U_x U_x^* \rangle + \langle U_y U_y^* \rangle \\ \langle U_x U_x^* \rangle - \langle U_y U_y^* \rangle \\ \langle U_x U_y^* \rangle + \langle U_y U_x^* \rangle \\ j(-\langle U_x U_y^* \rangle + \langle U_y U_x^* \rangle) \end{pmatrix} \quad , \tag{3.19}$$

where $\boldsymbol{s}$ is the Stokes vector and $\sigma_1, \sigma_2, \sigma_3$ are the normalized Stokes vector elements. The first two terms (s_0 and s_1) are relationships between the intensities along individual bases (no correlation terms). The next two terms (s_2 and s_3) correlate terms along orthogonal bases for in-phase (0, π) and $\frac{\pi}{2}$-phase-retardance ($\frac{\pi}{2}$, $-\frac{\pi}{2}$) conditions. Hence, the Stokes vector can be written as Eq. 3.11.

The 4×1 Stokes vector can be written in a 2×2 matrix that is more conventionally used to describe two-state systems. This is the coherency matrix introduced in Eq. 3.4, which can be expressed in terms of the Stokes elements as

$$\begin{aligned} \boldsymbol{G} = \begin{pmatrix} \langle U_x U_x^* \rangle & \langle U_x U_y^* \rangle \\ \langle U_y U_x^* \rangle & \langle U_y U_y^* \rangle \end{pmatrix} &= \begin{pmatrix} \langle s_0 \rangle + \langle s_1 \rangle & \langle s_2 \rangle - j\langle s_3 \rangle \\ \langle s_2 \rangle + j\langle s_3 \rangle & \langle s_0 \rangle - \langle s_1 \rangle \end{pmatrix} \\ &= \begin{pmatrix} 1 + \langle \sigma_1 \rangle & \langle \sigma_2 \rangle - j\langle \sigma_3 \rangle \\ \langle \sigma_2 \rangle + j\langle \sigma_3 \rangle & 1 - \langle \sigma_1 \rangle \end{pmatrix} \quad . \end{aligned} \tag{3.20}$$

The diagonal elements represent the average intensities along the orthogonal bases, and the off-diagonal elements represent the cross-correlation terms. The trace of the coherency matrix represents the average total intensity of the optical field.

3.2.2 Polarization visualization

The expression in Eq. 3.19 can further be analyzed by substituting the definitions $U_x = u_x e^{-j\phi_x}$ and $U_y = u_y e^{-j\phi_y}$. Given that $\phi = \phi_y - \phi_x$, we obtain

$$s_0 = u_x^2 + u_y^2 \tag{3.21}$$

$$s_1 = u_x^2 - u_y^2 \tag{3.22}$$

$$s_2 = u_x u_y e^{j\phi} + u_x u_y e^{-j\phi} \qquad = 2u_x u_y \cos\phi \tag{3.23}$$

$$s_3 = -j(u_x u_y e^{j\phi} - u_x u_y e^{-j\phi}) \qquad = 2u_x u_y \sin\phi \quad . \tag{3.24}$$

In these equations, we assume that the field is stationary and ergodic. Hence the averaging of the instantaneous Stokes vector translates to the usual Stokes parameters given in Eqs. 3.21 to 3.24. The equations can be visualized using the polarization ellipse (Fig. 3.2), and parameters such as ellipticity (χ) and

orientation (ψ) can also be understood from a geometric perspective.

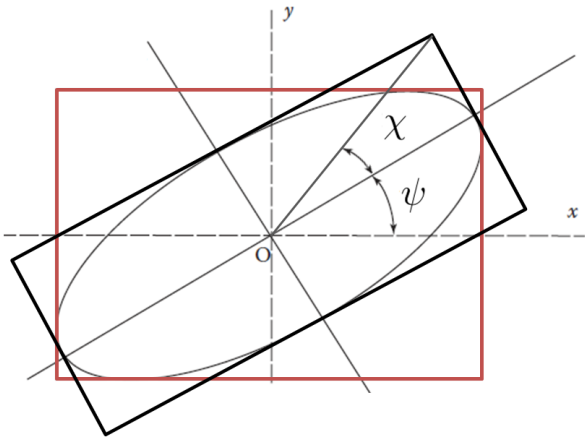

$$\begin{aligned} &\text{orientation} \\ \tan 2\psi &= \frac{2u_x u_y \cos\phi}{u_x^2 - u_y^2} \\ &= \cos\phi \tan 2\alpha \end{aligned}$$

$$\begin{aligned} &\text{ellipticity} \\ \sin 2\chi &= \frac{2u_x u_y \sin\phi}{u_x^2 + u_y^2} \\ &= \sin\phi \sin 2\alpha \end{aligned}$$

$$\begin{aligned} \phi &= \phi_y - \phi_x \\ \tan\alpha &= \frac{u_y}{u_x} \end{aligned}$$

Figure 3.2: Polarization ellipse.

In general,

$$s_0^2 \geq \sum_{n=0}^{3} s_n^2 \quad . \tag{3.25}$$

The equality condition holds for only fully polarized light, while for partially polarized light, the extent of polarization (called the degree-of-polarization, p) is given by $\frac{\sqrt{\sum_{n=0}^{3} s_n^2}}{s_0}$. The Mueller framework has a clear advantage over Jones calculus in describing partially polarized or unpolarized light. Figure 3.3 shows the Poincaré sphere space for which a field can be represented by a point in the volume. Fully polarized light is represented by a point that lies on the surface, and partially polarized light exists in the sphere volume. The closer to the radius the point is, the less the degree-of-polarization, and at the center, we obtain completely unpolarized light.

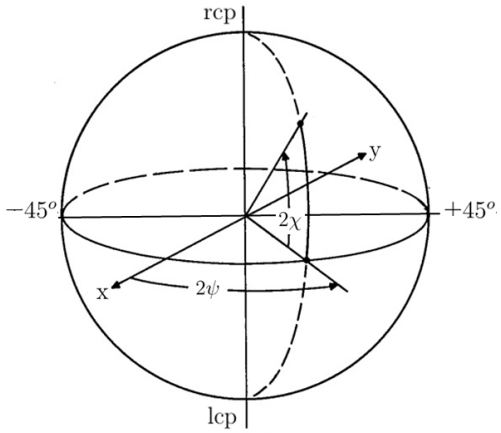

orientation

$$\tan 2\psi = \frac{s_2}{s_1}$$

ellipticity

$$\sin 2\chi = \frac{s_3}{s_0}$$

$$\tan \phi = \frac{s_3}{s_2}$$

Figure 3.3: The Poincaré sphere.

3.2.3 Mueller matrix properties

The Mueller matrix is a 4×4 matrix composed of real numbers, since Stokes vectors deal with intensities.

$$\boldsymbol{M} = \begin{pmatrix} m_{00} & m_{01} & m_{02} & m_{03} \\ m_{10} & m_{11} & m_{12} & m_{13} \\ m_{20} & m_{21} & m_{22} & m_{23} \\ m_{30} & m_{31} & m_{32} & m_{33} \end{pmatrix} \quad . \tag{3.26}$$

Not all 4×4 matrices can be Mueller matrices. For example, a matrix that acts on a valid incident Stokes vector to produce an output vector with degree-of-polarization greater than one is not physically realizable. The space of all possible Mueller matrices has been referred to as **physically realizable Mueller matrices** [111, 112]. Supposing $\boldsymbol{G} = \mathrm{diag}(1, -1, -1, -1)$, it was shown by Givens and Kostinski that a given Mueller matrix $\boldsymbol{M}$ is not overpolarizing, and hence physically realizable, if and only if the spectrum (or set of eigenvalues) of $\boldsymbol{GM}^T\boldsymbol{GM}$ is real and the eigenvector associated with the largest eigenvalue is a physical Stokes vector, that is, its degree of polarization is not greater than one [111]. From the interpretation of this, a few necessary conditions for a Mueller matrix to be physically realizable are (Ch. 22 of Ref [113])

- $m_{00} \geq |m_{ij}|$
- $m_{00}^2 \geq \sqrt{m_{01}^2 + m_{02}^2 + m_{03}^2}$

- $m_{00}^2 \geq \frac{1}{4}\mathrm{Tr}(\boldsymbol{M}\boldsymbol{M}^T)$

where $i, j \in \{0, 1, 2, 3\}$, the operator Tr() stands for the trace of the matrix and the superscript T is the transpose operator.

A subspace within physically realizable Mueller matrices consists of those matrices which have Jones matrix equivalents; these Mueller matrices are called **nondepolarizing Mueller matrices** or **Mueller-Jones matrices**. To show the condition for such matrices, we start off with writing the coherency density matrix in vector form as

$$\boldsymbol{C} = \begin{pmatrix} \langle U_x U_x^* \rangle \\ \langle U_x U_y^* \rangle \\ \langle U_y U_x^* \rangle \\ \langle U_y U_y^* \rangle \end{pmatrix} = \langle \boldsymbol{J} \otimes \boldsymbol{J}^* \rangle \,, \tag{3.27}$$

where * denotes the conjugate transpose. The Stokes vector can then be written as

$$\boldsymbol{s} = \begin{pmatrix} 1 & 0 & 0 & 1 \\ 1 & 0 & -1 & 0 \\ 0 & 1 & 1 & 0 \\ 0 & -j & j & 0 \end{pmatrix} \boldsymbol{C} \tag{3.28}$$

$$\boldsymbol{s} = \boldsymbol{A}\boldsymbol{C} \tag{3.29}$$

$$\boldsymbol{C} = \boldsymbol{A}^{-1}\boldsymbol{s} \quad . \tag{3.30}$$

Supposing we have an output coherency vector $\boldsymbol{C}_{out} = \langle \boldsymbol{J}_{out} \otimes \boldsymbol{J}_{out}^* \rangle$ given an input vector $\boldsymbol{C}_{in} = \langle \boldsymbol{J}_{in} \otimes \boldsymbol{J}_{in}^* \rangle$, we get

$$\begin{aligned} \boldsymbol{C}_{out} &= \langle \boldsymbol{J}_{out} \otimes \boldsymbol{J}_{out}^* \rangle \\ &= \langle \boldsymbol{T}\boldsymbol{J}_{in} \otimes \boldsymbol{T}^* \boldsymbol{J}_{in}^* \rangle \\ &= \langle \boldsymbol{T} \otimes \boldsymbol{T}^* \rangle \langle \boldsymbol{J}_{in} \otimes \boldsymbol{J}_{in}^* \rangle \\ &= \langle \boldsymbol{T} \otimes \boldsymbol{T}^* \rangle C_{in} \quad . \end{aligned} \tag{3.31}$$

By substituting in the definition of Eq. 3.30, we can write

$$\boldsymbol{A}^{-1}\boldsymbol{s}_{out} = \langle \boldsymbol{T} \otimes \boldsymbol{T}^* \rangle \boldsymbol{A}^{-1}\boldsymbol{s}_{in} \tag{3.32}$$

$$\boldsymbol{s}_{out} = \boldsymbol{A} \langle \boldsymbol{T} \otimes \boldsymbol{T}^* \rangle \boldsymbol{A}^{-1}\boldsymbol{s}_{in} \quad . \tag{3.33}$$

The Mueller-Jones matrices have a relationship with the Jones matrices described as

$$\boldsymbol{M} = \boldsymbol{A} \left\langle \boldsymbol{T} \otimes \boldsymbol{T}^{*} \right\rangle \boldsymbol{A}^{-1} \quad . \tag{3.34}$$

Hence, a given Mueller matrix $\boldsymbol{M}$ is a Mueller-Jones matrix if $\boldsymbol{A}^{-1}\boldsymbol{M}\boldsymbol{A}$ can be factored into the form $\boldsymbol{T} \otimes \boldsymbol{T}^{*}$

3.2.4 Mueller matrix parameters

The Mueller matrix formalism is a heuristic and comprehensive approach (relative to Jones matrix) for characterizing system polarization effect on light. In this section, we describe the matrix and scalar parameters that can be extracted from the Mueller matrix. It should be noted that each derivable matrix is in itself a Mueller matrix.

Diattenuation is a measure of the polarization-dependent transmittance of a system. This means that the amplitude of the field transmitted through a diattenuator changes with its polarization state. For a pure diattenuator, the change in transmittance goes from a maximum along the transmission-axis to a minimum at an axis orthogonal to the transmission-axis, following a cosine-squared curve. The diattenuator achieves this by either having absorptance or reflectance that depends on the polarization. The diattenuation representation matrix is a non-unitary transformation matrix since it does not preserve the inner-product of the Stokes vector after the transformation. The scalar diattenuation parameter D_m can be defined as

$$D_m = \frac{|T_{m_1} - T_{m_2}|}{T_{m_1} + T_{m_2}}, \quad 0 \leq D \leq 1 \quad , \tag{3.35}$$

where T_{m_1} and T_{m_2} are the maximum and minimum transmittances measured and their axes are the eigenpolarizations (m_1, m_2) of the system. A polarizer is a pure diattenuator, and it can have eigenpolarizations along any of the cardinal bases of the Poincaré sphere, that is x-y, $\pm 45^{\circ}$ or RCP/LCP.

Another property, the **retardance**, is a measure of the polarization-dependent optical pathlength (or equivalently, refractive index) of a system. The retardance representation matrix is a unitary transformation matrix, since it preserves the inner-product of the Stokes vector after the transformation. This

means that the intensities before and after the transformation are the same. Its effect is on the phase difference between the eigenpolarizations (referred to as fast-axis and slow-axis). The scalar retardance parameter R_m can be expressed as

$$R_m = |\delta_{m_1} - \delta_{m_2}|, \quad 0 \leq R \leq \pi \quad , \tag{3.36}$$

where δ_{m_1} and δ_{m_2} are the phase changes along the eigenpolarization axes (m_1, m_2). The fast-axis is that with the leading phase (or lower phase change). A retarder can also have its eigenpolarizations along x-y, $\pm 45^o$ or rcp-lcp.

Table 3.5: Effect of diattenuator and retarder along selected bases on linearly (x-y and $\pm 45°$) and circularly (rcp-lcp) polarized light

	Effect Axes	**Effect on Linear Input**	**Effect on Circular Input**
Diattenuator	x-y	Linear (linear for 100% diattenuation)	Elliptical (linear for 100% diattenuation)
	$\pm 45°$	Linear (linear for 100% diattenuation)	Elliptical (linear for 100% diattenuation)
	rcp-lcp	Elliptical (circular for 100% diattenuation)	Elliptical (linear for 100% diattenuation)
Retarder	x-y	Elliptical (circular for 90° retarder)	Elliptical (linear for 90° retardance)
	$\pm 45°$	Elliptical (circular for 90° retardance)	Elliptical (linear for 90° retardance)
	rcp-lcp	Rotated Linear (90° rotation for 90° retardance)	Circular

Table 3.5 shows the effect of diattenuators and retarders along different bases (x-y, $\pm 45°$, rcp-lcp) on different linear and circular polarized light. It should be noted that the diattenuation and the retardance can be represented by Jones matrices, with close analogy to the relationships already given [114]. Jones matrices are unable to capture **depolarization**: the measure of how uncorrelated orthogonal components of a field are. A depolarization representation matrix is however valid within the Mueller framework, and the depolarization scalar Δ_m can be thought of as affecting the bases (m_1, m_2), and $0 \leq \Delta \leq 1$. Table B.1 in Appendix B.2 defines some parameters that can be extracted from the Mueller matrix.

3.2.5 Mueller matrix decomposition

Decomposition of a Mueller matrix is important because it breaks up a matrix into constituent submatrices with their associated derivable scalars that can provide insight into the different properties with optical significance. To motivate this, suppose the matrix of an element is obtained to be

$$\boldsymbol{M} = \begin{pmatrix} 1 & 0 & 0 & 0 \\ -1 & 0 & 0 & 0 \\ 0 & 0 & 0 & 0 \\ 0 & 0 & 0 & 0 \end{pmatrix} \quad . \tag{3.37}$$

On the surface it looks like a purely vertical linear polarizer, since it does indeed produce the normalized Stokes vector $(1000)^T$ when it acts on any polarized state. However, decomposing it to

$$\boldsymbol{M} = \begin{pmatrix} 1 & 0 & 0 & 0 \\ -1 & 0 & 0 & 0 \\ 0 & 0 & 0 & 0 \\ 0 & 0 & 0 & 0 \end{pmatrix} = \frac{1}{2} \begin{pmatrix} 1 & -1 & 0 & 0 \\ -1 & 1 & 0 & 0 \\ 0 & 0 & 0 & 0 \\ 0 & 0 & 0 & 0 \end{pmatrix} \begin{pmatrix} 1 & 0 & 0 & 0 \\ 0 & 0 & 0 & 0 \\ 0 & 0 & 0 & 0 \\ 0 & 0 & 0 & 0 \end{pmatrix} \tag{3.38}$$

reveals its nature as a depolarizer followed by a vertical linear polarizer. Indeed, the difference is noted in the effect on vertically polarized input. The output is vertically polarized for both, but the intensity out of the purely vertical polarizer is twice that of the composite case.

Various decomposition approaches have been used in order to extract optically meaningful sub-matrices. For example, Mueller matrices have been decomposed into the sum of nondepolarizing Mueller matrices [115] and product of two nondepolarizing Mueller matrices sandwiched by a diagonal Mueller matrix [116]. Following is a description of two decomposition techniques.

Polar decomposition

The Mueller matrix polar decomposition approach as described by Lu and Chipman [117] expresses a Mueller matrix as a product of depolarization,

retardance and diattenuation matrices such that

$$\boldsymbol{M} = \boldsymbol{M_\Delta M_R M_D} \quad , \tag{3.39}$$

where

$$\boldsymbol{M_\Delta} = \begin{pmatrix} 1 & \vec{0}^T \\ \vec{P}_\Delta & \boldsymbol{m_\Delta} \end{pmatrix}, \quad \boldsymbol{M_R} = \begin{pmatrix} 1 & \vec{0}^T \\ \vec{0} & \boldsymbol{m_R} \end{pmatrix}, \quad \boldsymbol{M_D} = \begin{pmatrix} 1 & \vec{D}^T \\ \vec{D} & \boldsymbol{m_D} \end{pmatrix} \quad , \tag{3.40}$$

$\boldsymbol{m_\Delta}$, $\boldsymbol{m_R}$ and $\boldsymbol{m_D}$ are the 3×3 depolarization, retardance and diattenuation sub-matrices respectively, $\vec{P}_\Delta$ is the so-called polarizance vector and $\vec{D} = \begin{pmatrix} D_1 \\ D_2 \\ D_3 \end{pmatrix}$ is the diattenuation vector. Substituting Eq. 3.40 into 3.39 gives

$$\boldsymbol{M} = \begin{pmatrix} 1 & \vec{D}^T \\ \vec{P}_\Delta + \boldsymbol{m_\Delta m_R m_D} & \vec{P}_\Delta \vec{D}^T + \boldsymbol{m_\Delta m_R m_D} \end{pmatrix} \quad . \tag{3.41}$$

The matrices, and associated scalars retrieved, can be used as sample assessment tools [118–121]. The steps for polar decomposition after retrieving the Mueller matrix are explained in Appendix B.2. One thing to note is that since matrix multiplication is not commutative, the three factors in the polar decomposition are order dependent, yielding six different decompositions. Also, it is important to note that this decomposition does not work for singular (non-invertible) matrices, such as pure polarizers and retarders.

Differential decomposition

One shortcoming of the polar decomposition method is that it assumes that the optical effects happen consecutively (and not necessarily simultaneously) requiring multiplicative matrices that are order dependent. One decomposition effect that addresses this is the differential decomposition analysis [122–124], which relates the Mueller matrix to the spatial derivative along the light propagation direction.

We follow the derivation from Azzam [122] to obtain the differential decomposition matrix. Supposing we have light propagate through a thin slab

of medium of width Δz, the Stokes input and output vectors are related by

$$\boldsymbol{s}_{z+\Delta z} = \boldsymbol{M}_z \boldsymbol{s}_z \quad , \tag{3.42}$$

where $\boldsymbol{M}_z$ is the Mueller matrix of the thin slab. Subtracting $\boldsymbol{s}_z$ from both sides and dividing by Δz

$$\frac{\boldsymbol{s}_{z+\Delta z} - \boldsymbol{s}_z}{\Delta z} = \frac{(\boldsymbol{M}_z - \boldsymbol{I})\boldsymbol{s}_z}{\Delta z} \tag{3.43}$$

and taking the limit as $\Delta z \to 0$, we obtain

$$\frac{d\boldsymbol{s}_z}{dz} = \boldsymbol{M}^{(d)} \boldsymbol{s}_z \tag{3.44}$$

where $\boldsymbol{M}^{(d)} = lim_{\Delta z \to 0} \frac{(\boldsymbol{M}_z - \boldsymbol{I})}{\Delta z}$ is the differential propagation matrix. To describe the relationship with the measured Mueller matrix in a given homogeneous longitudinal distance, we start by relating input and output Stokes vectors separated by distance z.

$$\boldsymbol{s}_z = \boldsymbol{M}_z \boldsymbol{s}_0 \tag{3.45}$$

Differentiating both sides with respect to z,

$$\frac{d\boldsymbol{s}_z}{dz} = \frac{d\boldsymbol{M}_z}{dz} \boldsymbol{s}_0 \quad . \tag{3.46}$$

Substituting Eq. 3.44 into 3.46, we get

$$\boldsymbol{M}^{(d)} \boldsymbol{s}_z = \frac{d\boldsymbol{M}}{dz} \boldsymbol{s}_0 \tag{3.47}$$

$$\boldsymbol{M}^{(d)} \boldsymbol{M}_z \boldsymbol{s}_0 = \frac{d\boldsymbol{M}_z}{dz} \boldsymbol{s}_0 \quad . \tag{3.48}$$

We can see that

$$\frac{d\boldsymbol{M}_z}{dz} = \boldsymbol{M}^{(d)} \boldsymbol{M}_z \quad . \tag{3.49}$$

With the assumption that the differential matrix does not depend on z, we

solve the differential equation to obtain

$$\boldsymbol{M}_z = e^{\boldsymbol{M}^{(d)} z} \tag{3.50}$$

$$\ln \boldsymbol{M}_z = \boldsymbol{M}^{(d)} z \tag{3.51}$$

$$\boldsymbol{L} = \boldsymbol{M}^{(d)} z \quad , \tag{3.52}$$

where $\boldsymbol{L}$ is defined as the matrix logarithm of the measured Mueller matrix. For a given medium, the differential matrix $\boldsymbol{M}^{(d)}$ can expressed as [123].

$$\boldsymbol{M}^{(d)} = \begin{pmatrix} \alpha & \beta & \gamma & \delta \\ \beta' & \alpha_1 & \mu & \nu \\ \gamma' & -\mu' & \alpha_2 & \eta \\ \delta' & -\nu' & -\eta' & \alpha_3 \end{pmatrix} \quad , \tag{3.53}$$

where $\alpha, \alpha_1, \alpha_2, \alpha_3$ are the absorption values along total, x-y, $\pm 45°$ axes and circular axes respectively. $[\beta, \beta']$ are the linear diattenuation values along the xy axes, $[\gamma, \gamma']$ are the linear diattenuation values along the $\pm 45°$ axes, $[\delta, \delta']$ are the circular diattenuation values, $[\eta, \eta']$ are the linear retardance values along the xy axes, $[\nu, \nu']$ are the linear retardance values along the $\pm 45°$ axes and $[\mu, \mu']$ are the circular retardance values. For nondepolarizing media, $\alpha = \alpha_1 = \alpha_2 = \alpha_3$, $\delta = \delta'$, $\eta = \eta'$, $\nu = \nu'$ and $\mu = \mu'$ giving 7 independent elements.

Once we extract a sample Mueller matrix $\boldsymbol{M}_z$, and can obtain the matrix logarithm $\boldsymbol{L}$, we gain access to differential propagation matrix $\boldsymbol{M}^{(d)}$, from which we can derive the aforementioned optical properties.

3.3 Mueller matrix polarimetry

The experimental setup and analysis required to retrieve the Mueller matrix of a sample is called Mueller matrix polarimetry. It essentially involves measuring series of Stokes vector outputs, given pre-selected input states and solving the system of equations generated. A minimum of 16 measurements are required, so as to recover the representative matrix, that is 4 output states for 4 input states. However, it is common (and even encouraged) to take many more measurements, so as to reduce the effect of noise. Figure 3.4 is a block diagram illustrating the components required to build up a Mueller

matrix polarimeter. A source and detector are used for illumination and sig-

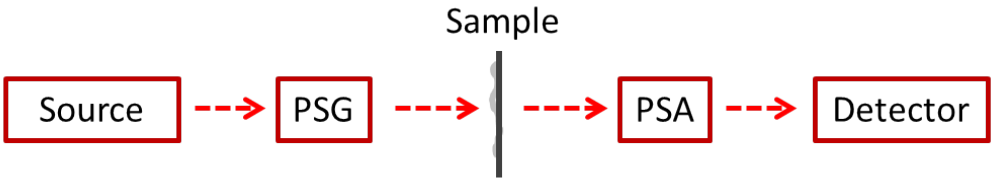

Figure 3.4: Components of a Mueller matrix polarimeter.

nal detection. The PSG (or polarization state generator) prepares the input states that probe the sample, while the PSA (or polarization state analyzer) analyzes the output state. Tables A.1 and A.2 give the angle settings for the PSG and PSA combinations, when using discrete optical components. For a given set of n input Stokes vectors and a minimum of four independent output Stokes vector measurements, the Mueller matrix $\boldsymbol{M}$ can be uniquely determined by concatenating the vectors into matrices, and inverting such that (Ch. 22 of Ref [113])

$$\boldsymbol{M} = \left(\boldsymbol{s_{o1}} \cdots \boldsymbol{s_{on}}\right) \left(\boldsymbol{s_{i1}} \cdots \boldsymbol{s_{in}}\right)_P^{-1} \quad , \tag{3.54}$$

where $()_P^{-1}$ represents the pseudo-inverse operator and n (> 4) is the number of PSG configurations used in the measurements.

CHAPTER 4

MUELLER MATRIX SECOND-HARMONIC GENERATION MICROSCOPY

4.1 Introduction

The Mueller framework has been recognized as a useful assessment tool for linear imaging of biological samples. As a metrology technique, Mueller matrix polarimetry, or a similar variant, has also been adapted to multiphoton imaging. For example, Mazumder *et al.* [125] presented a technique of illuminating a sample with different polarization states to obtain the Stokes parameters, and subsequently extract both degree of polarization and anisotropy ratio as quantitative metrics. In addition, Ávila *et al.* [126] acquired sets of SHG images of cornea and sclera for independent polarization states, and used the Mueller matrix elements to reconstruct the images for contrasting quality metrics. However, these techniques relate the linear Mueller matrix model to the nonlinear SHG process, and thus an interpretation of the measured results is not clear. Fortunately, Shi *et al.* showed that the standard, one-photon, Mueller calculus used in linear optics can be extended to a general two-photon case through the use of a so-called double Mueller matrix [109]. In this section, we show the experimental demonstration of two-photon Mueller matrix ($MM^{(2)}$)-SHG microscopy by applying the double Mueller matrix polarimetry to SHG imaging. Specifically, we show that measurement of the output Stokes vector permits an estimation of the Mueller matrix for unstained porcine tendon and skin, in principle, down to the level of a single pixel. We also use the Stokes vector to determine the degree of polarization of the nonlinear output.

In order to adapt Mueller matrix polarimetry to multiphoton imaging directly, the linear framework has to be able to accommodate the nonlinear

This work was previously published in C. Okoro and Kimani C. Toussaint Jr. [127], and is adapted here with permission

SHG process. That is, the two-to-one photon conversion process has to be accounted for. The standard Mueller calculus can be extended to the two-photon case by the so-called double Mueller matrix [109]. Indeed, a similar approach can be used for extension to higher order processes in general. This is the mathematical basis for the two-photon Mueller matrix ($MM^{(2)}$)-SHG microscopy, demonstrated in this chapter. This method was applied for two-photon Mueller matrix estimation in unstained porcine tendon and skin, to the level of a single image pixel. The Stokes vector was also used to determine the degree of polarization of the nonlinear output, given a selected input polarization.

4.2 Theory

As described in Eq. 3.11, the Stokes vector used in linear optics describes the polarization state of light in a 4×1 vector form. The "one-photon" Mueller matrix relationship between input (s_β) and output ($\tilde{s}_\alpha$) Stokes vectors elements can be derived from Eq. 3.12 as

$$\tilde{s}_\alpha = \sum_{\beta=0}^{3} m^{(1)}_{\alpha\beta} s_\beta \qquad \alpha = 0, 1, 2, 3 \quad , \tag{4.1}$$

where $m_{\alpha\beta}$ represents the 4×4 Mueller matrix elements and the zero index is used for consistency with Stokes convention. This Mueller calculus approach assumes a linear relation between input and output Stokes vectors. In general, for a multiphoton effect, the Mueller matrix becomes an $(n{+}1)$ dimensional array, where n is the order of the effect. For two-photon effects, Eq. 4.1 becomes

$$\tilde{s}_\alpha = \sum_{\beta=0}^{3} \sum_{\gamma=0}^{3} m^{(2)}_{\alpha\beta\gamma} s_\beta s'_\gamma \qquad \alpha = 0, 1, 2, 3 \quad , \tag{4.2}$$

where $m^{(2)}_{\alpha\beta\gamma}$ are the $4 \times 4 \times 4$ two-photon Mueller array elements relating two sets of input Stokes vector elements (s_β and s'_γ) to yield output Stokes vector elements. We can combine the elements s_β and s'_γ to form new elements of

a 16×1 vector such that

$$\tilde{s}_\alpha = \sum_{\gamma=0}^{15} m_{\alpha B}^{(2)} S_B \qquad \alpha = 0,1,2,3 \quad . \tag{4.3}$$

This makes the matrix with elements $m_{\alpha B}$ a 4×16 matrix representative of two-photon processes such as sum-frequency generation (SFG) and difference-frequency generation (DFG). For the degenerate SHG case, the 16 independent Stokes vector elements can be reduced to 9 independent Stokes vector elements. This reduction of parameters, and the resulting Stokes vector relationship to the single Stokes vector, is shown next.

First, the intensity for a two-photon process in terms of amplitude following from Eq. 2.2 is given by

$$P_l = \sum_{m,n=1,2} \chi_{lmn} E_m E_n \qquad \equiv 4 \text{ terms} \tag{4.4}$$

$$I_l \propto P_l P_l^* \qquad \equiv 16 \text{ terms} \quad . \tag{4.5}$$

If the two photons are identical, it follows that permutation symmetry holds, and $\chi_{lmn} = \chi_{lnm}$.

$$P_l = \chi_{l11} E_1 E_1 + \chi_{lVV} E_2 E_2 + 2\chi_{l12} E_1 E_2 \qquad \equiv 3 \; terms \tag{4.6}$$

$$I_l \propto P_l P_l^* \qquad \equiv 9 \; terms \quad . \tag{4.7}$$

This means that the basis of one photon correlates not only with itself, but also with the basis of the other photon. This translates to Eq. 4.3 becoming

$$\tilde{s}_\alpha = \sum_{\Gamma=0}^{8} M_{\alpha\Gamma}^{(2)} S_\Gamma \qquad \alpha = 0,1,2,3 \quad , \tag{4.8}$$

where S_Γ are the elements of the 9×1 double Stokes vector representation of the input field. The new Jones vector K can then be represented by

$$\boldsymbol{K} = \begin{pmatrix} U_x^2 \\ U_y^2 \\ 2U_x U_y \end{pmatrix} \tag{4.9}$$

Next, we proceed to obtain the double Stokes vector elements for the

second-harmonic process in a similar way as the single photon approach, to give

$$S_\Gamma = \left\langle \overline{\boldsymbol{K}} \boldsymbol{\lambda_\alpha} \boldsymbol{K} \right\rangle = \mathrm{Tr}(\langle \boldsymbol{\rho} \rangle \, \boldsymbol{\lambda_\alpha}) \quad \alpha = 0, 1, 2, 3\,, \tag{4.10}$$

where the new coherency density matrix $\boldsymbol{\rho}$ has the expression

$$\boldsymbol{\rho} = \left\langle \boldsymbol{K} \otimes \overline{\boldsymbol{K}} \right\rangle = \begin{pmatrix} \langle U_x^2 U_x^{*2} \rangle & \left\langle U_x^2 U_y^{*2} \right\rangle & \left\langle 2U_x^2 U_x^* U_y^* \right\rangle \\ \left\langle U_y^2 U_x^{*2} \right\rangle & \left\langle U_y^2 U_y^{*2} \right\rangle & \left\langle 2U_y^2 U_x^* U_y^* \right\rangle \\ \langle 2U_x U_y U_x^{*2} \rangle & \left\langle 2U_x U_y U_y^{*2} \right\rangle & \left\langle 4U_x U_y U_x^* U_y^* \right\rangle \end{pmatrix} \tag{4.11}$$

and $\boldsymbol{\lambda_\alpha}$ are the Gell-Mann matrix Lie generators of the group SU(3) irreducible Hermitian representation.

$$\begin{aligned} \lambda_1 &= \sqrt{\tfrac{2}{3}} \begin{pmatrix} 1 & 0 & 0 \\ 0 & 1 & 0 \\ 0 & 0 & 1 \end{pmatrix}, \quad \lambda_2 = \sqrt{\tfrac{1}{3}} \begin{pmatrix} 1 & 0 & 0 \\ 0 & 1 & 0 \\ 0 & 0 & -2 \end{pmatrix}, \quad \lambda_3 = \begin{pmatrix} 1 & 0 & 0 \\ 0 & -1 & 0 \\ 0 & 0 & 0 \end{pmatrix}, \\ \lambda_4 &= \begin{pmatrix} 0 & 1 & 0 \\ 1 & 0 & 0 \\ 0 & 0 & 0 \end{pmatrix}, \quad \lambda_5 = \begin{pmatrix} 0 & 0 & 0 \\ 0 & 0 & 1 \\ 0 & 1 & 0 \end{pmatrix}, \quad \lambda_6 = \begin{pmatrix} 0 & 0 & 1 \\ 0 & 0 & 0 \\ 1 & 0 & 0 \end{pmatrix}, \\ \lambda_7 &= \begin{pmatrix} 0 & 0 & 0 \\ 0 & 0 & -i \\ 0 & i & 0 \end{pmatrix}, \quad \lambda_8 = \begin{pmatrix} 0 & 0 & -i \\ 0 & 0 & 0 \\ i & 0 & 0 \end{pmatrix}, \quad \lambda_9 = \begin{pmatrix} 0 & -i & 0 \\ i & 0 & 0 \\ 0 & 0 & 0 \end{pmatrix}. \end{aligned} \tag{4.12}$$

By substituting Eqs. 4.11 and 4.12 into 4.10, and expressing in terms of the

single Stokes vector from Eq. 3.19, we get [128]

$$\boldsymbol{S} = \begin{pmatrix} S_0 \\ S_1 \\ S_2 \\ S_3 \\ S_4 \\ S_5 \\ S_6 \\ S_7 \\ S_8 \end{pmatrix} = \begin{pmatrix} \sqrt{\frac{1}{6}}(3s_0^2 - s_1^2) \\ \sqrt{\frac{1}{12}}(5s_1^2 - 3s_0^2) \\ -s_0 s_1 \\ \frac{1}{2}(s_2^2 - s_3^2) \\ s_2(s_1 + s_0) \\ -s_2(s_1 - s_0) \\ -s_2 s_3 \\ s_3(s_1 + s_0) \\ s_3(s_1 - s_0) \end{pmatrix} , \tag{4.13}$$

where we have used the equations $E_H E_H^* = \frac{1}{2}(s_0 - s_1)$, $E_V E_V^* = \frac{1}{2}(s_0 + s_1)$, $E_H E_V^* = \frac{1}{2}(s_2 + is_3)$, $E_V E_H^* = \frac{1}{2}(s_2 - is_3)$. Obtaining the output in conventional 4×1 vector formalism necessitates that the second-order Mueller matrix be expressed in a 4×9 matrix form. This is obtained by generating and solving a system of equations with pre-determined inputs and measured nonlinear output.

A series of nine known input polarization states is generated. The first six are chosen from cardinal points on the Poincaré sphere, while the other three are chosen such that they present a symmetric disposition with respect to the first six on the Poincaré sphere as shown in Fig. 4.1 (a slightly different model from Ref [109]). For each input state, output images for the polarization

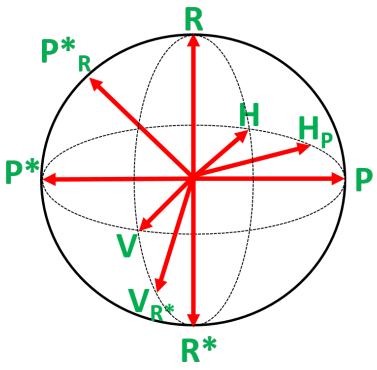

Figure 4.1: Poincaré sphere representation of selected input states.

analyzer settings should be acquired (that is, H, V, P, P^*, R and R^*). Hence, the set of nine equations to solve are

$$\begin{aligned} M^{(2)} \cdot H^{(i)} = H^{(o)}, \quad M^{(2)} \cdot V^{(i)} = V^{(o)}, \quad M^{(2)} \cdot P^{(i)} = P^{(o)}, \\ M^{(2)} \cdot P^{*(i)} = P^{*(o)}, \quad M^{(2)} \cdot R^{(i)} = R^{(o)}, \quad M^{(2)} \cdot R^{*(i)} = R^{*(o)}, \\ M^{(2)} \cdot H_P^{(i)} = H_P^{(o)}, \quad M^{(2)} \cdot V_{R^*}^{(i)} = V_{R^*}^{(o)}, \quad M^{(2)} \cdot P_R^{*(i)} = P_R^{*(o)}, \end{aligned} \tag{4.14}$$

where $M^{(2)}$ is the two-photon Mueller 4×9 matrix, the (i) superscript denotes input 9×1 two-photon Stokes vector and (o) superscript stands for output 4×1 Stokes vector. The individual input and output matrices obtained for each polarization input can be concatenated to obtain consolidated 9×9 input ($U^{(i)}$) and 4×9 output ($U^{(o)}$) matrices, respectively, as

$$\begin{aligned} U^{(i)} &= \begin{pmatrix} H^{(i)} & V^{(i)} & P^{(i)} & P^{*(i)} & R^{(i)} & R^{*(i)} & H_P^{(i)} & V_{R^*}^{(i)} & P_R^{*(i)} \end{pmatrix}, \\ U^{(o)} &= \begin{pmatrix} H^{(o)} & V^{(o)} & P^{(o)} & P^{*(o)} & R^{(o)} & R^{*(o)} & H_P^{(o)} & V_{R^*}^{(o)} & P_R^{*(o)} \end{pmatrix}. \end{aligned} \tag{4.15}$$

By measuring $U^{(o)}$ experimentally, we have access to the degree of polarization per polarization basis of the output SHG Stokes vector (p_m) and the two-photon Mueller matrix ($M^{(2)}$). The former refer to the elements of a 1×9 degree of polarization row vector (p) obtained by invoking

$$p_m = \frac{\sqrt{U_{m1}^{(o)2} + U_{m2}^{(o)2} + U_{m3}^{(o)2}}}{U_{m0}} \tag{4.16}$$

on each column m representing an input polarization state running from 1 to 9. The term p_m can be thought of as the degree of polarization of nonlinear SHG generated by input polarization state m, after passing through the sample. Also, $U_{m0}^{(o)}$ represents element $m0$ in matrix $U^{(o)}$ (and so on for $m1$, $m2$ and $m3$). Since we have pre-determined the input basis, the two-photon Mueller matrix can be determined by solving

$$M^{(2)} = U^{(o)} \cdot [U^{(i)}]^{-1} \quad . \tag{4.17}$$

This approach to obtaining these two metrics can prove useful in understanding how the polarization information may change between different spatial regions within an image.

4.3 Experiment

4.3.1 Samples

Porcine tissue samples were obtained from a local market and embedded in optimal cutting temperature (OCT) compound at -80^{o}C. Next, the samples were brought to -20^{o}C, and cut into thin sections using a cryostat (Leica CM3050S). The tissue slices were then soaked in 1× PBS to remove excess OCT, and mounted onto microscope coverslips using aqueous mounting media. Tendon samples at 5 μm, 25 μm and 75 μm, and skin sample at 5 μm were obtained this way and used in the study.

4.3.2 Experimental Setup

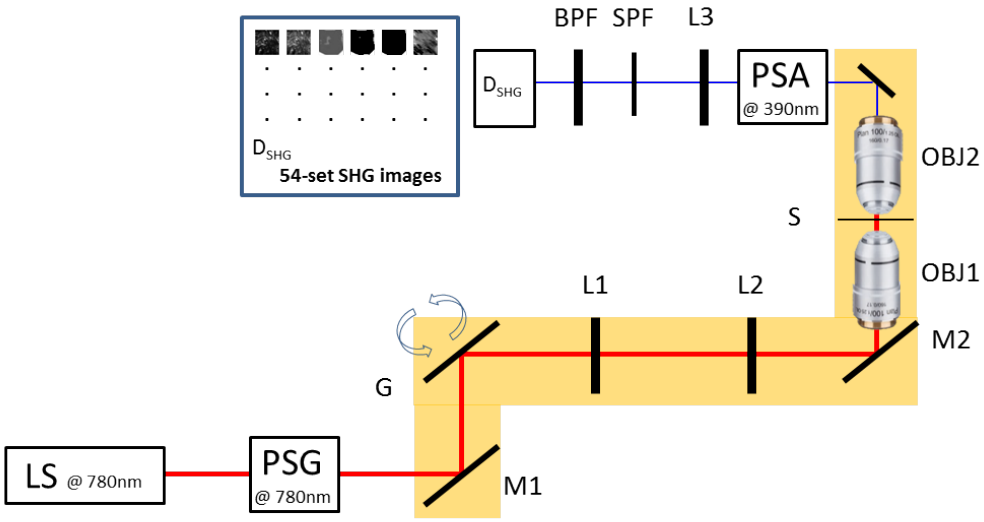

LS:	Laser Source	L:	Lens	SPF:	Short-pass Filter
M:	Mirror	P:	Pinhole	BPF:	Band-pass Filter
BS:	Beam-splitter	D:	Detector	OBJ1:	40×, 0.65 NA
G:	Galvo-scanner	S:	Sample	OBJ2:	50×, 0.8 NA

Figure 4.2: Experimental setup for the image acquisition process.

Figure 4.2 shows the experimental setup used. SHG imaging is performed in the forward direction in order to eliminate the use of dichroics which have inferior polarization preserving properties when compared with metal

mirrors. A Ti:sapphire laser (Spectra-Physics Mai-Tai HP DeepSee) produces 100 fs pulses at an excitation wavelength centered spectrally at 780 nm and a repetition rate of 80 MHz. Galvanometer-based scanning mirrors (Thorlabs GVS012) are used to sweep the beam over a rectangular field of view at the sample plane. Polarization states are generated using a polarization state generator (PSG) system comprising a linear polarizer and wave plate combination (half-wave plate for linearly polarized input, quarter-wave plate for circularly polarized input and both for elliptically polarized input). The beam is then reflected off a metal mirror towards the condenser (0.65NA Olympus 40× PLAN N) which focuses onto the sample. The forward-emitted signal is collected by an infinity-corrected objective (0.8NA Olympus 50× MPlan FL N) and relayed towards a tube lens for focusing. It should be noted that the condenser lens numerical aperture (NA) was chosen to be low enough (<0.7NA [129]) to still ignore transverse polarization changes at focus while maintaining an acceptable resolution (which increases with higher NA). Polarization analysis is performed using a polarization state analyzer (PSA) system having a quarter-wave plate and linear polarizer combination. A laser blocking short-pass filter (Semrock FF01-680/SP-25) is used for illumination rejection, while an SHG band-pass filter (Semrock FF01-390/BP-18-25) is used for narrow band filtering. The detector is an electron multiplying charge-coupled device (Hamamatsu EMCCD C9100-13) camera having a gain of 200× and an exposure time of 1 s.

4.4 Results and discussion

We obtain a set of 54 images, each corresponding to a combination of 6 PSA states for 9 PSG states, and analyze them after binning with 10×10 pixels. This is done so that the analysis can be localized and more spatially sensitive. The choice of binning dimension is made based on sensitivity requirements and computational cost. We subsequently determine the local output Stokes vector, degree of polarization per basis and two-photon Mueller matrix within each of these smaller cells using Eqs. 4.15 and 4.17.

The analysis is applied to 32×32 bins of two porcine sample types (skin and tendon) at 5 μm thickness. Figures 4.3 and 4.4 show SHG images of porcine skin and tendon samples, respectively, with representative average

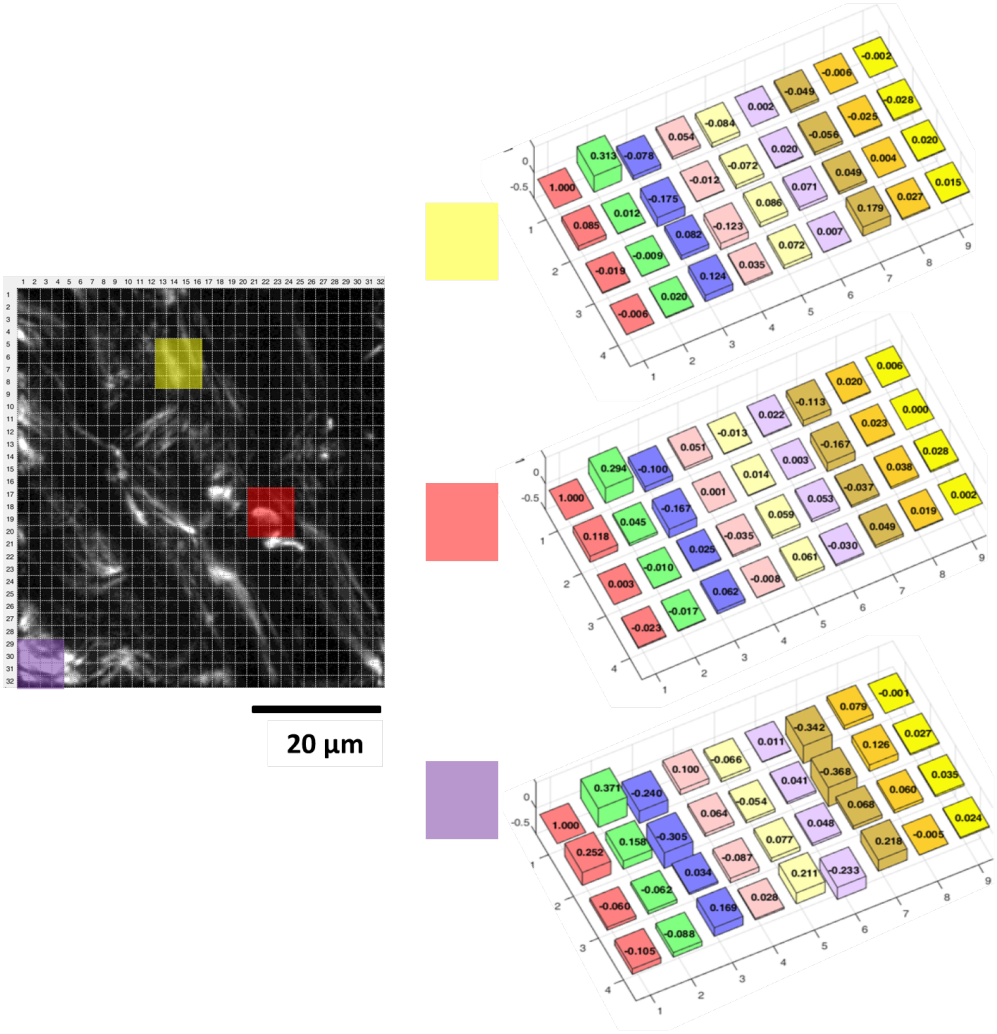

Figure 4.3: Sample SHG image of porcine skin tendon showing the division into 32×32 bins using grids. The average $M^{(2)}$ values are shown for select regions in the image, which are highlighted by the colored boxes. The bars for $M^{(2)}(1:1)$ in the bar plots are truncated for visualization convenience.

$M^{(2)}$ values over selected localized regions highlighted. We observe that for both samples, there is little sensitivity to mode S_8 (represented in terms of single Stokes vector by $s_3(s_1 + s_0)$) since the $M^{(2)}(r : 9)$ terms (where r stands for the index and runs through all the rows) are negligible compared to other elements of the matrix. It is noted that this also holds true to a lesser extent for the $M^{(2)}(r : 8)$ terms.

In order to investigate the effect of thickness, another study was conducted for porcine tendon samples at 5 μm, 25 μm and 75 μm. The values of p_m

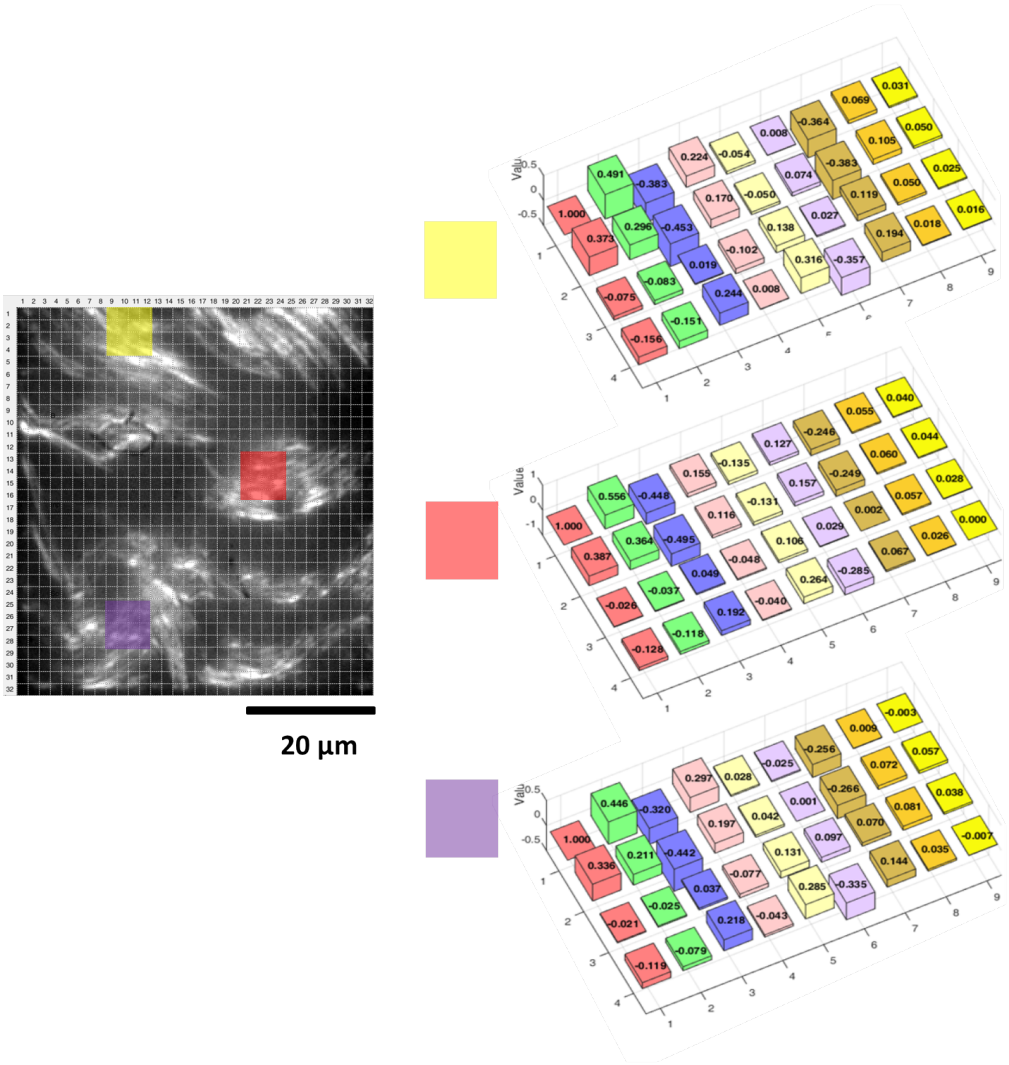

Figure 4.4: Sample SHG image of porcine tendon showing the division into 32×32 bins using grids. The average $M^{(2)}$ values are shown for select regions in the image, which are highlighted by the colored boxes. The bars for $M^{(2)}(1:1)$ in the bar plots are truncated for visualization convenience.

across the various sub-images are obtained, and the results represented as a histogram distribution plot. For a quantitative description, we choose to fit our data to a bimodal model f with normal distribution curves as given by

$$f = q\frac{1}{\sigma_1\sqrt{2\pi}}e^{-\frac{(p-\mu_1)^2}{2\sigma_1^2}} + (1-q)\frac{1}{\sigma_2\sqrt{2\pi}}e^{-\frac{(p-\mu_2)^2}{2\sigma_2^2}} \quad , \tag{4.18}$$

where $[\mu_1, \mu_2]$ represent the bimodal mean values, $[\sigma_1, \sigma_2]$ stand for the bimodal standard deviation values and $[q, 1-q]$ are mixture probability weights

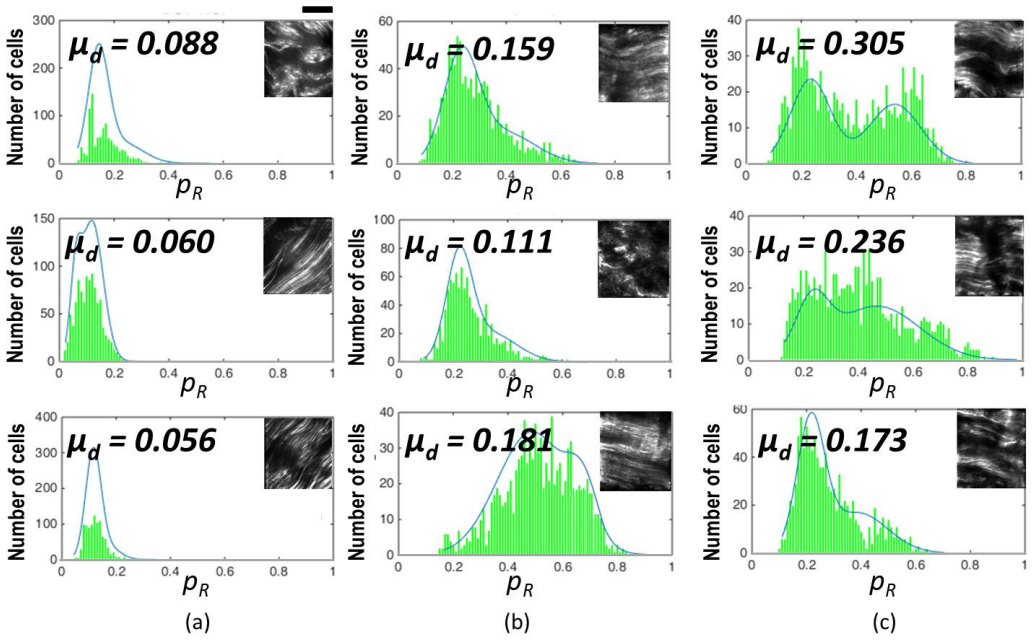

Figure 4.5: Histogram plots of p with R-input for porcine tendon at (a) 5 μm, (b) 25μm and (c) 75 μm, each taken at three different spatial regions. The solid lines are best fits using the bimodal distribution equation. The associated bimodal mean difference (μ_d) is also provided. Inset for each plot shows SHG images of the different spatial regions. The scale bar above the top left image is 40 μm.

attached to the modes of the distribution. A new metric, the bimodal mean difference μ_d (defined by $|\mu_1 - \mu_2|$), which can be considered a measure of shape distribution, is then retrieved.

For the set of experiments involving the nine input states, input polarization state R (or R-input) shows the greatest variation in μ_d. The R-input results for 32×32 sub-image cells across three different spatial regions each for 75 μm, 25 μm and 5 μm thick porcine tendon samples are shown in Fig. 4.5. Using the bimodal distribution equation, a best fit curve for the histogram is obtained and μ_d extracted. We find here a variation in μ_d (average of 0.068 for 5 μm and 0.150 for 25 μm and 0.238 for 75 μm), which depends on the thickness. This can be thought of as implying that the thicker the sample, the greater the range of p values and the larger the μ_d values that are obtained from the generated SHG. Qualitatively, this suggests that thicker samples mean more scattering events, and hence greater variation in derived parameters. However, it is important not to read too much meaning into

these results due to the limited sample size. Rather, the significance of the measurements is that they are robust and permit the inclusion of polarimetry with SHG imaging.

In conclusion, $MM^{(2)}$-SHG microscopy was used to extract nonlinear Mueller matrices for quantitative assessment of SHG images. Specifically, the output Stokes vectors were experimentally measured and used to determine the two-photon Mueller matrix and degree of polarization. Moreover, another metric, the bimodal mean difference (μ_d), was derived from the degree of polarization distribution model and it was observed that this metric showed increasing variation with thickness of porcine tendon samples. The increased variation is consistent with the intuition of increased scattering for thicker samples. This can possibly be used in investigating localized growth and/or changes in organizational structure as an indication of abnormality in tissues. However, care should be taken in interpreting p_m because the nonlinearity of SHG complicates relating it to the depolarization of the input Stokes vector. Moving forward, other exploratory themes include computational mining of information-rich two-photon Mueller matrix to obtain additional metrics that would be consistent with a second-order nonlinear scattering process. Furthermore, a multimodal approach can be developed by taking the fiber orientation into consideration, using for example FT-SHG [130]. This approach has the potential to be adapted to other multiphoton coherent imaging techniques.

CHAPTER 5

SECOND-HARMONIC PATTERNED POLARIZATION ANALYZED REFLECTION CONFOCAL MICROSCOPY

5.1 Introduction

A limitation of Mueller matrix SHG microscopy, with its second-order Mueller matrix theory, is that the parameters obtained are not as intuitive as the conventional polarimetry case, and this is important for understanding the underlying tissue properties. The question to be asked then is: Can we utilize linear polarimetry with its rich obtainable parameters, while retaining the strengths of SHG microscopy specificity to collagen? Fortunately, the answer it yes.

In this section, we introduce the second-harmonic patterned polarization-analyzed reflection confocal (SPPARC) microscope, which provides both SHG and linear polarimetric confocal microscopy images at a target imaging plane in a volume. We also demonstrate the capabilities of SPPARC microscopy in obtaining spatially dependent polarization information in three dimensions, from both collagen fibers in tissue and the surrounding EFMC. SPPARC combines the advantage of collagen-specificity from SHG microscopy with the potential insight acquired from linear polarimetry using reflection confocal microscopy. Moreover, the optical sectioning capability of both techniques is retained. The SHG images are used as an endogenous mask to pattern the confocal images, and the resulting collagen-filtered confocal images undergo MMPD analysis for extraction of traditional, linear polarimetric measures, namely, depolarization, retardance and diattenuation matrices, along with their associated scalars. In addition, the non-collagenous regions comprising the EFMC can also be obtained from the SPPARC images, and analyzed.

This work was previously published in C. Okoro and Kimani C. Toussaint Jr. [121], and is adapted here with permission

This technique provides a single microscopy platform that can provide label-free, quantitative information of both the collagen fibers comprising the ECM and the EFMC environment around the fibers. In the following sections, we briefly review reflection confocal microscopy, describe some polarization parameters, demonstrate the technique and show some results.

5.2 Confocal microscopy

Confocal microscopy is a linear optical imaging modality that uses a spatial pinhole to reject out-of-focus light, hence enabling three-dimensional sectioning of images. While quite popular for fluorescence imaging, it also finds applications in imaging unlabeled samples.

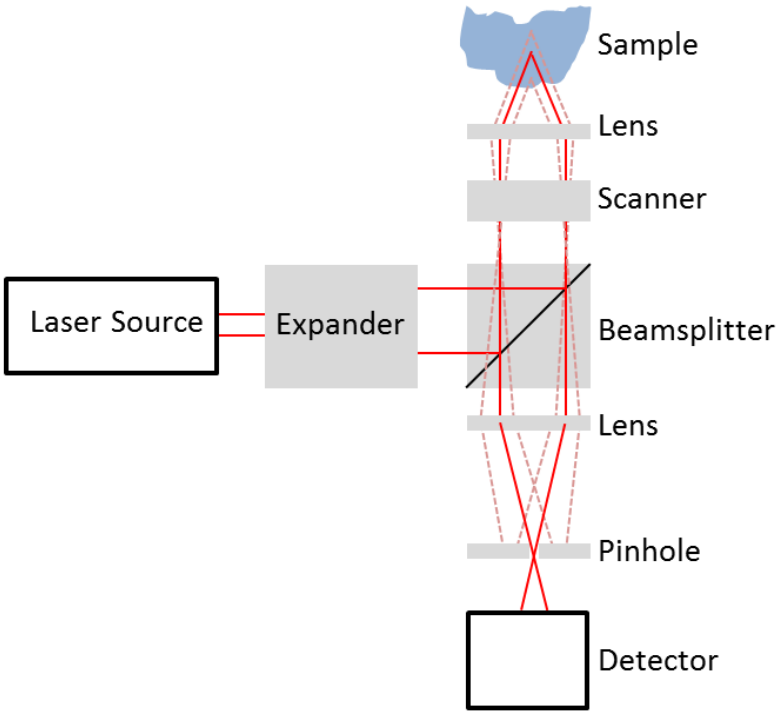

Figure 5.1: Simple confocal microscopy setup.

Figure 5.1 shows a simple reflection confocal microscopy setup for imaging tissues. A low coherence length laser source is ideal since this reduces the speckle that can result from interference [131]. For unlabeled samples, a

beamsplitter is used (instead of a dichroic) because the scattered light at the fundamental is the signal being detected. Two scanning mechanisms can be implemented: either the beam is scanned using an x-y scanner, or the sample can be scanned using a stage scanner. The much faster x-y beam scanning system is implemented with the scanner after the beamsplitter, so that the signal can be de-scanned before being directed towards the pinhole. The alternative to de-scanning would be to use a pinhole that tracked the beam path, a much harder problem.

The pinhole size determines the resolution, as well as the signal-to-noise ratio (SNR) of the acquired image. The smaller the pinhole, the better the resolution, since more of the out-of-focus rays are blocked. This is illustrated in the confocal setup picture, where most of the out-of-focus rays (in dashed lines) from above and below the in-focus plane are blocked out. However, there will be no marked increase in resolution if the pinhole becomes smaller than 1 airy-unit (size of a diffraction-limited spot scaled by the magnification at the pinhole plane). The theoretical lateral resolution achievable is $\frac{0.37\lambda}{NA}$ [96] while the axial resolution has been given as $\frac{0.64\lambda}{n-\sqrt{n^2-NA^2}}$ [96] and $\frac{1.4n\lambda}{NA^2}$ [132], where n is the refractive index of the medium, NA is the numerical aperture of the objective lens and λ is the excitation wavelength.

5.3 Experiment

5.3.1 Samples

Porcine tendon and posterior cruciate ligament (PCL) were embedded in optimal cutting temperature compound at -25^{o}C. The samples were then cut into thin sections using a cryostat (Leica CM3050S) and soaked in 1$\times$ PBS to remove the excess embedding compound. Next, the sections were placed on glass microscope slides, and # 1.5 coverslips were mounted on top with the aqueous mounting media. Tweezers were used to gently lower the coverslip on the microscope slide to avoid creating any air bubbles. After the samples were dried, nail polish was applied on the corners to seal the samples. Note that this study is exempt from the Illinois Institutional Animal Care and Use Committee (IACUC).

5.3.2 Experimental setup

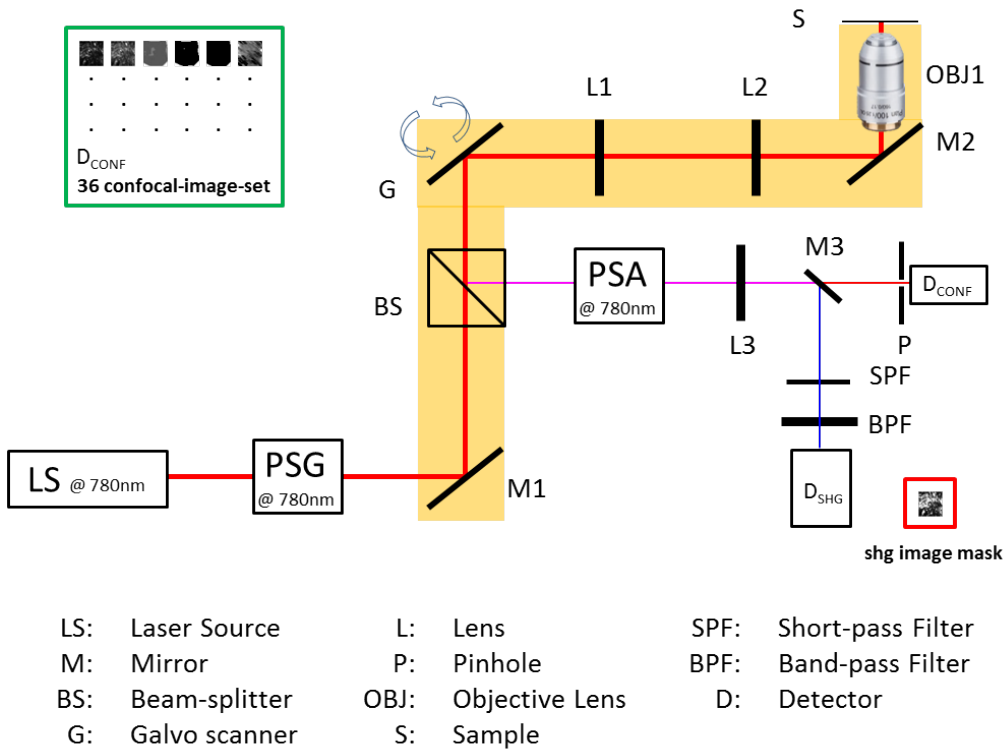

Figure 5.2: Experimental setup. The yellow region represents part of the setup that requires critical pre-calibration. The bold red line shows the path of the illuminating beam. The thin magenta line represents the common path taken by the emitted signals on reflection by the beamsplitter, while the thin red and blue lines show the paths taken by the confocal and SHG signals, respectively.

Figure 5.2 illustrates the SPPARC optical setup. A Ti:sapphire laser system (Spectra-Physics Mai-Tai) produces 100 fs duration pulses spectrally centered at 780 nm. The polarization state of the input beam is set using a polarization state generator (PSG) [127]. This beam is directed through a cube beam-splitter (30:70) and subsequently relayed by mirrors and lenses. A strain-free objective (Olympus ACHN40XP 0.65NA 40×) focuses the beam onto the sample. This relatively lower numerical aperture and strain-free objective is used to allow the focusing behavior to be satisfied within scalar diffraction theory [133], and to minimize unwanted polarization scattering effects. Scanning galvo mirrors sweep the beam across a ∼200 μm field-of-view

on the sample. The epi-scattered signal is collected by the same objective, and guided back through the initial path up till the beam-splitter which partially reflects it towards a polarization state analyzer (PSA) [127] to measure the polarization state of the signal. The beam is focused through a 50 μm diameter pinhole at the conjugate plane and then measured by a photomultiplier tube (PMT) detector D_{CONF} to obtain polarimetric confocal images via different PSG-PSA configurations. SHG images at 390 nm are obtained using right circularly polarized light and no PSA, by inserting mirror M3 into the beam path. This deflects the beam towards a short-pass (Semrock FF01-680/SP-25) and band-pass (Semrock FF01-390/BP-18-25) filter combination so as to allow only the second-harmonic signal through, which is then detected by the PMT (D_{SHG}).

5.3.3 Setup calibration and Mueller matrix characterization

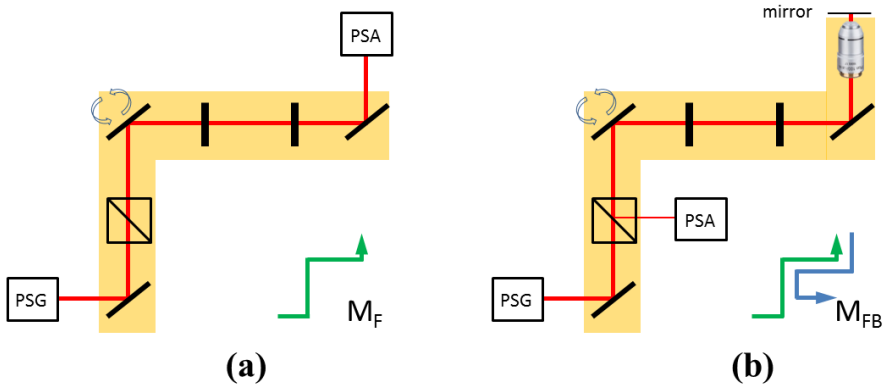

Figure 5.3: Mueller matrix characterization of the optical system. (a) The forward matrix, M_F. (b) The forward + backward matrix, M_{FB}, using a mirror M in place of the sample. The arrows to the right bottom corner indicate the path traveled by the beam from generation to analysis.

Polarimetric images obtained using the setup include polarization contributions from the optical setup. In order to isolate the sample's Mueller matrix contribution, a full characterization of the optical setup's Mueller matrix is done. First, the forward matrix M_F is obtained by PSA-PSG measurements using the arrangement in Fig. 5.3(a) to be $\boldsymbol{M_F} = \begin{pmatrix} 1.000 & 0.000 & 0.000 & 0.000 \\ 0.063 & -0.704 & -0.391 & 0.592 \\ -0.083 & -0.675 & 0.644 & -0.396 \\ -0.012 & -0.052 & -0.652 & -0.624 \end{pmatrix}$.

In a similar manner, the forward+backward matrix M_{FB} was obtained from the arrangement in Fig. 5.3(b) to be $\boldsymbol{M_{FB}} = \begin{pmatrix} 1.000 & 0.000 & 0.000 & 0.000 \\ -0.001 & -0.951 & -0.224 & -0.202 \\ 0.039 & 0.144 & 0.179 & -1.000 \\ 0.006 & 0.422 & -0.900 & -0.151 \end{pmatrix}$. Since we have

$$\boldsymbol{M_{FB}} = \boldsymbol{M_B M_{mirror} M_F} \quad , \tag{5.1}$$

the backward matrix M_B can then be obtained from

$$\boldsymbol{M_B} = \boldsymbol{M_{FB}} (\boldsymbol{M_F})_P^{-1} (\boldsymbol{M_{mirror}})_P^{-1} \quad , \tag{5.2}$$

where $M_{mirror} = \begin{pmatrix} 1 & 0 & 0 & 0 \\ 0 & 1 & 0 & 0 \\ 0 & 0 & -1 & 0 \\ 0 & 0 & 0 & -1 \end{pmatrix}$ is the ideal mirror Mueller matrix reflecting at normal incidence [134]. Using M_F and M_B, the sample matrix M_{sample} can be obtained from the measured matrix $M_{measured}$ via

$$\boldsymbol{M_{sample}} = (\boldsymbol{M_B})_P^{-1} \boldsymbol{M_{measured}} (\boldsymbol{M_F})_P^{-1} \quad . \tag{5.3}$$

5.4 Results

For a selected region, 36 polarimetric confocal sample images, from six PSA configurations for each of six PSG states, and a corresponding SHG image are obtained. Each image spans 512×512 pixels and is collected in ∼120 seconds. The SHG image is binarized by setting a threshold, based on second-harmonic signal strength, to highlight regions with appreciable collagen. This thresholded SHG image is then used as a mask to pattern the polarimetric confocal images. This process has the effect of yielding confocal images of collagen-rich regions. We subsequently determine the Mueller matrix per pixel using an image analysis algorithm based on Eq. 3.54, and extract sub-matrices and scalar parameters using equations in Table B.1. Figure 5.4 shows the confocal (red), SHG (green) and resulting SHG-patterned confocal (grayscale) images for three layers of a 3D z-stack of porcine tendon, with a step size of 5 μm. From theoretical considerations [135], the axial resolutions are calculated to be $1.4 \cdot n \cdot \lambda_{em1}/\mathrm{NA}^2$ (= 2.6 μm) for confocal microscopy, and $2.3 \cdot n \cdot \lambda_{em2}/\mathrm{NA}^2$ (= 2.1 μm) for SHG microscopy. The emission wavelengths, λ_{em1} and λ_{em2}, are given to be 780 nm and 390 nm respectively, and n is assumed to be that of air. These values are sufficiently close to show that the

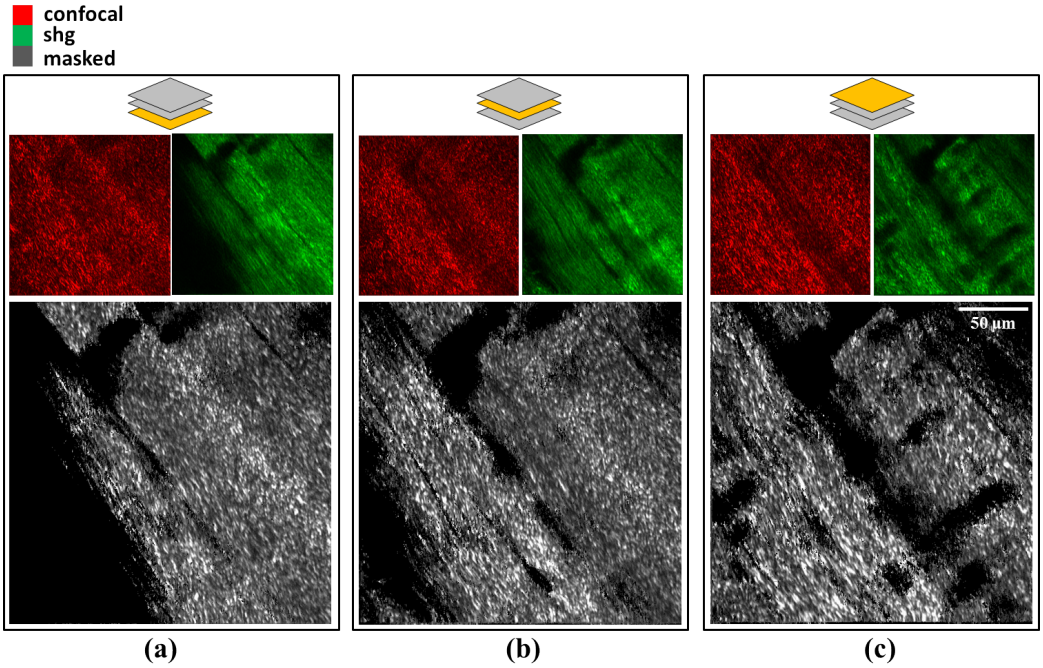

Figure 5.4: Confocal (red), SHG (green) and resulting masked (gray) images for three layers (a-c) of a porcine tendon z-stack with a step size of 5 μm. The currently imaged region in a stack is colored in yellow in the schematic above each column. The 50 μm scale bar applies to only the masked images.

images are roughly representative of similar planes. Each slice should also exclude significant out-of-plane signal contamination, since the resolution is less than the 5 μm layer separation.

The variation of parameters across the three layers imaged is shown in Fig. 5.5. From Fig. 5.5(a), depolarization and circular DOP parameters show a similar trend, reducing in value with deeper tissue penetration. Diattenuation and linear DOP show minimal variation across layers. The high linear DOP values indicate that there is a cumulative effect of preserving linear polarization, which is expected to be along the direction of the fibrils. In Fig. 5.5(b), it is observed that the average linear retardance reduces with deeper penetration.

Figure 5.6 shows polarization "heat" map comparisons between selected parameters from collagen in PCL and the center z-slice of porcine tendon imaged. On average, PCL has higher circular DOP values (0.75) than tendon

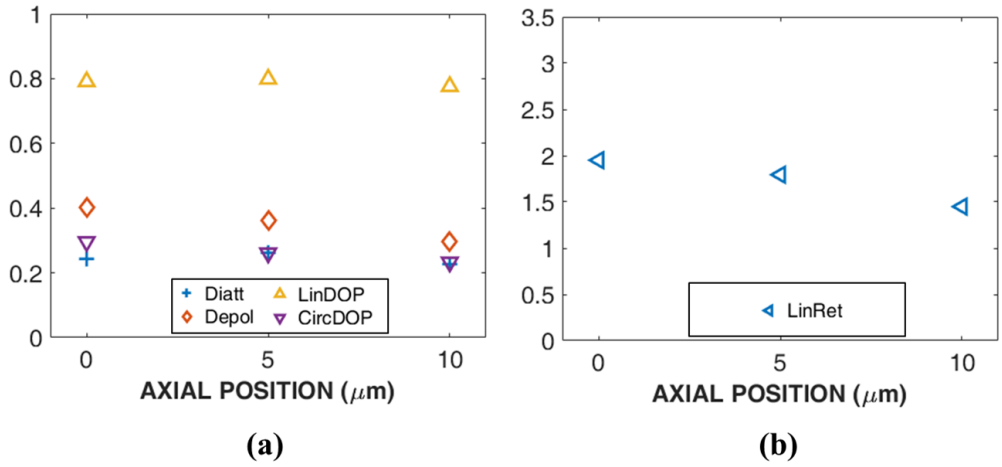

Figure 5.5: Variation of mean polarization parameters for collagen across three porcine tendon layers. (a) Diattenuation, depolarization, linear DOP and circular DOP, over a 0-to-1 range. (b) Linear retardance over a 0-to-π range. The legend shows the color assignment for each parameter.

(0.25). This implies that circularly polarized light preserves its polarization to a higher degree on passing through PCL. This observation is supported by the depolarization map, since the reduction of circular DOP most likely contributes to the overall depolarization of the sample. Ligament and tendon are connective tissues that have parallel and tightly packed heterogeneous collagen fibers [136]. However, ligament may also include collagen bundles with spiral arrangement [137], and this additional organization variation potentially explains the preferential response to circularly polarized light. Furthermore, the linear retardance of tendon collagen is less than that of PCL collagen. Since linear retardance is related to the birefringence of the sample, this seems to imply that the PCL region imaged has higher birefringence than tendon, which is another expected effect of a spiral/helical fiber arrangement [138].

Figure 5.7 shows the "heat" map comparisons for some parameters from a collagen-rich region and non-collagenous EFMC in PCL. The differences in mean values are more subtle in this case. Also, the polarization data does not show as much variation as the confocal images, and this may be due to additional isotropic absorption which varies across the region imaged, and affects intensity but not polarization information. It is observed that, on average, the linear DOP is preserved more for PCL collagen than PCL EFMC.

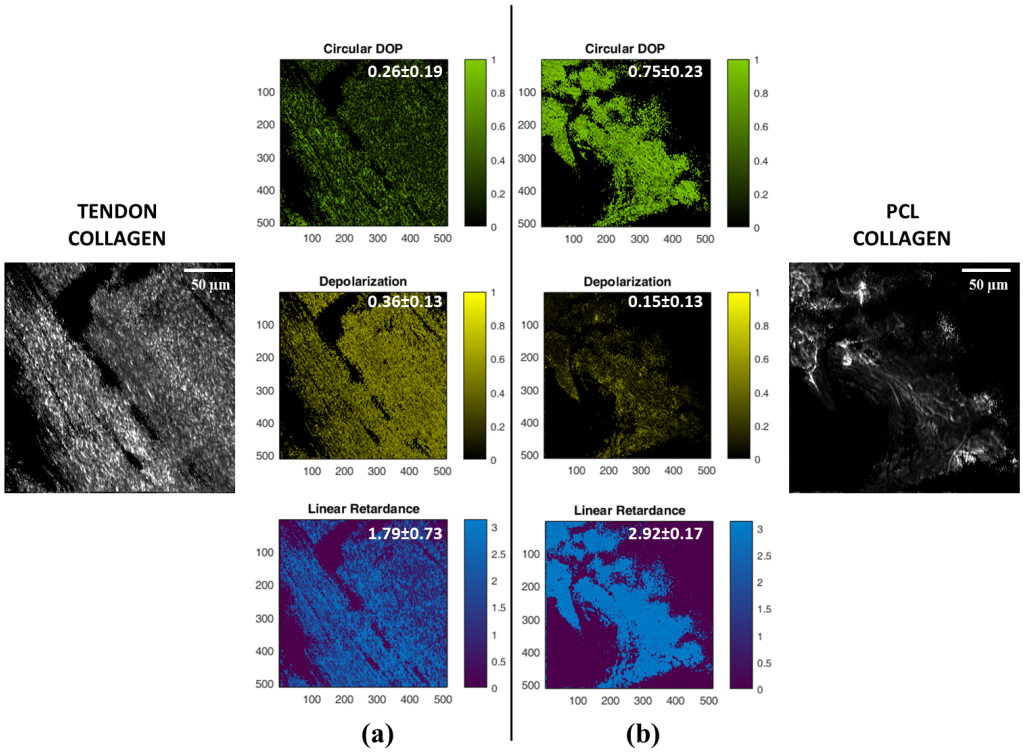

Figure 5.6: Comparison between selected polarization parameter maps (circular DOP, depolarization and circular retardance) of collagen in porcine (a) tendon and (b) PCL. The color bars represent the range of allowed values for each polarization metric. The inset values at the top right hand of the images are the average parameter values per pixel that contributes to signal, along with the standard deviation.

This suggests that there are more components that scatter linear polarization in the EFMC than in fibers. Furthermore, the higher average linear retardance points to the relatively higher birefringence of collagen compared with EFMC. A previous study that alludes to this observation showed that increased presence of other EFMC components such as proteoglycan caused lower linear birefringence [139], inferring that the EFMC has an average lower linear retardance than collagen. However, care must be taken in comparing these values, as the overlapping error bars suggest that the observed differences are not statistically significant.

In summary, the multimodal SPPARC microscope was introduced, from which three-dimensional SHG-patterned confocal microscopy images of colla-

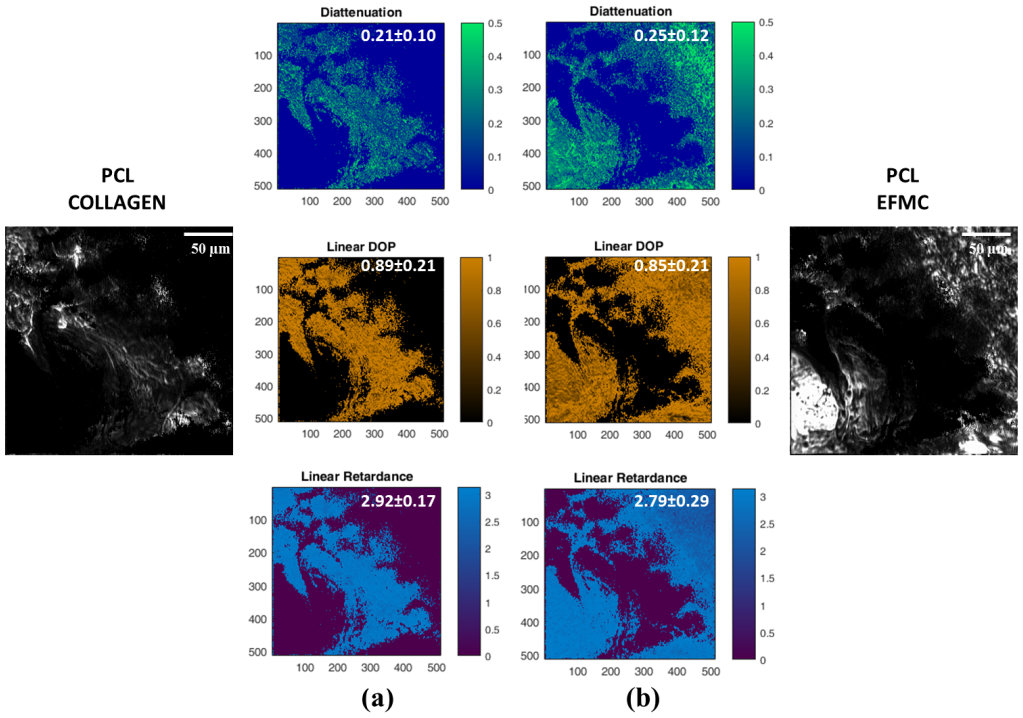

Figure 5.7: Comparison between selected polarization parameter maps (diatenuation, linear DOP and linear retardance) for (a) collagen and (b) EFMC, in porcine PCL. The color bars represent the range of allowed values for each polarization metric, apart from diattenuation, whose range has a maximum at 0.5 to increase contrast. The inset values at the top right hand of the images are the average parameter values per pixel that contributes to signal, along with the standard deviation.

gen fibers were obtained. We applied linear polarimetric analysis and matrix decomposition methods to these images in order to obtain rich polarization information. We also showed that SPPARC microscopy permits label-free quantitative analysis of the EFMC, which to our knowledge had heretofore not been accomplished. Using MMPD as a decomposition approach, we highlighted differences in average parameter values between tendon and PCL collagen, and observed that PCL preserves circular DOP (and hence has less total depolarization) better than tendon collagen. The variation in parameters was not as pronounced for the comparison between tendon collagen and tendon EFMC. We also tracked changes in parameters across layers for collagen in tendon. The retardance parameters, in particular, showed grad-

ually decreasing values for deeper penetration. In order to make statistically significant comparisons with stronger interpretation of results, an in-depth study involving more samples and further data analysis would be needed. In addition, the potential of polarimetric measures for differentiation would be more readily realized for complex microstructures having greater diversity, such as is the case with varying pathologies of cancerous tissues. This is indeed the focus of ongoing work being undertaken. Furthermore, other decomposition methods, such as the differential matrix decomposition [124], can be adapted to SPPARC microscopy.

CHAPTER 6

ANALYSIS OF STROMAL COLLAGEN IN BREAST BIOPSIES

6.1 Motivation

Breast cancer is the most predominant cancer in women and accounts for 30% of all new female cancer cases [140]. Added to the fact that it is the second leading cause of estimated cancer-related female deaths, the importance of early diagnosis and prognosis, which leads to better survivability [141], can be appreciated. The gold standard for cancer diagnosis on breast tissues is the qualitative assessment of hematoxylin and eosin (H&E) stained tissues performed by trained pathologists. Predicting future outcome for patients has relied on conventional prognostic factors such as tumor size, nuclear grade and axillary lymph node status [142]. Studies show that there are other prognostic markers, such as gene-expression signatures, that can more accurately predict or at the very least, complement current existing criteria [143].

Prognostic markers increasingly being recognized as important for describing growth and migration of tumors include the family of extracellular matrix (ECM) features [144–146]. In particular, the role of collagen in regulating tumor progression has been previously highlighted. For example, Provenzano *et al.* assigned distinctive signatures of collagen arrangement proximal to tumors as a means of classification [147]. Subsequent studies showed that such signatures predict poor outcome in patients, possibly due to provision of migration tracks that facilitate invasion [148, 149]. Obtaining orientation signatures, however, involves imaging on scales that reveal structural organization, and requires image processing in order to reveal quantitative information. Collagen density and stiffness also play a critical role in driving tumor invasion through processes such as increased facilitation of stromal collagen re-organization [150], modulation of hormone-crosstalk [151] and activation

of mechanically-sensitive signaling pathways [152]. Thus, this apparent significance of collagen and the broader ECM in cancer studies necessitates approaches for quantitative assessment of this specific environment.

Polarimetry is a powerful tool for collagen assessment, since it is sensitive to information about intrinsic structural properties on molecular and fibrillar scales [153, 154], hence presenting an evaluative framework for collagen samples. Polarization investigation has previously been implemented for assessment of both stained [59, 60, 155] and unstained [156–158] samples, analyzing features such as structural organization, orientation, alignment and birefringence. One approach by Ambekar *et al.* [159] calculated second-order polarization susceptibility ($\chi^{(2)}$) matrix elements of collagen using second-harmonic generated intensities. This approach requires the use of a crystallographic model for fitting acquired signals and subsequent estimation of parameters. An alternative polarization framework is Mueller matrix polarimetry which presents a comprehensive descriptive methodology since it incorporates the effect of depolarization. Along with other derivable metrics such as diattenuation and retardance, samples can be objectively assessed for evaluation. When combined with imaging [134], spatially varying polarization information can be extracted for better insight into sample properties [160–162]. As an example, Pierangelo *et al.* [163] observed that cancerous colon tissues with high cellular density and vascularization depolarized less than non-cancerous tissues, though this was complicated by other factors such as thickness and penetration level in deeper layers. He *et al.* [164] plotted frequency distributions of Mueller matrix images of cervical tissues, and found larger anisotropy and depolarization in benign tissues compared to abnormal. Following a similar trend, Tata *et al.* also observed lower depolarization in breast cancer tumors grown in mice compared with normal regions [165], while Dong *et al.* [166] observed increased linear retardance for *ductal carcinoma in situ* compared with normal tissues.

In the studies highlighted, constituent components in each sample (such as cells, vascularized regions, nuclei, collagen, mucin and lipids) all contribute to the polarization response, and not much is done in separating out individual component polarimetric contributions. As has been motivated earlier, collagen is important for cancer cell development. Hence, it would be beneficial to isolate the polarimetric contributions of collagen, in order to gain an improved understanding of its role during the breast tumor-microenvironment

interplay. Second-harmonic generation (SHG) microscopy is a suitable technique for imaging collagenous tissues, but its nonlinearity complicates polarization parameter extraction and interpretation [109, 127, 128]. We have recently developed second-harmonic patterned polarization-analyzed reflection confocal microscopy (SPPARC) microscopy as such a method to obtain the desired discriminatory polarization information in a manner that facilitates intuitive meaning of the measured polarization properties [121]. In this section, we show results on performing SPPARC imaging on varying pathologies of breast tissues, specifically *benign* (BT), *benign adjacent* (BAT) and *invasive lobular carcinoma* (ILC), in order to tease out differentiating metrics in the relevant collagen ultrastructure and extrafibrillar matrix *plus* cells (EFMC) region. The EFMC, also introduced in the previous section [121], is the part of the image captured by confocal microscopy but not by SHG microscopy, which implies that this section of tissue is the region with negligible or no collagen. We highlight parameters that exhibit greatest sensitivity to the different pathologies and present results of variation in these parameters, making comments about possible causes for these differences. To our knowledge, this is the first time that differences between linear Mueller matrix polarization response of collagen in *benign* and *malignant* breast tissues have been explored.

6.2 Experiment

6.2.1 Samples

The human breast TMA used in this study (labeled T088b) was purchased from US Biomax, Inc. The TMA specification obtained from the manufacturer includes age, grade, type and pathology diagnosis. Consecutive 25 μm sections of each tissue core were cut, and one set stained with hematoxylin and eosin in order to obtain corresponding brightfield images to the SHG images of the unstained second set. This is done so as to easily highlight regions of interest in the H&E stained images that will be assessed with SPPARC on unstained sample. The experiments on the TMA public use data are exempt from review by the University of Illinois Institutional Review Board. All experiments were carried out in accordance with relevant guidelines and

regulations.

6.2.2 Experimental setup

Brightfield images of the cores are acquired using a Zeiss observer Z1 inverted microscope, as described in the Methods section of Ref [167]. Light from a halogen lamp source illuminates the sample, and the scattered light, collected by a 10× Plan-Neofluar objective, is imaged to an Axiocam 503 color CCD camera. SHG imaging of the core samples is performed with a Zeiss NLO 710 microscope attached to an 80 MHz laser source as described previously [100, 168]. The SPPARC microscopy setup for collagen Mueller matrix polarimetry has also previously been described in detail [121]. Briefly, laser light at a wavelength of 780 nm from a 100 fs pulsed, 80 MHz repetition rate source is scanned using galvo mirrors and guided towards a strain-free 40× 0.65NA objective lens which focuses the light onto the sample plane. Epi-directed SHG signals at 390 nm and linearly scattered reflection confocal signals at 790 nm are collected by the same objective, partly reflected by a beam splitter and relayed to a photomultiplier tube (PMT) detector. A 50 μm confocal pinhole-PMT arrangement is used to collect the linearly scattered signals, while the SHG signals are collected by a combination of SHG filter (18 nm bandwidth centered at 390 nm) and PMT. A polarization state generator (PSG) and polarization state analyzer (PSA), each comprising reverse arrangements of linear polarizer, half-wave plate and quarter-wave plate, set up the different optical polarimetric configurations for generation and analysis of polarization states. For a given region, a complete set of oversampled polarization information (thirty-six 256×256-pixel images) is acquired in ∼1 hour. Each acquired image has a pixel size of ∼400 nm.

6.3 Results

6.3.1 Analysis

Each polarimetric confocal image is segmented using the SHG image as a mask. In this way the collagen-rich regions above an SHG signal threshold, and the non-collagenous regions (referred to as extracellular matrix *plus*

cells, EFMC) below this threshold can be decoupled. Spatial polarization information using matrix analysis and MMPD across an image is obtained per 2×2 binned pixels, in order to mitigate the effect of pixel saturation that may occur randomly during signal acquisition and for faster analysis.

6.3.2 Results and discussion

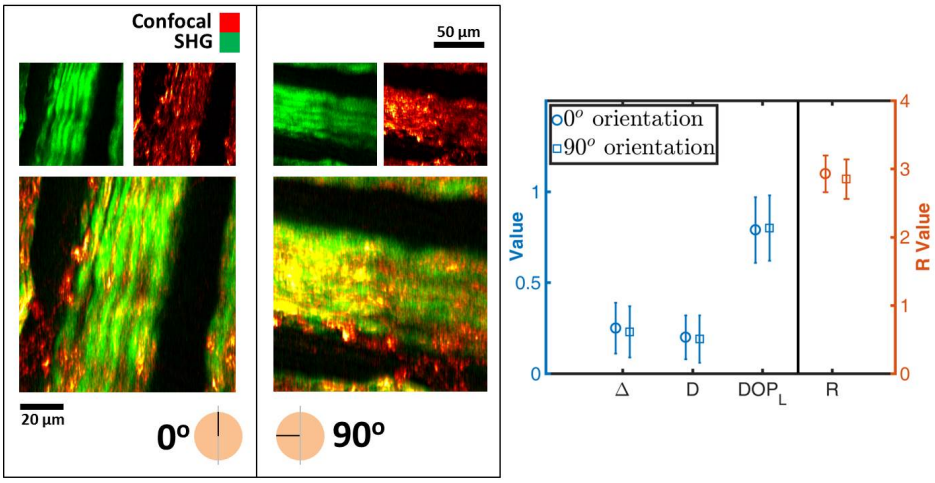

Figure 6.1: Composite images, with corresponding source SHG (pseudo-colored green) and confocal (pseudo-colored red) images, of orthogonal sample orientations of porcine tendon, used to generate scalar polarimetric parameters. The similarity in error plots between the parameters extracted from both orientations shown on the right, demonstrates the consistent nature of the extracted parameters.

As a first experiment to vet the consistent and intrinsic nature of the scalar polarimetric values extracted by matrix analysis and MMPD, SPPARC microscopy was performed on the same region of porcine tendon placed on the microscope slide holder at orthogonal orientations. It is expected that the intrinsic polarization response parameters would be invariant to rotation, even though the measured Mueller matrices would be different (in fact, the measured matrices should have an orthogonal relationship to each other). Porcine tendon presents a viable sample for verification studies because it is rich in fibrillar collagen [169, 170], thus providing a source of strong optical signals at the fundamental and second harmonic. Figure 6.1 shows the SHG-confocal image set for a randomly selected region that forms the composite image used to validate the invariance of the polarimetric parameters to ro-

tation. The plot on the right in Figure 6.1 shows the mean and standard deviation values of four polarimetric parameters (depolarization Δ, linear degree-of-polarization DOP_L, retardance R and diattenuation D). There is close agreement for all the mean values with changes of 8%, 1%, 3% and 5% for Δ, DOP_L, R and D respectively. The similarity in standard deviation values demonstrates consistency in parameter variation across the field-of-view considered.

We next proceed to perform imaging and analysis on breast tissues. A breast tissue micro-array (TMA,) with regions designated above as BT and BAT as control, along with ILC is assessed using SPPARC microscopy. Each tissue core has a diameter of $\sim$1.5 mm and is $\sim$25 μm thick. More details about the breast TMA are given in the Methods section. Figure 6.2 shows SHG images and the corresponding brightfield images of consecutively cut H&E stained cores for BT, BAT and ILC selected from the TMA. The age classification for the cores is also shown, with ILC and BAT obtained from women older than 45 years, while BT samples were obtained from women younger than 30 years. Stromal regions of interest on the tissue cores considered are marked in red on the H&E brightfield images, and used as a reference to perform SPPARC imaging on relevant sections (highlighted with yellow boxes on the SHG images). We compare the perilobular stroma of BT and the available stroma adjacent to BAT and surrounding/within ILC. We also avoid regions which display observable shrinkage and other artifacts due to tissue processing.

Figure 6.3 shows a pair of SPPARC microscopy images of one selected region each for BAT and ILC, along with their resulting maps for two extracted parameters: depolarization and linear degree-of-polarization. In these representative examples, it is observed that the depolarization effect of the stroma within malignant tissue is less than that of the BAT. Thus, the collagen contribution in malignant tissues shows a similar trend of the lower mean depolarization reported in previous studies of tumors [163–166]. In contrast, the effective linear degree-of-polarization of the output light after interaction with the samples shows the opposite trend.

For increased statistical strength, SPPARC microscopy is performed on 47 regions comprising 23 ILC and 24 benign regions (11 BT and 13 BAT sections). We find that the greatest parameter differences from collagen in ILC come from those in BAT sections. This suggests that the collagen optical

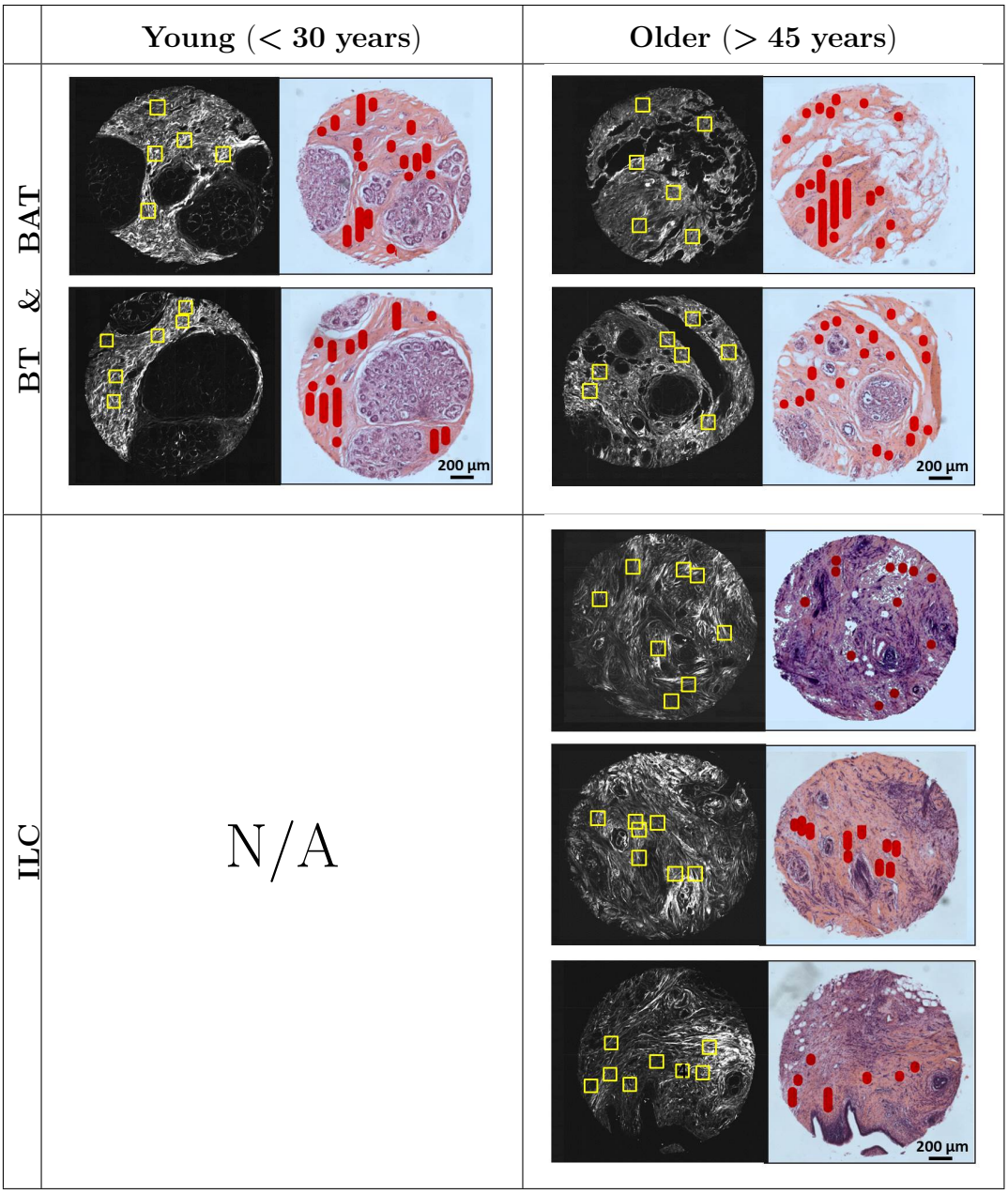

Figure 6.2: SHG (black-and-white) and H&E stained (color) images of consecutively cut sections of breast TMA cores from *benign tissues* (BT), *benign adjacent tissues* (BAT) and *invasive lobular carcinoma* (ILC). Regions of interest marked in red in the H&E images guide the selection of regions which undergo SPPARC analysis (marked by yellow boxes in the SHG images).

properties change most in the vicinity of tumors. We highlight in Fig. 6.4 the error bar comparisons of different parameters between BAT and ILC in collagen and the EFMC (the full plots showing comparison between BT, BAT and

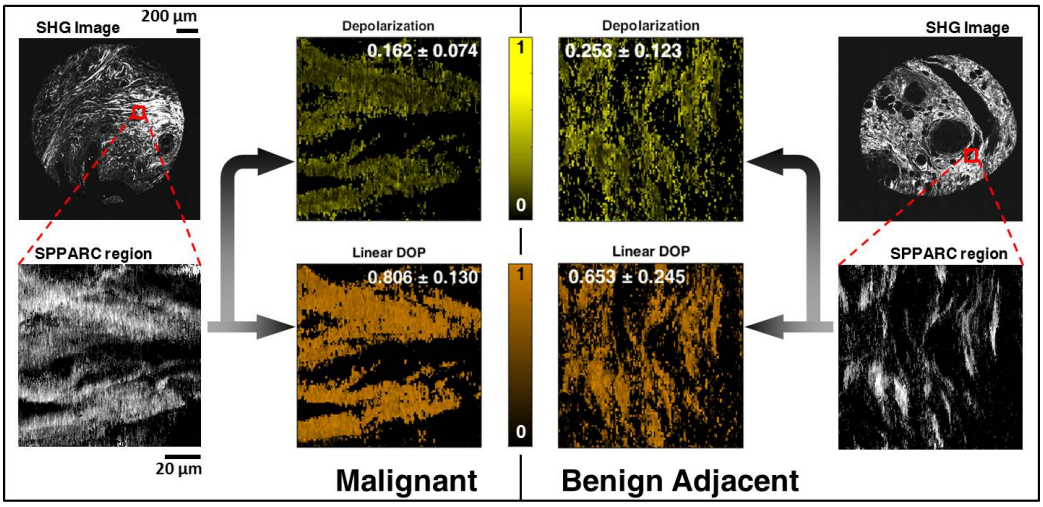

Figure 6.3: Two TMA sample cores: one each from ILC (top left) and BAT (top right) core. SPPARC images for selected regions with stromal collagen within tumor for ILC and stromal collagen in benign tissue adjacent to tumor for BAT are shown. The corresponding depolarization and linear DOP parameter spatial maps are also shown, revealing a lower depolarization and higher linear degree-of-polarization for stromal collagen within tumor.

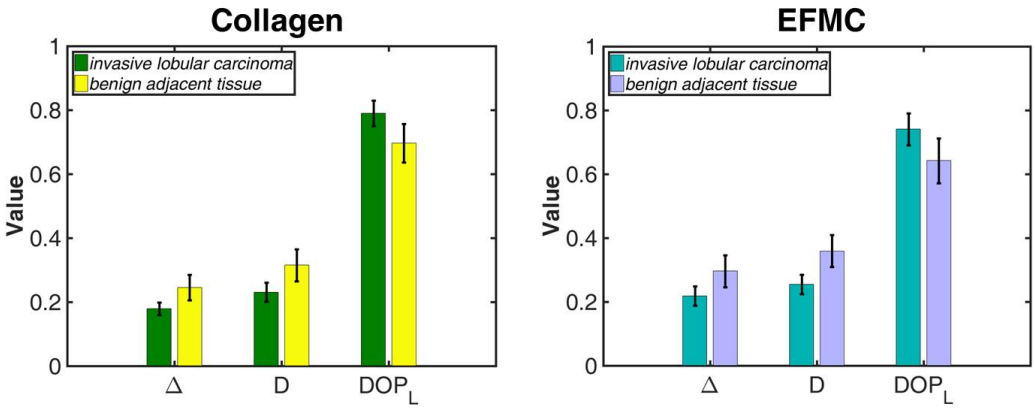

Figure 6.4: Plots of parameter mean and standard deviation comparing stromal collagen within tumor (ILC) with stromal collagen in benign tissue adjacent to tumor (BAT) for both collagen and the EFMC. The two plots exhibit similar trend of lower depolarization, lower diattenuation and higher linear degree-of-polarization for stromal collagen within malignant tissue.

ILC are shown in the Supplementary Information). As previously observed in the analysis of a pair of regions, stromal collagen within malignant tissues shows average lower Δ values than in BAT. We hypothesize that this may

be due to the fact that malignancy induces less optical scattering, and hence less polarization decoherence, as a result of stiffening of the surrounding stromal collagen. Stromal stiffening is an effect of increased matrix deposition leading to cross-linking in the tumor micro-environment [152, 171, 172]. A similar trend of reduced D for stromal collagen within ILC implies a reduction of preferential absorption of incident polarized light. We propose that this may be due to the loss in general optical anisotropy in stromal collagen [173], influenced by the haphazard growth and invasive behavior of the tumor. $\mathrm{DOP_L}$ shows the reverse trend, with stromal collagen in ILC preserving linear degree-of-polarization more than collagen in BAT. The overall stromal collagen relationship is also noted for the EFMC, although there appears to be slightly higher spread in the parameter variation as captured by the standard deviation.

It is important to note that the stromal collagen regions around malignant tissues assessed are themselves not classified as malignant. However, we do note differences in the polarization response depending on whether the collagen is in the vicinity of the tumors, adjacent to tumors or in benign tissues. When the malignancy arises from stromal collagen and other mesenchymal tissues, it is referred to as sarcoma [19, 174], which is not what we believe to be the case here.

6.4 Summary

In conclusion, we experimentally demonstrated the consistency of SPPARC analysis, and compared metrics between perilobular stroma in benign mammary tissue, and the available stroma adjacent to and surrounding malignant *invasive lobular carcinoma*. To our knowledge, this is the first time that such comparison of the linear Mueller matrix polarization response targeting stromal collagen in *benign* and around *malignant* breast tissues has been done. The most noticeable differences in metrics occur between BAT and stromal tissue around malignant tissues, where depolarization, diattenuation and linear degree-of-polarization appear to be sensitive tissue pathology. A key observation is that stroma surrounding malignant tissues shows lower depolarization, lower diattenuation and higher linear degree-of-polarization than stroma adjacent to malignant tissues. These results pave the way for an

expanded study involving more varied pathologies, and multivariate analysis that incorporates age, disease stage and more pathology diagnoses.

A current limitation is the data acquisition time for SPPARC microscopy. The process is currently being optimized for faster acquisition. In addition, experiments suggest that the parameter sensitivity increases with sample thickness, and hence use of thicker samples will enhance the differences in polarimetric effect, and aid in more accurate distinction of pathologies. Furthermore, a potentially interesting study would be a comparison of the polarization response between the briefly highlighted sarcoma and benign stromal collagen.

CHAPTER 7

CONCLUSION

This dissertation reports on work done to incorporate polarization metrology with nonlinear collagen-specific microscopy in order to quantitatively assess stromal collagen for deeper understanding and potential diagnostic and prognostic insight. In particular, the development and demonstration of two second-harmonic generation and Mueller matrix based techniques were shown – Mueller matrix second-harmonic generation (MMSHG) microscopy and second-harmonic patterned polarization analyzed reflection confocal (SPPARC) microscopy. The latter was then used to assess the stroma within and adjacent to breast biopsies.

MMSHG microscopy, based on a nonlinear generalized extension of the linear Mueller matrix, was experimentally demonstrated for extracting nonlinear Mueller matrices used to quantitatively assess collagen samples. Specifically, the output Stokes vector was measured and used to determine the two-photon Mueller matrix and degree of polarization. A new metric, the bimodal mean difference (μ_d), was derived from the degree of polarization distribution model and it was observed that this metric showed increasing variation with thickness of porcine tendon samples. The increased variation is expected since thicker samples scatter light more.

SPPARC microscopy was implemented for generation of three-dimensional SHG-patterned confocal microscopy images of collagen fibers. Linear polarimetric analysis and matrix decomposition methods were employed in order to obtain rich polarization information. It was shown that SPPARC microscopy allowed for label-free quantitative analysis of the EFMC. Using MMPD as a decomposition approach, we highlighted differences in average parameter values between tendon and PCL collagen, and observed that PCL preserves circular DOP more (and hence has less total depolarization) than tendon collagen. The variation in parameters was not as pronounced for the comparison between tendon collagen and tendon EFMC. These parameter changes were

tracked across layers for collagen in tendon. The retardance parameters, in particular, showed gradually reducing values for deeper penetration.

SPPARC was then applied for analysis of the perilobular stroma in benign mammary tissue, and the available stroma adjacent to (*benign adjacent tissue*, or BAT) and surrounding malignant *invasive lobular carcinoma* (ILC). The most noticeable differences in metrics occur between BAT and stromal tissue around malignant tissues, where depolarization, diattenuation and linear degree-of-polarization appear to be sensitive tissue pathology. It was also observed that the stroma surrounding malignant tissues showed lower depolarization, lower diattenuation and higher linear degree-of-polarization than the stroma adjacent to malignant tissues.

7.1 Future directions

Establishing a robust model for polarization investigative techniques, that can reveal intuitive parameters for describing collagen properties, is an overarching goal for this research work. Hence, one future direction would be developing such polarization models, and attempting to link them with currently existing parameters, verifiable by experiments. Preliminary work done on one such analysis using a simple polarization model in comparing MMSHG and SPPARC data is discussed in the next section.

7.1.1 Comparison of MMSHG and SPPARC data

As already explained, MMSHG and SPPARC microscopy both use the idea of combining SHG microscopy with Mueller matrix polarimetric metrology to retrieve parameters that are descriptive of the polarization response of the sample. However, how they go about integrating these techniques are different. While MMSHG imaging is performed in the forward direction and uses nonlinear polarimetry on the second-harmonic signals, SPPARC signals are collected in the epi-direction and polarimetry is done on the linear confocal signals; SHG is only used as a mask in the latter case. Even though some of the metrics obtained have similar definitions, it may not be trivial to relate them simply, especially because of the nonlinearity that exists for polarimetry on second-order signals. Hence, we re-examine the underlying

mechanism of signal generation in both techniques, propose a hypothesis on how we think signal scattering affects the optical properties and compare experimental results.

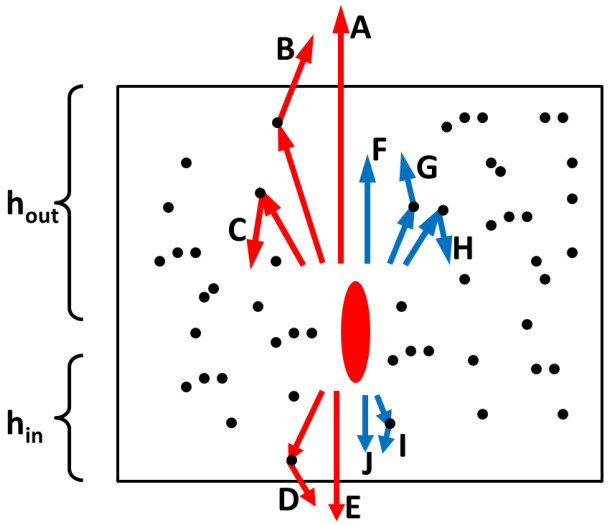

Figure 7.1: Simple scattering model showing paths linear photons (red) and second-order photons (blue) can take after interaction in a focal volume.

Figure 7.1 shows an illustration of a proposed model showing different paths light can take after scattering from a focal volume (shown by the ellipse) for a given thickness [$\approx h_{\text{in}}+h_{\text{out}}$] of a sample having scatterers. For the linear scattering case (shown in red), there are five scattering events shown. The rays marked A are the forward ballistic photons, while those marked B are the forward snake photons (ballistic photons are photons with no scattering, while snake photons are those with minimal 'snaking' scattering [175]). Rays C are the forward scattered photons for which severe scattering causes backward propagation. Rays D and E are the generated backward ballistic and snake photons, respectively. It is expected that photons can bounce around multiple times, but we assume that the intensity will be negligible for two or more scattering events. The model for the linearly scattered signal is the same for the second-harmonic signals (shown in blue and labeled F to J), though the intensity is considerably smaller. MMSHG deals with the nonlinear rays F, G. SPPARC deals with linear rays C, D, E (and uses rays H, I, J for masking).

Supposing we set h_{in} to be small enough that its scattering and absorption

effects on the excitation field are negligible, then we can proceed to make a few predictions. An obvious one is that the smaller h_{out} is, the 'sharper' the image, since there is less scattering of the signals. This means that MMSHG images would have less depolarization (effectively more average degree-of-polarization), and smaller bimodal mean difference μ_d. Also, the thicker h_{out} is, the larger the SPPARC linear and SHG signals become, because there is a greater distance over which photons C and H can occur. This means that given an imaging depth h_{in}, the backward scattered signals increase with h_{out}. Equivalently, the penetration depth achievable increases with sample thickness. In terms of polarimetric information, we expect that the greater contribution of scattered signals would result in more depolarization for thicker samples.

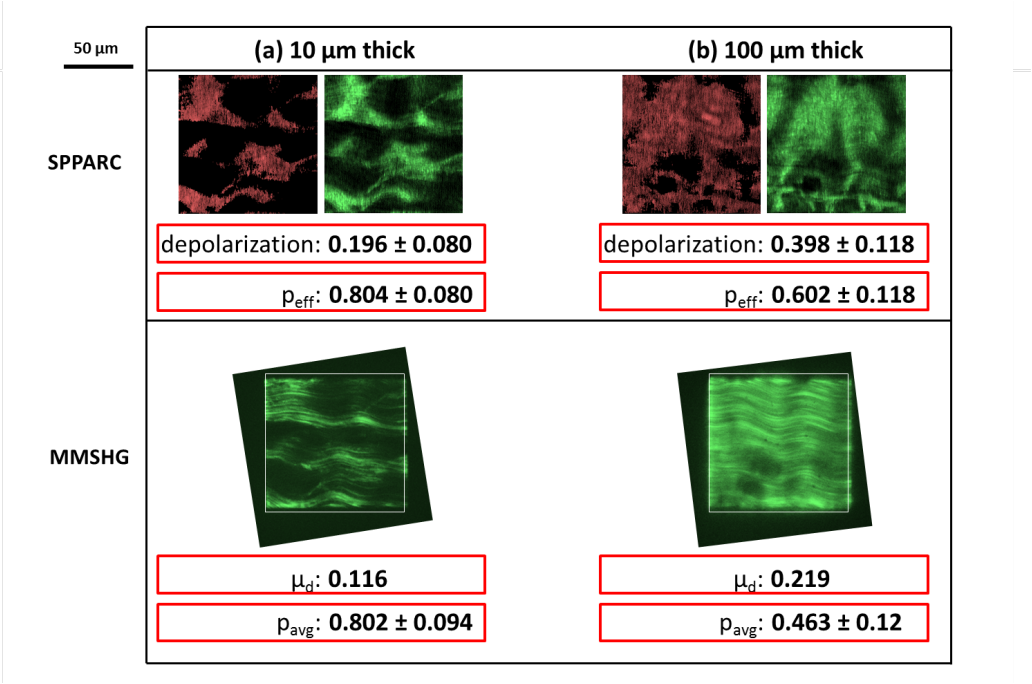

Figure 7.2: Comparison of SPPARC and MMSHG parameters for (a) 10 μm and (b) 100 μm thick porcine tendon at an imaging depth of 5 μm. We observe that for thicker samples, there is less nonlinear p_{eff} and less linear p_{avg} and μ_d

These observations give us a basis to correlate (albeit roughly) parameters such as SPPARC linear depolarization on the one hand, and MMSHG bimodal mean difference and average degree-of-polarization (p_{avg}). The latter is the p average obtained across all probing input polarizations. A series of

experiments were carried out on 10 μm and 100 μm thick porcine tendon samples at an imaging depth of $h_{\text{in}} = 5$ μm. An effective degree-of-polarization parameter p_{eff}=$(1 - \Delta)$ is introduced for SPPARC to maintain consistency with p_{avg} $(= \frac{1}{9}\sum_{m=0}^{9} p_m)$ from MMSHG. Figure 7.2 shows the results obtained. It is observed that the 10 μm thick collagen samples have higher SPPARC p_{eff} than 100 μm thick samples. As stated earlier, we suggest that this is due to greater probability of C-type rays for the thicker sample. We also notice that the MMSHG p_{avg} for the same region has higher values in 10 μm thick samples, along with lower μ_d mean, still pointing to the effects of scattering. More experiments over a variety of thicknesses should be carried out to make stronger statements about trend consistency, and to make comments on other parameters such as retardance and diattenuation.

7.1.2 Other directions

By combining with other polarization and non-polarization based techniques, SHG can be used as a delineating mask to reveal properties that are particular to collagenous tissues. For example, it can be integrated with third-harmonic generation imaging (THG) to probe collagen interface effects as well as spectroscopic imaging for collagen content analysis.

Another area for future research will involve optimization of the optical setup to allow for faster acquisition. This will necessitate parallel optimization of the data acquisition code for the detector, and use of automated liquid crystal elements for polarization state generation and analysis. Achieving this will enable stronger statistical significance for experimental data due to the ability to investigate higher number and greater diversity of samples.

The current analysis methods for Mueller matrices could also be extended to other methods (such as differential matrix decomposition), because even though these take more computational resources, they are potentially more insightful. In addition, not all matrices extracted during the imaging process are physically realizable (due to noise and detection error). By optimizing for the closest possible realizable matrix using computational approaches, more accurate representative data can be extracted.

APPENDIX A

POLARIMETRIC MEASUREMENTS

Linear and nonlinear polarimetric measurement angles for the PSG and PSA module arrangement using discrete optical components (Fig. A.1) are shown in Tables A.1 and A.2, respectively. The gray rows specify measurements taken for only nonlinear polarimetry.

Table A.1: Linear polarizer, quarter-wave plate and half-wave plate combinations for the polarization state generator

PSG State	**LP Angle (^{o})**	**HWP Angle (^{o})**	**QWP Angle (^{o})**
H	0.00	0.00	
V	0.00	45.00	
P	0.00	22.50	
P^*	0.00	337.50	
R	0.00	22.50	90.00
R^*	0.00	337.50	90.00
H_P	0.00	11.25	
V_{R^*}	0.00	56.25	90.00
P_R^*	0.00	56.25	135.00

Table A.2: Linear polarizer, quarter-wave plate and half-wave plate combinations for the polarization state analyzer.

PSA State	**QWP Angle (^{o})**	**HWP Angle (^{o})**	**LP Angle (^{o})**
H		0.00	0.00
V		45.00	0.00
P		22.50	0.00
P^*		337.50	0.00
R	90.00	22.50	0.00
R^*	90.00	337.50	0.00

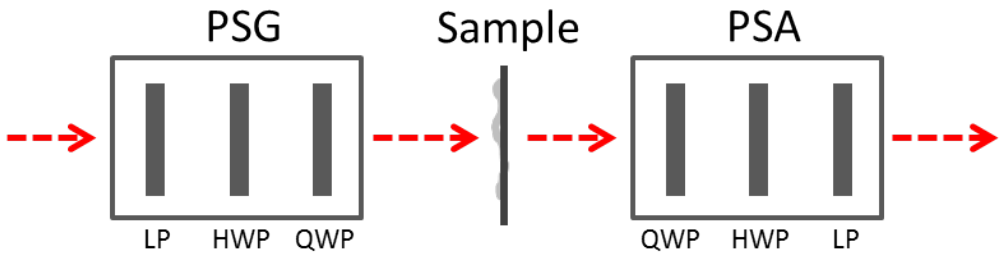

Figure A.1: Arrangement of discrete optical components for polarimetric measurements.

Calibration for the discrete optical components proceeds in this way:

- Linear polarizers are characterized using another reference linear polarizer. The Malus' curve shows a cosine-squared curve having maximum intensity ($I_{\max}$) when the polarizers have their axis aligned, and minimum intensity ($I_{\min}$) when the axes are orthogonal to each other (90° angle). The quality of the polarizer can be captured by the extinction ratio ($\frac{I_{\max}}{I_{\min}}$).

- Half-wave plates can be calibrated using two linear polarizers. When the polarizers are aligned, rotating the half-wave plate also produces the cosine-squared curve, with a maximum when the fast-axis of the wave-plate is aligned with the polarizers and a minimum (≈ 0) when it is 45° to the polarizer axes. If the polarizer axes are originally orthogonal to each other, the cosine-squared curve has its maximum and minimum shifted by 45°.

- Quarter-wave plates can be calibrated by also using two linear polarizers. For aligned polarizers, rotating the quarter-wave plate produces a cosine-squared curve that goes from a maximum when the fast-axis of the wave-plate is aligned with the polarizers to a minimum value when it is 45° to the polarizers' axes. However, this minimum is not ≈ 0, but is $\approx \frac{I_{\max}}{2}$. If the polarizer axes are orthogonal to each other, the cosine-squared curve has its maximum at when the half-wave plate is 45° to either polarizer axis.

APPENDIX B

MUELLER MATRIX ANALYSIS

B.1 Some polarization parameters

Table B.1: Description of selected scalar parameters obtainable from the sub-matrix decomposition of the Mueller matrix (first two), and directly from the Mueller matrix (last three) [117, 176]

Scalar Metric	**Mathematical Definition**	**Description**
diattenuation	$D = \text{norm}(\vec{D})$	Measure of the dependence of the transmittance of the system on incident polarization. Obtained from the diattenuation vector.
depolarization	$\Delta = 1 - \frac{\lvert\text{Tr}(\boldsymbol{M_R}) - 1\rvert}{3}$	Measure of depolarization power of the depolarizer matrix on a polarized incident source. Obtained from the depolarization matrix.
linear retardance	$R_L = \cos^{-1}[((m_{R11} + m_{R22})^2 + (m_{R11} + m_{R22})^2)^{\frac{1}{2}} - 1]$	Degree of change in retardance for linearly polarized light.
linear DOP	$DOP_L = \frac{m_{10} + m_{11}}{m_{00} + m_{01}}$	Degree to which linearly polarized input light preserves its polarization. state.
circular DOP	$DOP_C = \frac{m_{30} + m_{33}}{m_{00} + m_{03}}$	Degree to which circularly polarized input light preserves its polarization. state.

B.2 Mueller matrix polar decomposition

Given a Mueller matrix $\boldsymbol{M}$, we can proceed to decompose in the following way:

- Find $\vec{D}^T$ by taking the top right 1×3 row vector; this is the diattenuation vector.
- Find $\vec{P}$ by taking the bottom left 3×1 column vector; this is the polarizance vector.
- We then obtain the diattenuation submatrix as:

$$\boldsymbol{m_D} = \sqrt{1-D^2}\boldsymbol{I} + (1-\sqrt{1-D^2})\hat{D}\hat{D}^T, \tag{B.1}$$

  where $\boldsymbol{I}$ is the 3×3 identity matrix, $D = \sqrt{D_1^2 + D_2^2 + D_3^2}$ is the diattenuation scalar and $\hat{D} = \frac{\vec{D}}{D}$ is the unit diattenution vector. We then also obtain $\boldsymbol{M_D}$.

- We solve for $\boldsymbol{M'} = \boldsymbol{M_\Delta M_R}$ by:

$$\boldsymbol{M'} = \boldsymbol{M}\boldsymbol{M_D^{-1}} \quad . \tag{B.2}$$

  We take the bottom right 3×3 submatrix of $\boldsymbol{M'}$ as $\boldsymbol{m'}$.

- Next we obtain $\boldsymbol{m_\Delta}$ as

$$\begin{aligned}\boldsymbol{m_\Delta} = \pm &\left[\boldsymbol{m'}(\boldsymbol{m'})^T + (\sqrt{\lambda_1\lambda_2} + \sqrt{\lambda_2\lambda_3} + \sqrt{\lambda_1\lambda_3})\boldsymbol{I}\right]^{-1} \\ &\times \left[(\sqrt{\lambda_1} + \sqrt{\lambda_2} + \sqrt{\lambda_3})\boldsymbol{m'}(\boldsymbol{m'})^T + \sqrt{\lambda_1\lambda_2\lambda_3}\boldsymbol{I}\right] \quad .\end{aligned} \tag{B.3}$$

- We obtain the depolarization polarizance vector $\vec{P}_\Delta$ as:

$$\vec{P}_\Delta = \frac{\vec{P} - \boldsymbol{m}\vec{D}}{1-D^2} \quad . \tag{B.4}$$

- We can now build up $\boldsymbol{M_\Delta}$ from $\boldsymbol{m_\Delta}$ and $\vec{P}_\Delta$. The depolarization scalar is obtained as $\Delta = 1 - \frac{|\mathrm{Tr}(\boldsymbol{m_\Delta})|}{3}$.

- Lastly, we can solve for $\boldsymbol{M_R}$ using

$$\boldsymbol{M_R} = \boldsymbol{M_\Delta^{-1}} \boldsymbol{M'} \quad . \tag{B.5}$$

The retardance scalar, $R = \cos^{-1}\left[\frac{\mathrm{Tr}(\boldsymbol{M_R})}{2} - 1\right]$.

APPENDIX C

COMMENTS ON SOME EXPERIMENTAL SPECIFICATIONS

C.1 Laser source

The laser source used for all experiments is the Mai Tai HP mode-locked Ti:sapphire laser from Spectra-Physics. It is able to generate femtosecond pulses (required for efficient second-harmonic generation) over a broadband wavelength (λ) range from 690 nm to 1020 nm. However, all experiments are carried out at **780 nm** (laser settings are optimized at 800 nm), with light having a pulse width of < 100 fs.

C.2 Detectors

Two detectors are used for capturing SHG and confocal images. The forward detection (for MMSHG experiments) uses a water cooled Hamamatsu ImagEM C9100-13 electron multiplying charge-coupled device (EMCCD) having 512×512 16 μm pixels, suited for high dynamic range imaging. For epi-detection (in SPPARC experiments), a H10721 Hamamatsu photosensor module containing a photomultiplier tube (PMT) with high gain is used. Sources of noise include dark noise (for the EMCCD), ripple noise (for the PMT) and shot noise.

C.3 Acquisition speed

The acquisition speed differs for the forward and backward images. Since the forward collection uses a random galvo-scan, and full field-of-view imaging, the typical acquisition time for a 512×512 pixel image of a 5 μm porcine tendon sample is 2 s (exposure time). This translates to an ~ 8 μs pixel dwell

time. Of course, this considers SNR of good visual quality. For the backward collected signal, the requirement of a galvo raster-scan and a PMT readout for point-by-point image building necessitates tight synchronization. The experiments achieved an acquisition time of $\sim$50 s, yielding a pixel-dwell time of $\sim$190 μs. The speed of acquisition can be increased with implementation of an electro-optic or acousto-optic modulator, and faster synchronization program.

REFERENCES

[1] H. Tom, T. Heinz, and Y. Shen, "Second-harmonic reflection from silicon surfaces and its relation to structural symmetry," *Physical Review Letters*, vol. 51, no. 21, 1983.

[2] Y. Shen, "Surface properties probed by second-harmonic and sum-frequency generation," *Nature*, vol. 337, no. 6207, p. 519, 1989.

[3] Y. Li, Y. Rao, K. F. Mak, Y. You, S. Wang, C. R. Dean, and T. F. Heinz, "Probing symmetry properties of few-layer MoS_2 and h-BN by optical second-harmonic generation," *Nano Letters*, vol. 13, no. 7, pp. 3329–3333, 2013.

[4] A. Rubano, T. Günter, M. Lilienblum, C. Aruta, F. M. Granozio, U. S. di Uccio, L. Marrucci, D. Paparo, and M. Fiebig, "Optical second harmonic imaging as a diagnostic tool for monitoring epitaxial oxide thin-film growth," *Applied Surface Science*, vol. 327, pp. 413–417, 2015.

[5] G. A. Di Lullo, S. M. Sweeney, J. Körkkö, L. Ala-Kokko, and J. D. San Antonio, "Mapping the ligand-binding sites and disease-associated mutations on the most abundant protein in the human, type I collagen," *Journal of Biological Chemistry*, vol. 277, no. 6, pp. 4223–4231, 2002.

[6] H. Lodish, A. Berk, S. L. Zipursky, P. Matsudaira, D. Baltimore, and J. Darnell, *Molecular Cell Biology*. 4th edition. W H Freeman, 2000.

[7] R. C. Billinghurst, L. Dahlberg, M. Ionescu, A. Reiner, R. Bourne, C. Rorabeck, P. Mitchell, J. Hambor, O. Diekmann, H. Tschesche et al., "Enhanced cleavage of type ii collagen by collagenases in osteoarthritic articular cartilage." *The Journal of Clinical Investigation*, vol. 99, no. 7, pp. 1534–1545, 1997.

[8] Y. Komai and T. Ushiki, "The three-dimensional organization of collagen fibrils in the human cornea and sclera." *Investigative Ophthalmology & Visual Science*, vol. 32, no. 8, pp. 2244–2258, 1991.

[9] E. J. Miller, E. H. Epstein Jr, and K. A. Piez, "Identification of three genetically distinct collagens by cyanogen bromide cleavage of insoluble human skin and cartilage collagen," *Biochemical and Biophysical Research Communications*, vol. 42, no. 6, pp. 1024–1029, 1971.

[10] W. Cheng, R. Yan-hua, N. Fang-gang, and Z. Guo-an, "The content and ratio of type I and III collagen in skin differ with age and injury," *African Journal of Biotechnology*, vol. 10, no. 13, pp. 2524–2529, 2011.

[11] D. R. Keene, L. Y. Sakai, and R. E. Burgeson, "Human bone contains type iii collagen, type vi collagen, and fibrillin: type iii collagen is present on specific fibers that may mediate attachment of tendons, ligaments, and periosteum to calcified bone cortex." *Journal of Histochemistry & Cytochemistry*, vol. 39, no. 1, pp. 59–69, 1991.

[12] K. von der Mark, V. Gauss, H. von der Mark, and P. Müller, "Relationship between cell shape and type of collagen synthesised as chondrocytes lose their cartilage phenotype in culture," *Nature*, vol. 267, no. 5611, p. 531, 1977.

[13] K. T. Weber, Y. Sun, S. C. Tyagi, and J. P. Cleutjens, "Collagen network of the myocardium: function, structural remodeling and regulatory mechanisms," *Journal of Molecular and Cellular Cardiology*, vol. 26, no. 3, pp. 279–292, 1994.

[14] S. D. Hauschka and I. R. Konigsberg, "The influence of collagen on the development of muscle clones," *Proceedings of the National Academy of Sciences*, vol. 55, no. 1, pp. 119–126, 1966.

[15] M. P. Lynch, J. L. Stein, G. S. Stein, and J. B. Lian, "The influence of type i collagen on the development and maintenance of the osteoblast phenotype in primary and passaged rat calvarial osteoblasts: modification of expression of genes supporting cell growth, adhesion, and extracellular matrix mineralization," *Experimental Cell Research*, vol. 216, no. 1, pp. 35–45, 1995.

[16] M. E. Nimni, "Collagen: structure, function, and metabolism in normal and fibrotic tissues," in *Seminars in Arthritis and Rheumatism*, vol. 13, no. 1. Elsevier, 1983, pp. 1–86.

[17] S. M. Weis, J. L. Emery, K. D. Becker, D. J. McBride, J. H. Omens, and A. D. McCulloch, "Myocardial mechanics and collagen structure in the osteogenesis imperfecta murine (OIM)," *Circulation Research*, vol. 87, no. 8, pp. 663–669, 2000.

[18] R. Ambekar, K. C. Toussaint Jr, and A. W. Johnson, "The effect of keratoconus on the structural, mechanical, and optical properties of the cornea," *Journal of the Mechanical Behavior of Biomedical Materials*, vol. 4, no. 3, pp. 223–236, 2011.

[19] C. Adem, C. Reynolds, J. N. Ingle, and A. Nascimento, "Primary breast sarcoma: clinicopathologic series from the Mayo Clinic and review of the literature," *British Journal of Cancer*, vol. 91, no. 2, p. 237, 2004.

[20] C. L. Hall, J. Dai, K. L. van Golen, E. T. Keller, and M. W. Long, "Type i collagen receptor ($\alpha 2\beta 1$) signaling promotes the growth of human prostate cancer cells within the bone," *Cancer Research*, vol. 66, no. 17, pp. 8648–8654, 2006.

[21] D. M. Gilkes, P. Chaturvedi, S. Bajpai, C. C. Wong, H. Wei, S. Pitcairn, M. E. Hubbi, D. Wirtz, and G. L. Semenza, "Collagen prolyl hydroxylases are essential for breast cancer metastasis," *Cancer Research*, vol. 73, no. 11, pp. 3285–3296, 2013.

[22] K. Zhang, C. A. Corsa, S. M. Ponik, J. L. Prior, D. Piwnica-Worms, K. W. Eliceiri, P. J. Keely, and G. D. Longmore, "The collagen receptor discoidin domain receptor 2 stabilizes snail1 to facilitate breast cancer metastasis," *Nature Cell Biology*, vol. 15, no. 6, p. 677, 2013.

[23] S. L. Jacques, J. R. Roman, and K. Lee, "Imaging superficial tissues with polarized light," *Lasers in Surgery and Medicine*, vol. 26, no. 2, pp. 119–129, 2000.

[24] W. Kaminsky, K. Claborn, and B. Kahr, "Polarimetric imaging of crystals," *Chemical Society Reviews*, vol. 33, no. 8, pp. 514–525, 2004.

[25] A. Weber, M. C. Cheney, Q. Y. Smithwick, and A. E. Elsner, "Polarimetric imaging and blood vessel quantification," *Optics Express*, vol. 12, no. 21, pp. 5178–5190, 2004.

[26] Q. Hu, L.-L. Tay, M. Noestheden, and J. P. Pezacki, "Mammalian cell surface imaging with nitrile-functionalized nanoprobes: biophysical characterization of aggregation and polarization anisotropy in sers imaging," *Journal of the American Chemical Society*, vol. 129, no. 1, pp. 14–15, 2007.

[27] Y. Pu, W. Wang, S. Achilefu, B. Das, G. Tang, V. Sriramoju, and R. Alfano, "Time-resolved fluorescence polarization anisotropy and optical imaging of cybesin in cancerous and normal prostate tissues," *Optics Communications*, vol. 274, no. 1, pp. 260–267, 2007.

[28] P. Whittaker, D. R. Boughner, and R. Kloner, "Analysis of healing after myocardial infarction using polarized light microscopy." *The American Journal of Pathology*, vol. 134, no. 4, p. 879, 1989.

[29] R. Oldenbourg and G. Mei, "New polarized light microscope with precision universal compensator," *J. Microsc.*, vol. 180, no. 2, pp. 140–147, 1995.

[30] G. Yao and L. V. Wang, "Two-dimensional depth-resolved Mueller matrix characterization of biological tissue by optical coherence tomography," *Optics Letters*, vol. 24, no. 8, pp. 537–539, 1999.

[31] D. Lara and C. Dainty, "Axially resolved complete Mueller matrix confocal microscopy," *Applied Optics*, vol. 45, no. 9, pp. 1917–1930, 2006.

[32] P. G. Ellingsen, M. B. Lilledahl, L. M. S. Aas, C. de Lange Davies, and M. Kildemo, "Quantitative characterization of articular cartilage using Mueller matrix imaging and multiphoton microscopy," *Journal of Biomedical Optics*, vol. 16, no. 11, p. 116002, 2011.

[33] C. Bonnans, J. Chou, and Z. Werb, "Remodelling the extracellular matrix in development and disease," *Nature Reviews Molecular Cell Biology*, vol. 15, no. 12, p. 786, 2014.

[34] R. O. Hynes, "The extracellular matrix: not just pretty fibrils," *Science*, vol. 326, no. 5957, pp. 1216–1219, 2009.

[35] R. O. Hynes and A. Naba, "Overview of the matrisomean inventory of extracellular matrix constituents and functions," *Cold Spring Harbor Perspectives in Biology*, vol. 4, no. 1, p. a004903, 2012.

[36] S. Ricard-Blum, F. Ruggiero, and M. van der Rest, "The collagen superfamily," in *Collagen*. Springer, 2005, pp. 35–84.

[37] P. Fratzl, "Collagen: structure and mechanics, an introduction," in *Collagen*. Springer, 2008, pp. 1–13.

[38] B. R. Masters, P. T. So et al., *Handbook of Biomedical Nonlinear Optical Microscopy*. Oxford University Press New York:, 2008.

[39] S. Roth and I. Freund, "Second harmonic generation in collagen," *The Journal of Chemical Physics*, vol. 70, no. 4, pp. 1637–1643, 1979.

[40] X. Chen, O. Nadiarynkh, S. Plotnikov, and P. J. Campagnola, "Second harmonic generation microscopy for quantitative analysis of collagen fibrillar structure," *Nature Protocols*, vol. 7, no. 4, pp. 654–669, 2012.

[41] Proto-col World, "The collagen molecule," https://www.proto-col.com/blog/2014/07/30/collagen/, 2014.

[42] D. J. Maitland and J. T. Walsh, "Quantitative measurements of linear birefringence during heating of native collagen," *Lasers in Surgery and Medicine*, vol. 20, no. 3, pp. 310–318, 1997.

[43] M. Wolman, "Polarized light microscopy as a tool of diagnostic pathology," *Journal of Histochemistry & Cytochemistry*, vol. 23, no. 1, pp. 21–50, 1975.

[44] M. C. Pierce, R. L. Sheridan, B. H. Park, B. Cense, and J. F. de Boer, "Collagen denaturation can be quantified in burned human skin using polarization-sensitive optical coherence tomography," *Burns*, vol. 30, no. 6, pp. 511–517, 2004.

[45] K. Okuyama, K. Okuyama, S. Arnott, M. Takayanagi, and M. Kakudo, "Crystal and molecular structure of a collagen-like polypeptide (pro-pro-gly) 10," *Journal of Molecular Biology*, vol. 152, no. 2, pp. 427–443, 1981.

[46] R. Z. Kramer, L. Vitagliano, J. Bella, R. Berisio, L. Mazzarella, B. Brodsky, A. Zagari, and H. M. Berman, "X-ray crystallographic determination of a collagen-like peptide with the repeating sequence (Pro-Pro-Gly) 1," *Journal of Molecular Biology*, vol. 280, no. 4, pp. 623–638, 1998.

[47] R. Berisio, L. Vitagliano, L. Mazzarella, and A. Zagari, "Crystal structure of the collagen triple helix model [(pro-pro-gly) 10] 3," *Protein Science*, vol. 11, no. 2, pp. 262–270, 2002.

[48] D. J. Hulmes and A. Miller, "Quasi-hexagonal molecular packing in collagen fibrils," *Nature*, vol. 282, no. 5741, p. 878, 1979.

[49] K. Gelse, E. Pöschl, and T. Aigner, "Collagensstructure, function, and biosynthesis," *Advanced Drug Delivery Reviews*, vol. 55, no. 12, pp. 1531–1546, 2003.

[50] W. F. Vogel, "Collagen-receptor signaling in health and disease." *European Journal of Dermatology: EJD*, vol. 11, no. 6, pp. 506–514, 2001.

[51] S. P. Sugrue and E. D. Hay, "Response of basal epithelial cell surface and cytoskeleton to solubilized extracellular matrix molecules." *The Journal of Cell Biology*, vol. 91, no. 1, pp. 45–54, 1981.

[52] Y. Yamaguchi, D. M. Mann, and E. Ruoslahti, "Negative regulation of transforming growth factor-β by the proteoglycan decorin," *Nature*, vol. 346, no. 6281, p. 281, 1990.

[53] B. Hinz, "The extracellular matrix and transforming growth factor-β1: tale of a strained relationship," *Matrix Biology*, vol. 47, pp. 54–65, 2015.

[54] F. Rauch and F. H. Glorieux, "Osteogenesis imperfecta," *The Lancet*, vol. 363, no. 9418, pp. 1377–1385, 2004.

[55] T. T. Andreassen, A. H. Simonsen, and H. Oxlund, "Biomechanical properties of keratoconus and normal corneas," *Experimental Eye Research*, vol. 31, no. 4, pp. 435–441, 1980.

[56] WebMD, "Sarcoma," https://www.webmd.com/cancer/sarcoma#1, 2018.

[57] M. Wolman and F. Kasten, "Polarized light microscopy in the study of the molecular structure of collagen and reticulin," *Histochemistry and Cell Biology*, vol. 85, no. 1, pp. 41–49, 1986.

[58] A. Changoor, M. Nelea, S. Methot, N. Tran-Khanh, A. Chevrier, A. Restrepo, M. Shive, C. Hoemann, and M. Buschmann, "Structural characteristics of the collagen network in human normal, degraded and repair articular cartilages observed in polarized light and scanning electron microscopies," *Osteoarthritis and Cartilage*, vol. 19, no. 12, pp. 1458–1468, 2011.

[59] L. Rich and P. Whittaker, "Collagen and picrosirius red staining: a polarized light assessment of fibrillar hue and spatial distribution," *Braz. J. Morphol. Sci.*, vol. 22, no. 2, pp. 97–104, 2005.

[60] L. C. U. Junqueira, G. Bignolas, and R. Brentani, "Picrosirius staining plus polarization microscopy, a specific method for collagen detection in tissue sections," *The Histochemical Journal*, vol. 11, no. 4, pp. 447–455, 1979.

[61] J. M. Clark, "The organization of collagen in cryofractured rabbit articular cartilage: a scanning electron microscopic study," *Journal of Orthopaedic Research*, vol. 3, no. 1, pp. 17–29, 1985.

[62] J. M. Clark, "Variation of collagen fiber alignment in a joint surface: a scanning electron microscope study of the tibial plateau in dog, rabbit, and man," *Journal of Orthopaedic Research*, vol. 9, no. 2, pp. 246–257, 1991.

[63] B. Alexander, T. L. Daulton, G. M. Genin, J. Lipner, J. D. Pasteris, B. Wopenka, and S. Thomopoulos, "The nanometre-scale physiology of bone: steric modelling and scanning transmission electron microscopy of collagen–mineral structure," *Journal of the Royal Society Interface*, vol. 9, no. 73, pp. 1774–1786, 2012.

[64] T. Starborg, N. S. Kalson, Y. Lu, A. Mironov, T. F. Cootes, D. F. Holmes, and K. E. Kadler, "Using transmission electron microscopy and 3View to determine collagen fibril size and three-dimensional organization," *Nature Protocols*, vol. 8, no. 7, p. 1433, 2013.

[65] R. Cameron and A. Donald, "Minimizing sample evaporation in the environmental scanning electron microscope," *Journal of Microscopy*, vol. 173, no. 3, pp. 227–237, 1994.

[66] A. Young, I. Legrice, M. Young, and B. Smaill, "Extended confocal microscopy of myocardial laminae and collagen network," *Journal of Microscopy*, vol. 192, no. 2, pp. 139–150, 1998.

[67] P. C. Dolber and M. Spach, "Conventional and confocal fluorescence microscopy of collagen fibers in the heart." *Journal of Histochemistry & Cytochemistry*, vol. 41, no. 3, pp. 465–469, 1993.

[68] D. Touboul, N. Efron, D. Smadja, D. Praud, F. Malet, and J. Colin, "Corneal confocal microscopy following conventional, transepithelial, and accelerated corneal collagen cross-linking procedures for keratoconus," *Journal of Refractive Surgery*, vol. 28, no. 11, pp. 769–775, 2012.

[69] B. E. A. Saleh and M. C. Teich, *Fundamentals of Photonics*. 2nd edition. John Wiley and Sons, Inc. New York, USA, 2007.

[70] W. Mohler, A. C. Millard, and P. J. Campagnola, "Second harmonic generation imaging of endogenous structural proteins," *Methods*, vol. 29, no. 1, pp. 97–109, 2003.

[71] R. W. Boyd, *Nonlinear Optics*. Academic Press, 2003.

[72] I. V. Shadrivov, A. A. Zharov, and Y. S. Kivshar, "Second-harmonic generation in nonlinear left-handed metamaterials," *JOSA B*, vol. 23, no. 3, pp. 529–534, 2006.

[73] P. Franken and J. Ward, "Optical harmonics and nonlinear phenomena," *Reviews of Modern Physics*, vol. 35, no. 1, p. 23, 1963.

[74] T. Kowalczyk, K. Singer, and P. Cahill, "Anomalous-dispersion phase-matched second-harmonic generation in a polymer waveguide," *Optics Letters*, vol. 20, no. 22, pp. 2273–2275, 1995.

[75] M. Hobden, "Phase-matched second-harmonic generation in biaxial crystals," *Journal of Applied Physics*, vol. 38, no. 11, pp. 4365–4372, 1967.

[76] A. Fiore, S. Janz, L. Delobel, P. van der Meer, P. Bravetti, V. Berger, E. Rosencher, and J. Nagle, "Second-harmonic generation at λ= 1.6 μm in AlGaAs/Al_2O_3 waveguides using birefringence phase matching," *Applied Physics Letters*, vol. 72, no. 23, pp. 2942–2944, 1998.

[77] N. Dong, F. Chen, and J. Vázquez de Aldana, "Efficient second harmonic generation by birefringent phase matching in femtosecond-laser-inscribed KTP cladding waveguides," *Physica Status Solidi (RRL)-Rapid Research Letters*, vol. 6, no. 7, pp. 306–308, 2012.

[78] M. Yamada, N. Nada, M. Saitoh, and K. Watanabe, "First-order quasi-phase matched linbo3 waveguide periodically poled by applying an external field for efficient blue second-harmonic generation," *Applied Physics Letters*, vol. 62, no. 5, pp. 435–436, 1993.

[79] P. S. Kuo, J. Bravo-Abad, and G. S. Solomon, "Second-harmonic generation using-quasi-phasematching in a GaAs whispering-gallery-mode microcavity," *Nature Communications*, vol. 5, p. 3109, 2014.

[80] J. Gannaway and C. Sheppard, "Second-harmonic imaging in the scanning optical microscope," *Optical and Quantum Electronics*, vol. 10, no. 5, pp. 435–439, 1978.

[81] M. Fiebig, V. V. Pavlov, and R. V. Pisarev, "Second-harmonic generation as a tool for studying electronic and magnetic structures of crystals," *JOSA B*, vol. 22, no. 1, pp. 96–118, 2005.

[82] M. Timofeeva, A. Bouravleuv, G. Cirlin, I. Shtrom, I. Soshnikov, M. Reig Escalé, A. Sergeyev, and R. Grange, "Polar second-harmonic imaging to resolve pure and mixed crystal phases along GaAs nanowires," *Nano Letters*, vol. 16, no. 10, pp. 6290–6297, 2016.

[83] I. I. Smolyaninov, A. V. Zayats, and C. C. Davis, "Near-field second-harmonic imaging of ferromagnetic and ferroelectric materials," *Optics Letters*, vol. 22, no. 21, pp. 1592–1594, 1997.

[84] S. I. Bozhevolnyi, J. M. Hvam, K. Pedersen, F. Laurell, H. Karlsson, T. Skettrup, and M. Belmonte, "Second-harmonic imaging of ferroelectric domain walls," *Applied Physics Letters*, vol. 73, no. 13, pp. 1814–1816, 1998.

[85] I. Freund, M. Deutsch, and A. Sprecher, "Connective tissue polarity. optical second-harmonic microscopy, crossed-beam summation, and small-angle scattering in rat-tail tendon," *Biophysical Journal*, vol. 50, no. 4, pp. 693–712, 1986.

[86] P. J. Campagnola and L. M. Loew, "Second-harmonic imaging microscopy for visualizing biomolecular arrays in cells, tissues and organisms," *Nature Biotechnology*, vol. 21, no. 11, p. 1356, 2003.

[87] G. Cox, E. Kable, A. Jones, I. Fraser, F. Manconi, and M. D. Gorrell, "3-dimensional imaging of collagen using second harmonic generation," *Journal of Structural Biology*, vol. 141, no. 1, pp. 53–62, 2003.

[88] D. A. Dombeck, M. Blanchard-Desce, and W. W. Webb, "Optical recording of action potentials with second-harmonic generation microscopy," *Journal of Neuroscience*, vol. 24, no. 4, pp. 999–1003, 2004.

[89] L. Sacconi, D. Dombeck, and W. Webb, "Overcoming photodamage in second-harmonic generation microscopy: real-time optical recording of neuronal action potentials," *Proceedings of the National Academy of Sciences of the United States of America*, vol. 103, no. 9, pp. 3124–3129, 2006.

[90] D. S. Peterka, H. Takahashi, and R. Yuste, "Imaging voltage in neurons," *Neuron*, vol. 69, no. 1, pp. 9–21, 2011.

[91] L. Moreaux, T. Pons, V. Dambrin, M. Blanchard-Desce, and J. Mertz, "Electro-optic response of second-harmonic generation membrane potential sensors," *Optics Letters*, vol. 28, no. 8, pp. 625–627, 2003.

[92] S. Feng and H. G. Winful, "Physical origin of the Gouy phase shift," *Optics Letters*, vol. 26, no. 8, pp. 485–487, 2001.

[93] L. Moreaux, O. Sandre, and J. Mertz, "Membrane imaging by second-harmonic generation microscopy," *JOSA B*, vol. 17, no. 10, pp. 1685–1694, 2000.

[94] J. Mertz, "Applications of second-harmonic generation microscopy," in *Handbook of Biomedical Nonlinear Optical Microscopy*, B. R. Masters and P. So, Eds. Oxford University Press, 2008, ch. 15, pp. 348–376.

[95] F. Légaré, C. Pfeffer, and B. R. Olsen, "The role of backscattering in shg tissue imaging," *Biophysical Journal*, vol. 93, no. 4, pp. 1312–1320, 2007.

[96] F. S. Pavone and P. J. Campagnola, *Second Harmonic Generation Imaging*. CRC Press, Boca Raton, 2014.

[97] R. LaComb, O. Nadiarnykh, S. S. Townsend, and P. J. Campagnola, "Phase matching considerations in second harmonic generation from tissues: Effects on emission directionality, conversion efficiency and observed morphology," *Optics Communications*, vol. 281, no. 7, pp. 1823–1832, Apr 2008. [Online]. Available: http://www.sciencedirect.com/science/article/pii/S0030401807010735

[98] R. M. Williams, W. R. Zipfel, and W. W. Webb, "Interpreting second-harmonic generation images of collagen I fibrils," *Biophysical Journal*, vol. 88, no. 2, pp. 1377–1386, 2005.

[99] R. A. R. Rao, M. R. Mehta, S. Leithem, and K. C. Toussaint, Jr., "Quantitative analysis of forward and backward second-harmonic images of collagen fibers using Fourier transform second-harmonic-generation microscopy," *Optics Letters*, vol. 34, no. 24, pp. 3779–3781, Dec 2009. [Online]. Available: http://ol.osa.org/abstract.cfm?URI=ol-34-24-3779

[100] M. Sivaguru, S. Durgam, R. Ambekar, D. Luedtke, G. Fried, A. Stewart, and K. C. Toussaint, "Quantitative analysis of collagen fiber organization in injured tendons using Fourier transform-second harmonic generation imaging," *Optics Express*, vol. 18, no. 24, pp. 24 983–24 993, 2010.

[101] R. A. Rao, M. R. Mehta, and K. C. Toussaint, "Fourier transform-second-harmonic generation imaging of biological tissues," *Optics Express*, vol. 17, no. 17, pp. 14 534–14 542, Aug 2009. [Online]. Available: http://www.opticsexpress.org/abstract.cfm?URI=oe-17-17-14534

[102] R. Ambekar, M. Chittenden, I. Jasiuk, and K. C. Toussaint, "Quantitative second-harmonic generation microscopy for imaging porcine cortical bone: comparison to SEM and its potential to investigate age-related changes," *Bone*, vol. 50, no. 3, pp. 643–650, 2012.

[103] H. Majeed, C. Okoro, A. Kajdacsy-Balla, K. C. Toussaint, and G. Popescu, "Quantifying collagen fiber orientation in breast cancer using quantitative phase imaging," *Journal of Biomedical Optics*, vol. 22, no. 4, p. 046004, 2017.

[104] X. Han, R. M. Burke, M. L. Zettel, P. Tang, and E. B. Brown, "Second harmonic properties of tumor collagen: determining the structural relationship between reactive stroma and healthy stroma," *Optics Express*, vol. 16, no. 3, pp. 1846–1859, Feb 2008. [Online]. Available: http://www.opticsexpress.org/abstract.cfm?URI=oe-16-3-1846

[105] T. Hompland, A. Erikson, M. Lindgren, T. Lindmo, and C. de Lange Davies, "Second-harmonic generation in collagen as a potential cancer diagnostic parameter," *Journal of Biomedical Optics*, vol. 13, no. 5, pp. 054 050–054 050, 2008.

[106] R. Ambekar, T.-Y. Lau, M. Walsh, R. Bhargava, and K. C. Toussaint, Jr., "Quantifying collagen structure in breast biopsies using second-harmonic generation imaging," *Biomedical Optics Express*, vol. 3, no. 9, pp. 2021–2035, Sep 2012. [Online]. Available: http://www.opticsinfobase.org/boe/abstract.cfm?URI=boe-3-9-2021

[107] M. Born and E. Wolf, *Principles of Optics: Electromagnetic Theory of Propagation, Interference and Diffraction of Light.* Elsevier, 2013.

[108] C. Okoro, H. E. Kondakci, A. F. Abouraddy, and K. C. Toussaint, "Demonstration of an optical-coherence converter," *Optica*, vol. 4, no. 9, pp. 1052–1058, 2017.

[109] Y. Shi, W. McClain, and R. Harris, "Generalized Stokes-Mueller formalism for two-photon absorption, frequency doubling, and hyper-Raman scattering," *Physical Review A*, vol. 49, no. 3, p. 1999, 1994.

[110] C. Brosseau, *Fundamentals of Polarized Light: A Statistical Optics Approach*. Wiley-Interscience, 1998.

[111] C. R. Givens and A. B. Kostinski, "A simple necessary and sufficient condition on physically realizable mueller matrices," *Journal of Modern Optics*, vol. 40, no. 3, pp. 471–481, 1993.

[112] J. E. Ahmad and Y. Takakura, "Estimation of physically realizable mueller matrices from experiments using global constrained optimization," *Optics Express*, vol. 16, no. 18, pp. 14 274–14 287, 2008.

[113] M. Bass, E. W. Van Stryland, D. R. Williams, and W. L. Wolfe, Eds., *Handbook of Optics*. McGraw-Hill, New York, 2001.

[114] S.-Y. Lu and R. A. Chipman, "Homogeneous and inhomogeneous jones matrices," *JOSA A*, vol. 11, no. 2, pp. 766–773, 1994.

[115] S. Cloude, "Group theory and polarization algebra," *Optik*, vol. 75, no. 1, pp. 26–36, 1986.

[116] Z.-F. Xing, "On the deterministic and non-deterministic Mueller matrix," *Journal of Modern Optics*, vol. 39, no. 3, pp. 461–484, 1992.

[117] S.-Y. Lu and R. A. Chipman, "Interpretation of Mueller matrices based on polar decomposition," *J. Opt. Soc. Am. A*, vol. 13, no. 5, pp. 1106–1113, May 1996.

[118] J. Chung, W. Jung, M. J. Hammer-Wilson, P. Wilder-Smith, and Z. Chen, "Use of polar decomposition for the diagnosis of oral precancer," *Applied Optics*, vol. 46, no. 15, pp. 3038–3045, 2007.

[119] P. Shukla and A. Pradhan, "Mueller decomposition images for cervical tissue: Potential for discriminating normal and dysplastic states," *Optics express*, vol. 17, no. 3, pp. 1600–1609, 2009.

[120] N. Ghosh, M. F. Wood, S.-h. Li, R. D. Weisel, B. C. Wilson, R.-K. Li, and I. A. Vitkin, "Mueller matrix decomposition for polarized light assessment of biological tissues," *Journal of Biophotonics*, vol. 2, no. 3, pp. 145–156, 2009.

[121] C. Okoro and K. C. Toussaint, "Second-harmonic patterned polarization-analyzed reflection confocal microscope," *Journal of Biomedical Optics*, vol. 22, no. 8, p. 086007, 2017.

[122] R. Azzam, "Propagation of partially polarized light through anisotropic media with or without depolarization: a differential $4\times$ 4 matrix calculus," *J. Opt. Soc. Am.*, vol. 68, no. 12, pp. 1756–1767, 1978.

[123] R. Ossikovski, "Differential matrix formalism for depolarizing anisotropic media," *Optics Letters*, vol. 36, no. 12, pp. 2330–2332, 2011.

[124] S. Kumar, H. Purwar, R. Ossikovski, I. A. Vitkin, and N. Ghosh, "Comparative study of differential matrix and extended polar decomposition formalisms for polarimetric characterization of complex tissue-like turbid media," *Journal of Biomedical Optics*, vol. 17, no. 10, pp. 105 006–105 006, 2012.

[125] N. Mazumder, J. Qiu, M. R. Foreman, C. M. Romero, C.-W. Hu, H.-R. Tsai, P. Török, and F.-J. Kao, "Polarization-resolved second harmonic generation microscopy with a four-channel stokes-polarimeter," *Optics Express*, vol. 20, pp. 14 090–14 099, Jun 2012. [Online]. Available: http://www.opticsexpress.org/abstract.cfm?URI=oe-20-13-14090

[126] F. J. Ávila, O. del Barco, and J. M. Bueno, "Mueller-matrix second harmonic microscopy of collagen-based tissues," in *Focus on Microscopy, 2015*, 2015.

[127] C. Okoro and K. C. Toussaint, "Experimental demonstration of two-photon Mueller matrix second-harmonic generation microscopy," *Journal of Biomedical Optics*, vol. 21, no. 1, p. 016011, 2016.

[128] M. Samim, S. Krouglov, and V. Barzda, "Double Stokes Mueller polarimetry of second-harmonic generation in ordered molecular structures," *J. Opt. Soc. Am. B*, vol. 32, no. 3, pp. 451–461, 2015.

[129] H. Kang, B. Jia, and M. Gu, "Polarization characterization in the focal volume of high numerical aperture objectives," *Optics Express*, vol. 18, no. 10, pp. 10 813–10 821, May 2010. [Online]. Available: http://www.opticsexpress.org/abstract.cfm?URI=oe-18-10-10813

[130] T. Y. Lau, R. Ambekar, and K. C. Toussaint, "Quantification of collagen fiber organization using three-dimensional Fourier transform-second-harmonic generation imaging," *Optics Express*, vol. 20, no. 19, pp. 21 821–21 832, 2012.

[131] J. B. Pawley, "Laser sources for confocal microscopy," in *Handbook of Biological Confocal Microscopy*. Springer, 2006, pp. 20–42.

[132] A. Diaspro, "Resolution and contrast in confocal and two-photon microscopy," in *Confocal and Two-Photon Microscopy: Foundations, Applications and Advances*. Wiley-Liss, 2001, pp. 101–125.

[133] S. Pereira and A. Van de Nes, "Superresolution by means of polarisation, phase and amplitude pupil masks," *Optics Communications*, vol. 234, no. 1, pp. 119–124, 2004.

[134] J. L. Pezzaniti and R. A. Chipman, "Mueller matrix imaging polarimetry," *Optical Engineering*, vol. 34, no. 6, pp. 1558–1569, 1995.

[135] A. Diaspro, Ed., *Confocal and Two-Photon Microscopy: Foundations, Applications and Advances*, Wiley, 2001.

[136] V. Ottani, M. Raspanti, and A. Ruggeri, "Collagen structure and functional implications," *Micron*, vol. 32, no. 3, pp. 251–260, 2001.

[137] L. David, E. S. Grood, F. R. Noyes, R. E. Zernicke et al., "Biomechanics of ligaments and tendons." *Exerc. Sport Sci. Rev.*, vol. 6, no. 1, pp. 125–182, 1978.

[138] B. de Campos Vidal, "Image analysis of tendon helical superstructure using interference and polarized light microscopy," *Micron*, vol. 34, no. 8, pp. 423–432, 2003.

[139] P. Whittaker, D. Boughner, D. Perkins, and P. Canham, "Quantitative structural analysis of collagen in chordae tendineae and its relation to floppy mitral valves and proteoglycan infiltration." *Heart*, vol. 57, no. 3, pp. 264–269, 1987.

[140] R. L. Siegel, K. D. Miller, and A. Jemal, "Cancer statistics, 2018," *CA: A Cancer Journal for Clinicians*, vol. 68, no. 1, pp. 7–30, 2018.

[141] K. D. Miller, R. L. Siegel, C. C. Lin, A. B. Mariotto, J. L. Kramer, J. H. Rowland, K. D. Stein, R. Alteri, and A. Jemal, "Cancer treatment and survivorship statistics, 2016," *CA: A Cancer Journal for Clinicians*, vol. 66, no. 4, pp. 271–289, 2016.

[142] P. Taneja, D. Maglic, F. Kai, S. Zhu, R. D. Kendig, A. F. Elizabeth, and K. Inoue, "Classical and novel prognostic markers for breast cancer and their clinical significance," *Clinical Medicine Insights: Oncology*, vol. 4, pp. CMO–S4773, 2010.

[143] B. Weigelt, J. L. Peterse, and L. J. Van't Veer, "Breast cancer metastasis: markers and models," *Nature Reviews Cancer*, vol. 5, no. 8, p. 591, 2005.

[144] A. Bergamaschi, E. Tagliabue, T. Sørlie, B. Naume, T. Triulzi, R. Orlandi, H. Russnes, J. Nesland, R. Tammi, P. Auvinen et al., "Extracellular matrix signature identifies breast cancer subgroups with different clinical outcome," *The Journal of Pathology*, vol. 214, no. 3, pp. 357–367, 2008.

[145] M. W. Pickup, J. K. Mouw, and V. M. Weaver, "The extracellular matrix modulates the hallmarks of cancer," *EMBO Reports*, p. e201439246, 2014.

[146] J. Insua-Rodríguez and T. Oskarsson, "The extracellular matrix in breast cancer," *Advanced Drug Delivery Reviews*, vol. 97, pp. 41–55, 2016.

[147] P. P. Provenzano, K. W. Eliceiri, J. M. Campbell, D. R. Inman, J. G. White, and P. J. Keely, "Collagen reorganization at the tumor-stromal interface facilitates local invasion," *BMC Medicine*, vol. 4, no. 1, p. 38, 2006.

[148] M. W. Conklin, J. C. Eickhoff, K. M. Riching, C. A. Pehlke, K. W. Eliceiri, P. P. Provenzano, A. Friedl, and P. J. Keely, "Aligned collagen is a prognostic signature for survival in human breast carcinoma," *The American Journal of Pathology*, vol. 178, no. 3, pp. 1221–1232, 2011.

[149] K. M. Riching, B. L. Cox, M. R. Salick, C. Pehlke, A. S. Riching, S. M. Ponik, B. R. Bass, W. C. Crone, Y. Jiang, A. M. Weaver et al., "3D collagen alignment limits protrusions to enhance breast cancer cell persistence," *Biophysical Journal*, vol. 107, no. 11, pp. 2546–2558, 2014.

[150] P. P. Provenzano, D. R. Inman, K. W. Eliceiri, J. G. Knittel, L. Yan, C. T. Rueden, J. G. White, and P. J. Keely, "Collagen density promotes mammary tumor initiation and progression," *BMC Medicine*, vol. 6, no. 1, p. 11, 2008.

[151] C. E. Barcus, E. C. Holt, P. J. Keely, K. W. Eliceiri, and L. A. Schuler, "Dense collagen-I matrices enhance pro-tumorigenic estrogen-prolactin crosstalk in MCF-7 and T47D breast cancer cells," *PloS One*, vol. 10, no. 1, p. e0116891, 2015.

[152] I. Acerbi, L. Cassereau, I. Dean, Q. Shi, A. Au, C. Park, Y. Chen, J. Liphardt, E. Hwang, and V. Weaver, "Human breast cancer invasion and aggression correlates with ECM stiffening and immune cell infiltration," *Integrative Biology*, vol. 7, no. 10, pp. 1120–1134, 2015.

[153] S. Brasselet, "Polarization-resolved nonlinear microscopy: Application to structural molecular and biological imaging," *Advances in Optics and Photonics*, vol. 3, no. 3, p. 205, 2011.

[154] S. Liu, X. Chen, and C. Zhang, "Development of a broadband Mueller matrix ellipsometer as a powerful tool for nanostructure metrology," *Thin Solid Films*, vol. 584, pp. 176–185, 2015.

[155] B. S. Manjunatha, A. Agrawal, V. Shah et al., "Histopathological evaluation of collagen fibers using picrosirius red stain and polarizing microscopy in oral squamous cell carcinoma," *Journal of Cancer Research and Therapeutics*, vol. 11, no. 2, p. 272, 2015.

[156] W. Drexler, D. Stamper, C. Jesser, X. Li, C. Pitris, K. Saunders, S. Martin, M. B. Lodge, J. G. Fujimoto, and M. E. Brezinski, "Correlation of collagen organization with polarization sensitive imaging of in vitro cartilage: implications for osteoarthritis." *The Journal of Rheumatology*, vol. 28, no. 6, pp. 1311–1318, 2001.

[157] J. Rieppo, J. Hallikainen, J. S. Jurvelin, I. Kiviranta, H. J. Helminen, and M. M. Hyttinen, "Practical considerations in the use of polarized light microscopy in the analysis of the collagen network in articular cartilage," *Microscopy Research and Technique*, vol. 71, no. 4, pp. 279–287, 2008.

[158] N.-J. Jan, J. L. Grimm, H. Tran, K. L. Lathrop, G. Wollstein, R. A. Bilonick, H. Ishikawa, L. Kagemann, J. S. Schuman, and I. A. Sigal, "Polarization microscopy for characterizing fiber orientation of ocular tissues," *Biomedical Optics Express*, vol. 6, no. 12, pp. 4705–4718, 2015.

[159] R. Ambekar, T.-Y. Lau, M. Walsh, R. Bhargava, and K. C. Toussaint, "Quantifying collagen structure in breast biopsies using second-harmonic generation imaging," *Biomeical Optics Express*, vol. 3, no. 9, pp. 2021–2035, 2012.

[160] M. H. Smith, P. D. Burke, A. Lompado, E. A. Tanner, and L. W. Hillman, "Mueller matrix imaging polarimetry in dermatology," in *Biomedical Diagnostic, Guidance, and Surgical-Assist Systems II*, vol. 3911. International Society for Optics and Photonics, 2000, pp. 210–217.

[161] M. H. Smith, "Interpreting mueller matrix images of tissues," in *Laser-tissue Interaction XII: Photochemical, Photothermal, and Photomechanical*, vol. 4257. International Society for Optics and Photonics, 2001, pp. 82–90.

[162] S. Alali and I. A. Vitkin, "Polarized light imaging in biomedicine: emerging mueller matrix methodologies for bulk tissue assessment," *Journal of Biomedical Optics*, vol. 20, no. 6, p. 061104, 2015.

[163] A. Pierangelo, A. Benali, M.-R. Antonelli, T. Novikova, P. Validire, B. Gayet, and A. De Martino, "Ex-vivo characterization of human colon cancer by Mueller polarimetric imaging," *Optics Express*, vol. 19, no. 2, pp. 1582–1593, 2011.

[164] C. He, H. He, X. Li, J. Chang, Y. Wang, S. Liu, N. Zeng, Y. He, and H. Ma, "Quantitatively differentiating microstructures of tissues by frequency distributions of Mueller matrix images," *Journal of Biomedical Optics*, vol. 20, no. 10, p. 105009, 2015.

[165] A. Tata, A. Gribble, M. Ventura, M. Ganguly, E. Bluemke, H. J. Ginsberg, D. A. Jaffray, D. R. Ifa, A. Vitkin, and A. Zarrine-Afsar, "Wide-field tissue polarimetry allows efficient localized mass spectrometry imaging of biological tissues," *Chemical Science*, vol. 7, no. 3, pp. 2162–2169, 2016.

[166] Y. Dong, J. Qi, H. He, C. He, S. Liu, J. Wu, D. S. Elson, and H. Ma, "Quantitatively characterizing the microstructural features of breast ductal carcinoma tissues in different progression stages by mueller matrix microscope," *Biomedical Optics Express*, vol. 8, no. 8, pp. 3643–3655, 2017.

[167] W. Lee, M. M. Kabir, R. Emmadi, and K. C. Toussaint, "Third-harmonic generation imaging of breast tissue biopsies," *Journal of Microscopy*, vol. 264, no. 2, pp. 175–181, 2016.

[168] M. Sivaguru, J. P. Eichorst, S. Durgam, G. A. Fried, A. A. Stewart, and M. C. Stewart, "Imaging horse tendons using multimodal 2-photon microscopy," *Methods*, vol. 66, no. 2, pp. 256–267, 2014.

[169] R. A. R. Rao, M. R. Mehta, S. Leithem, and K. C. Toussaint Jr, "Quantitative analysis of forward and backward second-harmonic images of collagen fibers using fourier transform second-harmonic-generation microscopy," *Optics Letters*, vol. 34, no. 24, pp. 3779–3781, 2009.

[170] J. E. Marturano, J. F. Xylas, G. V. Sridharan, I. Georgakoudi, and C. K. Kuo, "Lysyl oxidase-mediated collagen crosslinks may be assessed as markers of functional properties of tendon tissue formation," *Acta Biomaterialia*, vol. 10, no. 3, pp. 1370–1379, 2014.

[171] M. Egeblad, M. G. Rasch, and V. M. Weaver, "Dynamic interplay between the collagen scaffold and tumor evolution," *Current Opinion in Cell Biology*, vol. 22, no. 5, pp. 697–706, 2010.

[172] S. Gangadhara, P. Barrett-Lee, R. I. Nicholson, and S. Hiscox, "Pro-metastatic tumor–stroma interactions in breast cancer," *Future Oncology*, vol. 8, no. 11, pp. 1427–1442, 2012.

[173] J. W. Birk, M. Tadros, K. Moezardalan, O. Nadyarnykh, F. Forouhar, J. Anderson, and P. Campagnola, "Second harmonic generation imaging distinguishes both high-grade dysplasia and cancer from normal colonic mucosa," *Digestive Diseases and Sciences*, vol. 59, no. 7, pp. 1529–1534, 2014.

[174] V. Pasta, M. Monti, M. Cialini, M. Vergine, P. Urciuoli, A. Iacovelli, S. Rea, and V. DOrazi, "Primitive sarcoma of the breast: new insight on the proper surgical management," *Journal of Experimental & Clinical Cancer Research*, vol. 34, no. 1, p. 72, 2015.

[175] L. Wang, P. Ho, C. Liu, G. Zhang, and R. Alfano, "Ballistic 2-d imaging through scattering walls using an ultrafast optical kerr gate," *Science*, vol. 253, no. 5021, pp. 769–771, 1991.

[176] W. Wang, L. G. Lim, S. Srivastava, J. S. B. Yan, A. Shabbir, and Q. Liu, "Roles of linear and circular polarization properties and effect of wavelength choice on differentiation between ex vivo normal and cancerous gastric samples," *Journal of Biomedical Optics*, vol. 19, no. 4, pp. 046 020–046 020, 2014.